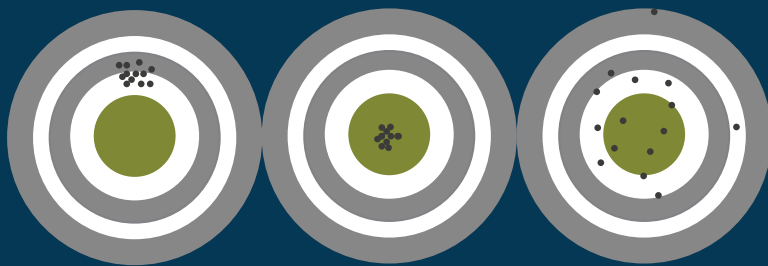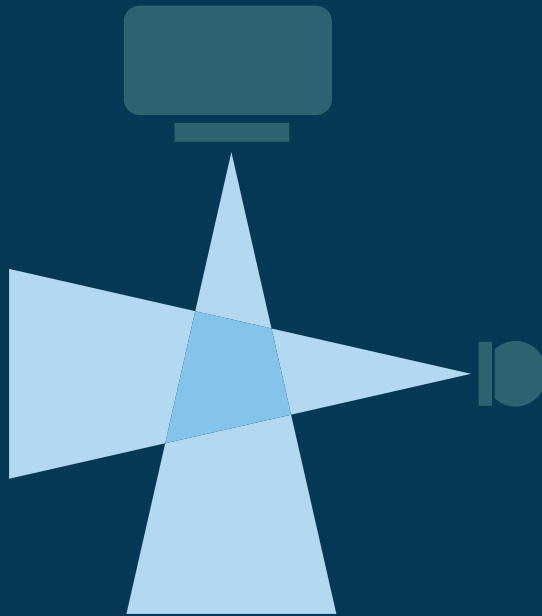# Fast Daily Interfraction and Intrafraction Prostate Repositioning For High Precision Radiotherapy

Theodore Funwi Mutanga

Fast Daily Interfraction and Intrafraction Prostate Repositioning for High Precision Radiotherapy

Theodore Funwi Mutanga

Cover: (top) A representation of crossfire MV and kV imaging; (bottom left) Example of systematic positioning error; (bottom right) Example of random positioning error; (bottom center) Reduction of systematic and random errors by online positioning using the method described in this thesis.

Fast Daily Interfraction and Intrafraction Prostate Repositioning for High Precision Radiotherapy

Snelle dagelijkse interfractie en intrafractie prostaat herpositionering voor hoge precisie radiotherapie

Proefschrift

ter verkrijging van de graad van doctor aan de
Erasmus Universiteit Rotterdam
op gezag van de
Rector Magnificus

Prof. dr. H. G. Schmidt

en volgens besluit van het College voor Promoties.

De openbare verdediging zal plaatsvinden op
Dinsdag 21 Juni 2011 om 13:30 uur

door

THEODORE FUNWI MUTANGA
geboren te Bamenda, Kameroen

ERASMUS UNIVERSITEIT ROTTERDAM

Promotiecommissie

Promotor: Prof. dr. B. J. M. Heijmen

Overige leden: Prof. dr. P. C. Levendag
                        Prof. dr. C. H. Bangma
                        Prof. dr. M. B. van Herk

"For what is a man profited, if he shall gain the whole world, and lose his own soul?"

HOLY BIBLE, MATTHEW 16:26, KING JAMES VERSION

to Gisele, Preston and Gaby
to my mother, Pauline, who'll always be with me
to my family, for all invaluable support

Contents

CHAPTER 1

General introduction

1.1 Prostate cancer

Prostate cancer is the most common form of cancer affecting men all over the world and it is the second leading cause of cancer-related deaths in males [1, 2]. The majority of new cases are diagnosed in a non-metastatic stage of the disease with almost 85% of the cancers confined to local or regional site [3]. While advanced metastatic prostate cancer is usually treated with palliative intent, successful treatments with curative intent have been developed for clinically localized prostate cancer and are constantly being improved [4–9].

Over the last few decades, external beam radiation therapy (EBRT) has been one of the curative treatment options available for the management of clinically localized prostate cancer and is generally believed to be used for about half of the diagnosed patients [9, 10]. While clinical outcomes assessed in terms of survival rates measured after long-term patient follow-up have been largely satisfactory, efforts to improve the efficacy of this modality have focused on increasing the control of tumour with higher doses [11–14]. However, these higher treatment doses have been associated with increased acute and late side-effect [11, 15]. The main side effects of EBRT which impact quality of life of patients include gastro-intestinal and genitourinary toxicity as well as reduced sexual function [11, 16, 17]. These side effects can be minimized by limiting radiation damage to responsible anatomical structures using techniques that ensure precise and accurate dose delivery to the tumour [18].

In EBRT for prostate cancer, ionizing radiation (mainly photons but other types of particles such as electrons, protons and heavy ions) usually from a linear accelerator (linac) are applied externally from several directions to deliver a lethal dose of radiation to the target area while avoiding as much as possible nearby healthy normal tissues or organs at risk (OAR). The target is usually the prostate but for more advanced stage prostate cancer, seminal vesicles and regional pelvic lymph nodes might also be included in the treated volum [19, 20]. The rectum , bladder and urethra constitute the main OAR but other structures in the vicinity of the prostate including the femoral heads and penile bulb are also at risk of radiation exposure. EBRT treatments involve daily delivery of small fractions of the total prescribed dose over a treatment course of several weeks. This fractionated nature of treatment delivery allows sufficient time for cells of normal tissues to be repaired while at the same time allowing for a maximum likelihood of the cancerous cells to be damaged [21]. Cancerous cells proliferate more than normal cells and as such they are more susceptible to DNA damage by radiation. The fractionated treatment implies that the process of patient positioning and treatment delivery has to be repeated on each treatment

day. Therefore accurate and reproducible daily target positioning measures have to be implemented to align the target in relation to treatment beams. Accurate patient positioning will ensure that the target gets the planned dose and collateral damage to nearby healthy normal tissues is minimized.

1.2 Geometric errors in prostate radiotherapy

The accuracy of dose delivery in EBRT is limited by uncertainty in target location in relation to planned beams at the time of treatment. This uncertainty in target localization is due to errors caused by any deviations between the planned and executed treatments. Set-up errors arise from the inaccuracy in patient (and target) position in relation to the planned position. Also, various physiologic processes occurring within the body, for instance breathing, urinal bladder and rectum fillings cause internal organ motion as well as changes in organ orientation (rotation), shape and size (deformation) which in turn cause errors in the delivered treatment. Set-up errors as well as internal organ motion and morphologic errors can be categorized as inter-fraction and intrafraction meaning between treatment days and during a treatment fraction, respectively. All geometric errors can be classified as *systematic* - reflecting the difference in the average geometry within the treatment fraction compared to the snapshot geometry at treatment planning, and *random* - reflecting the day-to-day geometric variations about the mean. The classification of geometric errors into systematic and random errors turns out to be useful when evaluating various strategies for managing geometric errors and for establishing treatment planning safety margins.

In addition to set-up, organ motion and morphologic errors mentioned above, there is another source of error arising from uncertainty in defining the anatomic organs (targets and OAR) at planning. Although these delineation errors are quite important and can affect the treatment efficacy, they are not specifically studied in this thesis. Nevertheless, measures should be taken to minimize them and to account for the residuals during the planning process.

1.3 Management of geometric errors

Geometric errors are mainly incorporated into the treatment planning process by use of safety margins around the target volume following recommendations of the International Commission on Radiation Units and Measurements (ICRU)[22–24]. The

ICRU defines various volumes related to the management of geometric errors. The clinical target volume (CTV) includes the delineated gross tumour volume (GTV) and the surrounding region where sub-clinical disease is expected. The planning target volume (PTV) is the CTV plus a margin to accommodate the anticipated geometric errors during treatment as well as target definition errors. The CTV-PTV margin must ensure that the prescribed dose is actually delivered to the CTV with high confidence level. The theoretical framework constructed in the ICRU reports forms a basis for managing geometrical uncertainties, which is a prerequisite to high-precision radiotherapy.

Margin recipes (formulas) which are based on assessments of distributions of geometric errors have been developed and widely used to determine the size of the CTV-PTV margin in prostate radiotherapy [25, 26]. A PTV margin that is too wide will unnecessarily increase radiation to normal tissues. Conversely, margins that are too small will increase the risk of missing parts of the target in some or even all fractions.

Since margins are based on localization errors, verification and correction measures that aim to reduce geometric errors will allow for the use of smaller planning margins. Corrective measures can be implemented using either information gathered from previous treatment fractions (*offline* approach) to adjust subsequent treatment fractions or using information acquired in the current treatment fraction (*online* approach) to correct for observed geometric variations. Online approaches have the advantage over offline approaches that in addition to correcting for systematic errors originating from the preparation phase, random day-to-day errors are corrected as well. The online approach therefore allows for the use of smaller margins, minimal dose to normal tissues and eliminates the risk of missing the target. Until recently, online solutions for target localization and correction of interfraction and intrafraction errors have not been widely clinically available because of associated increased workload due to more frequent imaging and analysis as well as needed equipment.

1.3.1   Use of implanted markers in prostate radiotherapy

The possibility to visualize small radio-opaque markers implanted into the prostate to act as surrogates for the prostate location has been greatly facilitated by developments in electronic portal imaging devices (EPIDs). The high contrast resolution of modern EPIDs which are present on most linacs have allowed the markers to be visualized on portal images with dose as little as 1-2 monitor unitss (MUs) implying that they can be used for daily (frequent) imaging with minimal associated imaging dose to the patient. Since a few years, linacs are also equipped with kV imaging

systems yielding high quality imaging of implanted markers. The markers, usually made of metals like gold and platinum, have been shown to be stable in the prostate with minimal marker migrations [27–29]. Thus, these markers can be used as reliable surrogates for the prostate.

Traditional methods for patient positioning have relied on bony anatomy for judging the target position in prostate radiotherapy. Because internal organs exhibit motion with respected to the bony anatomy, this method is not reliable. Implanted markers are advantageous over bony anatomy based positioning methods especially when using intensity modulated radiation therapy (IMRT) fields with small segments which cannot capture the whole pelvic bony anatomy in the field of view. Because the position of markers can be defined unambiguously in planar images, the three-dimensional (3D) positions of the markers can be reconstructed automatically using stereoscopic imaging and fast computer reconstruction algorithms, allowing for fast online set-up positioning correction.

1.4   Objectives and scope of the thesis

The main objective of the research in this thesis is the development and evaluation of systems and methods for improving the accuracy with which EBRT treatments can be delivered using the general framework of image guided radiation therapy (IGRT). To this end, a system designated StereoGraphic Targeting (SGT) was designed for daily interfraction(at start of treatment) positioning and later extended for intrafraction(during treatment) prostate repositioning using imaging of implanted markers and subsequent software-controlled, remote position adjustments (couch translations). The main requirements for this system which were considered include: 1) minimal increase in fraction duration 2) highest possible accuracy 3) minimal workload from imaging, image evaluation and position adjustments (couch shifts) 4) minimal additional imaging dose.

The second objective of the research in this thesis is the assessment of residual errors including organ deformation and rotation which remain after translation corrections. Since the IGRT approach only corrects for translational errors, we sought to quantify the other residual errors and evaluate appropriate planning margins to account for them. The overall goal is to ensure that the prescribed dose is delivered precisely to the defined target while minimizing radiation dose to nearby non-target organs, thereby also limiting radiation induced side effects.

Chapter 2 describes the design and clinical implementation of the online inter-

fraction positioning system designated StereoGraphic Targeting (SGT). The accuracy and performance of SGT will be investigated using both data from phantom studies and from patients treated clinically with SGT guidance.

While SGT corrects for interfraction positioning errors, there are also motions within the treatment fraction (intrafraction motion) after initial positioning corrections with SGT. In Chapter 3, this intrafraction motion will be characterised and quantified for a large number of patients. We will investigate in particular if there is significant systematic intrafraction motion and if this motion reproduces from day-to-day as well as within each fraction. Especially, systematic intrafraction motion can limit positioning accuracy of the prostate. Chapter 4 describes the design, clinical implementation and performance of intrafraction StereoGraphic Targeting (iSGT). iSGT is a proposed method extending SGT to correct for intrafraction motion of the prostate. The efficacy of iSGT in managing intrafraction motion will be analysed using clinical data from patients treated with and without iSGT intrafraction corrections.

In Chapter 5, the errors due to deformation of the prostate and seminal vesicles relative to implanted markers will be investigated using deformable registration and multiple organ delineations obtained from repeat CTs of prostate patients. The main objective will be to derive planning margins that could be expected to account for residual errors including especially organ deformation and rotation errors after daily marker-based prostate corrections with couch translations.

It is known that geometric uncertainties can have an effect on the treatment outcome (measure of tumour eradication and associated normal tissue complications) but the actual relationship between errors and final treatment outcome is not clearly known. This has mainly been due to the limitations in determining the actual delivered dose including the effects of geometric variations. Estimations of treatment outcome metrics (tumour control probability (TCP), normal tissue complication probability (NTCP)) are often computed on the static anatomy in the planning CT which does not include the anatomic variations during treatment. An important shortcoming of margin recipes is that they are computed based on population statistics and do not incorporate both rotational and deformation errors. It is just these errors that become essential after eliminating the translational errors such as with SGT and iSGT.

Presently, rotation and deformation errors are generally not corrected for and are only accommodated in the planning margins. For these errors, adaptive radiotherapy (ART) offers options for accounting for them. It is therefore relevant to investigate patient-specific geometric models which can be used for adaptive radio-

therapy. One possibility for adaptive radiation therapy (ART) is to use acquired data for geometric variations from a few initial (from first few fractions) samples of an individual patient. Using deformable registration of multiple computed tomography (CT)s of prostate patients with implanted markers for initial CT registration as a starting point, Chapter 6 addresses the practically relevant problem of creating patient-specific deformation models from individual patient data. Chapter 6 also presents a methodology for evaluating the delivered treatment dose in the presence of all measured residual geometric errors. A direct consequence of this is that it can be used in evaluating appropriate treatment planning margins for geometric errors using patient-specific data.

Lastly, in Chapter 7 the major findings of this thesis are discussed and a comparison is made with other IGRT methods. Future directions, with a view to ART for accounting for residual geometric errors will also be discussed.

Stereographic Targeting in Prostate Radiotherapy: Speed and Precision by Daily Automatic Positioning Corrections Using Kilovoltage/Megavoltage Image Pairs

Theodore F. Mutanga, Hans C. J. de Boer, Gerard J. van der Wielen, Davy Wentzler, Jaco Barnhoorn, Luca Incrocci and Ben J. M. Heijmen

Abstract

Purpose

A fully automated, fast, online prostate repositioning scheme using implanted markers, kilovoltage/megavoltage imaging, and remote couch movements has been developed and clinically applied. The initial clinical results of this stereographic targeting (SGT) method, as well as phantom evaluations, are presented.

Methods and Materials

Using the SGT method, portal megavoltage images are acquired with the first two to six monitor units of a treatment beam, immediately followed by acquisition of an orthogonal kilovoltage image without gantry motion. The image pair is automatically analyzed to obtain the marker positions and three-dimensional prostate displacement and rotation. Remote control couch shifts are applied to correct for the displacement. The SGT performance was measured using both phantom images and images from 10 prostate cancer patients treated using SGT.

Results

With phantom measurements, the accuracy of SGT was 0.5, 0.2, and 0.3 mm (standard deviation [SD]) for the left-right, craniocaudal, and anteroposterior directions, respectively, for translations and $0.5°$(SD) for the rotations around all axes. Clinically, the success rate for automatic marker detection was 99.5%, and the accuracy was 0.3, 0.5 and 0.8 mm (SD) in the left-right, craniocaudal, and anteroposterior axes. The SDs of the systematic center-of-mass positioning errors (Σ) were reduced from 4.0 mm to < 0.5 mm for all axes. The corresponding SD of the random (σ) errors was reduced from 3.0 to <0.8 mm. These small residual errors were achieved with a treatment time extension of < 1 min.

Conclusion

Stereographic targeting yields systematic and random prostate positioning errors of <1 mm with <1 min of added treatment time.

2.1   Introduction

Recent advances in electronic portal imaging devices (EPIDs) [30, 31], as well as linear accelerator-integrated kilovoltage (kV) scanners [32, 33], have enabled detailed investigation of the uncertainties in target position during external beam radiotherapy (EBRT). These uncertainties, stemming from deviations in patient anatomy during treatment relative to the anatomy during planning, lead to inaccuracies in the delivered dose distribution and possible loss of tumor control with an increased risk of complications. To account for the uncertainties, planning margins are added to the clinical target volume (CTV) to obtain the planning target volume (PTV) [24], while ensuring adequate CTV dose coverage. One of the goals of image-guided RT is to allow for the reduction of these margins through the reduction of the geometric errors during treatment, thereby potentially reducing toxicity. Combined with kV and/or megavoltage (MV) daily imaging (online approach), implanted markers not only allow for elimination of large geographic misses, but also for the reduction of both random and systematic errors [34]. Studies of the effect of systematic geometric misses due to a nonrepresentative rectal shape during acquisition of the planning computed tomography (CT) scan have indicated that such misses result in increased biochemical and clinical failure, even when margins of 1 cm have been applied [35, 36]. Online corrections can eliminate such misses while simultaneously allowing for smaller CTV-PTV margins [37–40].

This report describes stereographic targeting (SGT), a method for fast and accurate online prostate positioning with implanted markers using orthogonal cross-fire kV/MV imaging. The clinical data obtained for the first 10 patients treated with SGT are presented.

2.2   Methods and Materials

2.2.1   Preparation

Before CT scanning, cylindrical gold markers (1 mm x 5 mm; Heraeus GmbH, Engineered Materials Division, Hessen, Germany) were transperineally implanted in the prostate using 18-gauge implant needles under transrectal ultrasound guidance. Two markers were placed near the base and two near the apex. At least 1 week after implantation, the patients were scheduled for the planning CT scan (Somatom Sensation Open, Siemens Medical Solutions, Erlangen, Germany) with a reconstruction slice thickness of 2.5 mm. The interval between implantation and planning allowed

for any edema to resolve so that the anatomy in the scan would be representative for treatment [39, 41]. The reference positions of the markers with respect to the isocenter were reconstructed with a tool (*Define Marker 3D*) in the EPID software program, which in the present study used digitally reconstructed radiographs (DRRs). The input for this tool was at least two DRRs with sufficient beam angle separation (minimally 60°). The marker positions were first manually identified in at least two DRRs by clicking on the two edges of the marker. A rectangular contour was automatically drawn around the marker according to the two clicked points. Next, the tool automatically reconstructed the three-dimensional (3D) marker positions from the identified two-dimensional positions. For each marker identified on a DRR, the expected marker position in the other DRRs was indicated automatically to facilitate the process. The obtained reconstructed 3D marker reference positions were stored for later use in SGT.
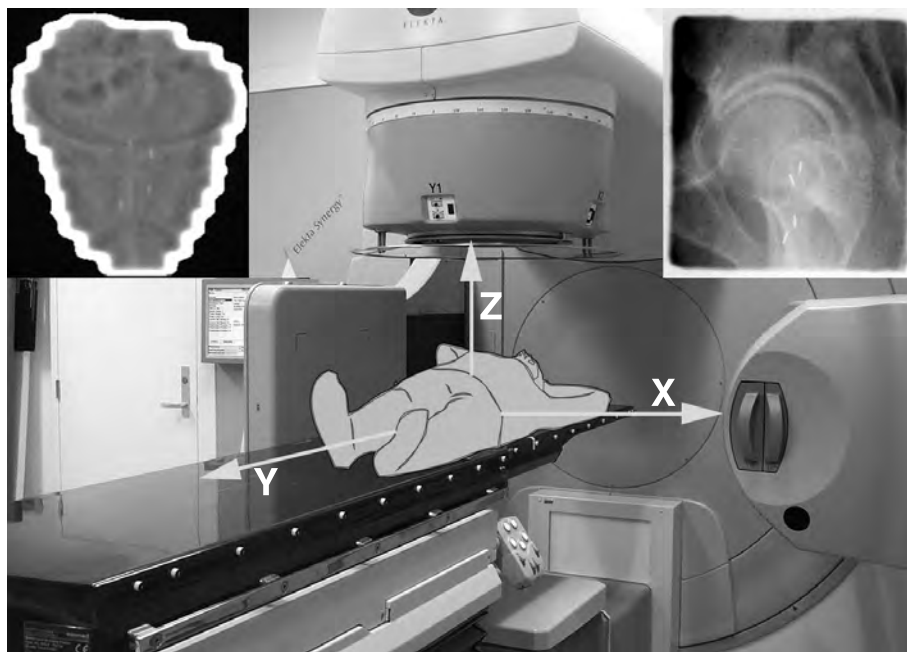

Figure 2.1: Coordinate system: anterior-posterior (Z), cranio-caudal (Y) and left-right (X), with orthogonal imagers and sample clinical images. Top left: megavoltage image. Top right: kilovoltage image.

2.2.2 Equipment

The cross-fire kV/MV imaging system (Figure 2.1) used in SGT was developed on the Synergy linear accelerator (Elekta, Crawley UK). For MV imaging, either a charge-coupled device, camera-based EPID (TheraView NT [TNT], Cablon Medical, Leusden, The Netherlands) or an iView GT flat-panel EPID (Elekta, Crawley, UK) can be used. In the present study, the TNT EPID (Cablon Medical) was used. The gantry-mounted XVI system enables acquisition of a planar image from the kV beam orthogonal to the MV beam directly before MV acquisition. Hence, the XVI/EPID combination can be used for acquisition of an orthogonal pair of images without intermediate gantry rotation. The TNT software was extended to provide all necessary tools for image processing, marker detection, analysis, and application of the positioning corrections.

The Theraview Couch Set-up Assistant (TCSA) system applies patient positioning corrections by remotely steering the Elekta Precision couch. The prototype of the TCSA used in this study was developed in collaboration with Cablon Medical and Elekta. It consisted of an independent controller personal computer connected to the couch control cabinet and to the TNT workstation. Treatment plan information, as well as positioning corrections, were transferred from TNT software to the TCSA controller while safety checks were being performed. The checks included correspondence of the patient and treatment plan identification numbers with the record and verify system, TCSA and couch hardware status, and communication integrity. In the case of any inconsistency, the TCSA moves to a passive state and stops any motion being executed. In the *offline mode*, the relative couch position as read by the TCSA is first zeroed by pressing a dedicated button on the couch's manual controls. Any pretreatment corrections such as those generated by an offline correction protocol are automatically executed by the TCSA while the motion enable bar is pressed. In the *online mode* used in SGT, zeroing the couch readout and execution of pretreatment corrections are the same but shifts of a maximum of 2 cm are also allowed under remote control of the TNT software. In the online mode, the radiographer in the control room must hold the keyboard spacebar of the TNT workstation to allow this couch motion.

2.2.3 SGT execution

At the start of each treatment fraction, the patient was positioned according to the alignment of the room lasers with the skin marks. If available, pretreatment (*off-line*) corrections were executed by the TCSA. Next, a lateral planar kV image (kVI) of 1024

x 1024 pixels was acquired with the XVI system using a dedicated collimator that projects a field size of 10×10 cm^2 at the isocenter. The clinical kVI acquisition settings (eight frames, 40 ms, 32 mA) resulted in a maximal skin dose of approximately 1.5 mGy. The acquired kVI was then automatically imported into the TNT workstation. The kVI acquisition was immediately followed by MV image (MVI) acquisition with the first part (2-6 monitor units [MU]) of the anteroposterior treatment beam. For IMRT, we apply the split IMRT field technique [42]. In the split IMRT field technique, the IMRT field is divided into a static and a modulated field, and an MVI of the former field is used in SGT. Congruence of the isocenter positions of the two orthogonal imagers was checked daily as a part of our routine quality assurance program [43] and was within 0.5 mm during the study period.

On the basis of the automatically extracted two-dimensional(2D) positions of the markers in the two orthogonal images, the 3D marker positions were reconstructed in the treatment coordinate system. The difference between the center of mass (COM) of the markers during a treatment fraction and the corresponding COM from the planning CT is the translational correction. Prostate rotations about the COM with respect to the planning CT scan for all three axes were also calculated. The translational correction was remotely executed under TCSA guidance if the magnitude of the correction vector was > 2 mm. After the correction has been applied, the SGT loop can be re-entered to acquire and analyze images for verification (Figure 2.2). If no further correction or verification is necessary, all treatment beams are delivered. In the present study, 3D verification using on a second kVI/MVI pair was always performed. In subsequent sections, we describe the procedure to automatically obtain the marker positions from the image pair in more detail.

2.2.4 Automatic marker detection and 3D position reconstruction

For the MVI, the image coordinate system was determined by registration of the detected field edge with the planned field edge [44]. For the kVI, the image coordinate system was retrieved from the XVI database. For both images, fixed pattern noise was eliminated by dividing each image with a flat field image. Automatic marker detection in each image required a set of previously obtained reference marker positions for the corresponding view, as described in the section 2.2.1 *"Preparation"*. The applied algorithm for automatic marker detection was based on a combination of template matching and marker extraction kernels (MEKs) [45], adapted for the rotations of individual markers. For each projected marker, the MEKs were calculated for a set of predetermined in-plane marker rotations. The range of these rotations

Time Ranges   patient set-up

EPID/XVI: 10-15s   kV/MV acquisition

matching: 2-3s   find displacements
inspection: 10-15s

automatic couch   execute corrections
corrections: 0-12s

verify ?   yes

no → treat
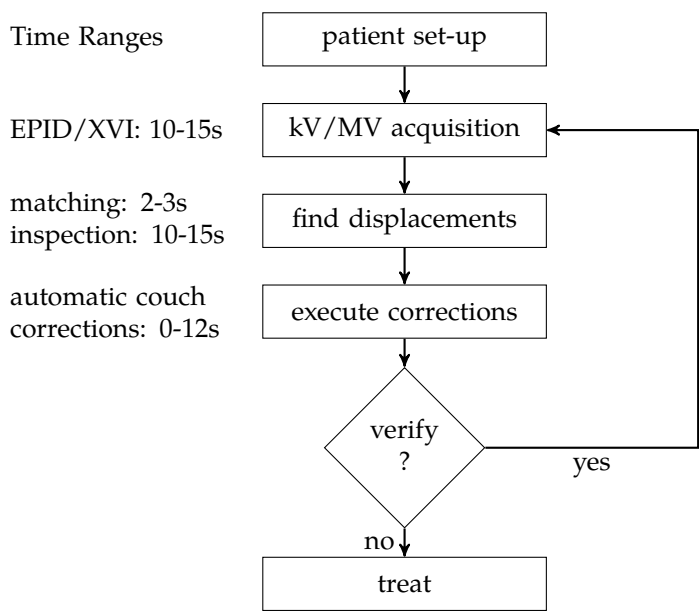
Figure 2.2: StereoGraphic Targeting workflow with observed time ranges for various subprocesses.

was determined by the initial marker orientation plus a maximal MEK rotation value (θ), which is set as an option in TNT. A θ-value of 20° was sufficient for marker detection in the present study. The sum of the rotated MEKs formed the effective MEK, which was then convolved with the input image to form the marker response image (Figure 2.3 b, f). The image was binarized with adaptive thresholding to select only those features with sufficient marker response. Although the markers stand out in the binary image, some features with shapes similar to markers (e.g., because of bony edges, calcifications, or image noise) are also visible (Figure 2.3 c, g). To obtain the true marker positions from the spots in the binary image, Chamfer matching [46] was used. Because the Chamfer match was performed with all markers simultaneously, it was insensitive to the features in the binary image that did not represent the markers. After Chamfer matching, the centroid of the spot with greatest response in the neighborhood of a marker was chosen as the detected marker position. With the marker positions thus identified in two orthogonal images, the 3D rigid body transformation that best mapped the marker reference positions onto the positions during a treatment fraction was found analytically from the least-squares minimization [47]. The residue errors per marker directly yielded information about the rigidity of the template, as well as whether the markers were associated with the correct blobs. The quality of the match, both overall and for individual markers, could thus be assessed.

In the visualization of the match results, the markers were presented with color coding to indicate this quality.
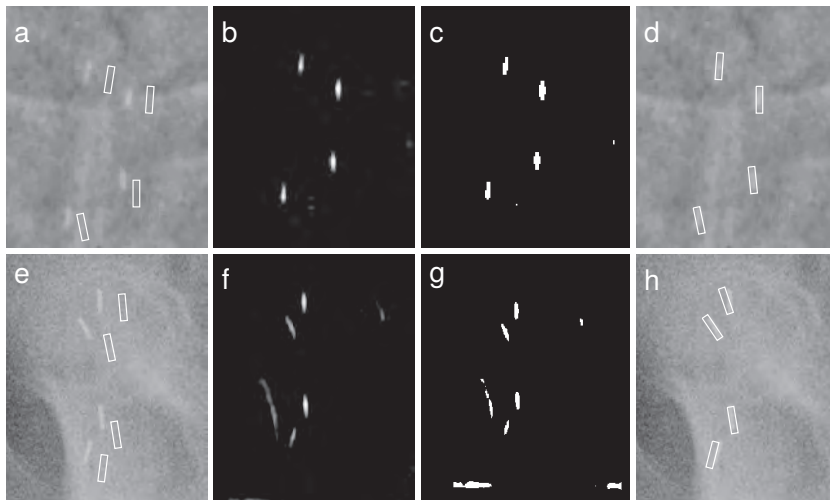
Figure 2.3: Marker matching on (a-d) megavoltage image and (e-h) kilovoltage image. Reference marker positions indicated by solid white rectangles and detected marker positions by dotted white rectangles. (a, e) Initial images, (b, f) images after convolution with marker extraction kernel, (c, g) images after binarization of convolution images, and (d, h) final images with detected marker positions.

2.2.5 Phantom measurements

The accuracy and success rate of SGT marker matching was studied for the clinically applied (kV/MV) image combination, as well as for another approach using two MVIs. Furthermore, the performance of SGT marker matching as a function of MV beam energy, as well as MV exposure, was investigated.

A phantom consisting of a stack of 10 square (41 x 41 cm^2) plates of RW3 (PTW, Germany) water-equivalent material was used. Each plate had a thickness of 1-2 cm so that the combined dimension of the phantom was 41 x 41 x 20 cm^3. Six gold markers were embedded in grooves on the two opposite faces of the central plate, with three markers on each face. The markers were placed such that the intermarker separation was 2, 4, and 1 cm in the left-right, craniocaudal, and anteroposterior directions, respectively. The phantom was placed on the treatment couch and shifts ranging from 0 to 20 mm in each direction with step sizes of 5 mm were executed using couch motion. Two orthogonal MVIs (MV *anteroposterior* and MV *lateral*) were acquired with varying exposures (1, 2, 4, 8 and 32 MU) after each shift, using the three available beam energies (6, 10, and 18 MV). A lateral kVI (kV *lateral*) was also

acquired after each MVI acquisition at the clinically applied exposure for each phantom position.

The marker matching accuracy and success rate in the presence of combined phantom rotations and translations were also studied using a dedicated phantom consisting of a water-filled box (30 x 20 x 30 cm^3) made of polymethyl metacrylate. Four gold markers were embedded in grooves on the two faces of a polymethyl metacrylate slab (30 x 20 x 2 cm^3), with two markers on each face. This slab was immersed in the water-filled box. Predefined rotations about the three principal directions (range, 0-20°; with a step size of 5°) were applied to the phantom with markers. Both kVI/MVI and MVI/MVI orthogonal images were acquired after each rotation step. Phantom translations were applied using couch shifts, and MVI exposures of 6 MU and 32 MU at 6 MV were studied.

2.2.6   Ground truth values for marker matches

A tool developed in MATLAB was used to obtain the *ground truth* transformation (three translations and three rotations) that the SGT matching software should ideally yield. With this tool, markers are manually identified in an orthogonal pair of images by clicking on the centers of the markers in each image. Given two pairs of orthogonal images and the corresponding manually identified marker positions, the tool calculates the rigid body transformation between the pairs of images. For each pair of images used, the procedure was repeated three times, and the mean transformation was calculated and used as the ground truth.

2.2.7   TCSA precision

The precision of the TCSA was measured using the slab phantom with embedded gold markers. Initially, the phantom was placed on the couch, and the absolute 3D position of the couch was obtained. Next, two orthogonal kVIs were acquired with the phantom in the initial position. Predetermined displacements ranging from -2 cm to 2 cm were applied to the phantom using couch shifts. After each execution of three random displacements along the three orthogonal axes, the absolute position of the couch in the room coordinate system was determined. Next, two orthogonal kVIs of the phantom were acquired, and the couch was moved back to the initial position. All images were imported into TNT, and the automatic SGT marker-matching tool was used to measure the applied displacements by comparing the marker positions in each image set with those in the initial reference images. For these measurements,

the clinically applied TCSA tolerance of 0.3 mm was used. The TCSA will not attempt to improve a deviation between the couch position readout and a prescribed position of < 0.3 mm. This tolerance setting enables fast convergence toward the prescribed position, without oscillations around the optimal position.

2.2.8 Clinical study

The positioning accuracy obtained with SGT was investigated for 10 patients treated with SGT during EBRT with three or four implanted markers. The treatment plan beam angle was 360° ± 1°, 90-93°, and 264-270° for the anteroposterior, left-lateral, and right-lateral directions, respectively. The dose prescription for 8 of the 10 patients was 72 Gy in 36 fractions at 2 Gy/fraction. Of the 10 patients, 2, who had previously undergone high-dose-rate brachytherapy, were treated with 1.8 Gy in 25 EBRT fractions, and the markers (three or four platinum cylinders; 3 mm x 1 mm) implanted during the brachytherapy procedure were used. For all patients, pre- and postcorrection kVI/MVI pairs were obtained, and the duration of all involved steps was logged. From the outcome of the automatic match in the SGT for these patients, the pre- and postcorrection systematic and random errors were calculated. In addition, for each fraction, the automatic match results found in the SGT procedure were compared with the ground truth values obtained with the tool described in the previous two sections to assess the accuracy of SGT positioning during clinical operation.

2.3 Results

2.3.1 Phantom verification: translations

The kV/MV combination yielded greater marker detection rates than the MV/MV approach because of the greater marker visibility in the lateral kV images (Figure 2.4). The success rate was calculated as the fraction of automatic matches with a 3D deviation from ground truth of < 2 mm. Because our goal with SGT was to obtain accuracy better than 2 mm for positioning errors, this was a conservative cutoff level.

The mean and SD values expressing differences between the automated SGT result and ground truth per translation direction are reported in Table 2.1 for each exposure, beam energy, and combination of orthogonal images. In Table 2.1, slightly greater magnitudes of deviations from ground truth values were observed for the low MVI exposures (1-2 MU); this was more so for the MVI/MVI pairs because of the

Table 2.1: Differences in ground truth for phantom translations at different exposures and beam energies in three directions

		Differences (mm)														
		1MU			2MU			4MU			8MU			32MU		
		X	Y	Z	X	Y	Z	X	Y	Z	X	Y	Z	X	Y	Z
MV/MV																
6MV	Mean	0.7	0.6	0.6	-0.1	0.9	0.8	0.3	0.6	0.1	-0.1	0.7	-0.1	-0.1	0.6	0.4
	SD	0.4	0.9	1.1	0.6	0.7	1.5	0.4	0.3	0.8	0.5	0.2	0.4	0.2	0.3	0.2
10MV	Mean	-0.1	0.5	0.0	0.2	0.4	0.2	-0.1	0.6	-0.1	-0.1	0.6	0.5	-0.1	0.5	0.5
	SD	0.7	0.4	1.0	0.6	0.3	0.6	0.5	0.3	0.6	0.5	0.2	0.5	0.2	0.2	0.1
18MV	Mean	-0.2	0.2	0.2	-0.2	0.3	0.5	-0.1	0.4	0.7	-0.1	0.4	0.6	-0.1	0.5	0.4
	SD	0.4	0.4	0.6	0.3	0.3	0.4	0.3	0.3	0.2	0.2	0.3	0.3	0.2	0.3	0.2
kV/MV																
6MV	Mean	-0.1	0.1	0.6	0.1	0.1	0.6	0.4	0.1	0.5	0.1	0.1	0.6	0.0	0.1	0.6
	SD	0.9	0.4	0.2	0.5	0.3	0.2	0.4	0.3	0.1	0.5	0.2	0.1	0.2	0.2	0.1
10MV	Mean	0.0	-0.1	0.5	0.1	-0.1	0.5	-0.1	-0.1	0.5	-0.2	-0.1	0.6	-0.2	-0.1	0.6
	SD	0.7	0.3	0.2	0.7	0.3	0.2	0.4	0.2	0.2	0.4	0.2	0.2	0.2	0.2	0.2
18MV	Mean	-0.2	-0.1	0.3	-0.3	0.0	0.4	-0.2	0.0	0.3	-0.2	0.0	0.3	-0.1	0.1	0.3
	SD	0.3	0.2	0.1	0.3	0.2	0.1	0.3	0.2	0.1	0.2	0.2	0.1	0.2	0.2	0.1

Abbreviations: MU = monitor unit; MV = megavoltage; kV = kilovoltage; SD = standard deviation.
Data shown for 2 cases, using both MV/MV and kV/MV image pairs.
For MV/MV image pairs, exposure pertained to both images.

lower image quality of the MVI compared with the kVI. This was also reflected in the lower success rate for MVI/MVI at the lowest exposures (Figure 2.4). The cumulative frequency distributions per beam energy of all the observed 3D deviations between the automated match and ground truth are shown in Figure 2.5. From the regular behavior of these distributions, it was apparent that although a cutoff level of 2 mm for success was applied, in the small fraction of failure cases, the errors were always < 3 mm. The best results (steepest descent in cumulative distribution) were obtained for the 18-MV beam.
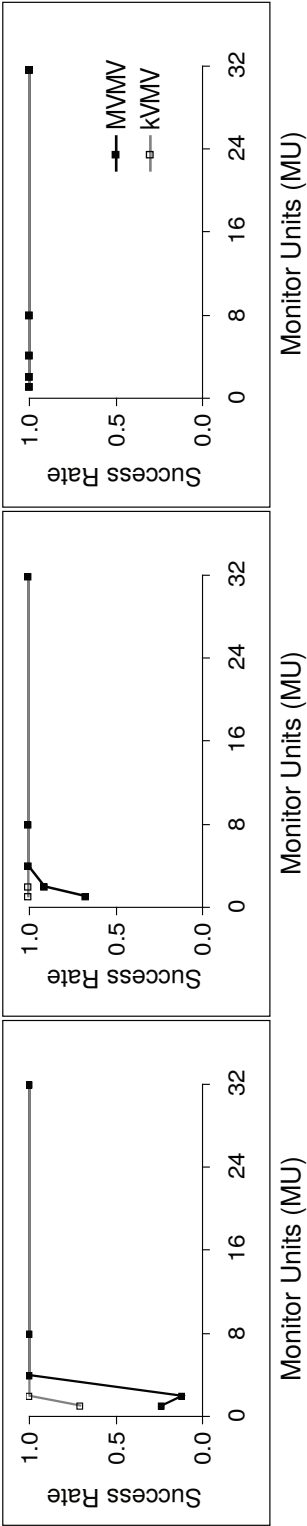
Figure 2.4: Image matching success rates (for marker translations) vs. monitor units at three beam energies for a phantom. KV/MV = initial stereographic targeting procedure using orthogonal kilovoltage image and megavoltage image combination. MV/MV = procedure using two orthogonal megavoltage images.
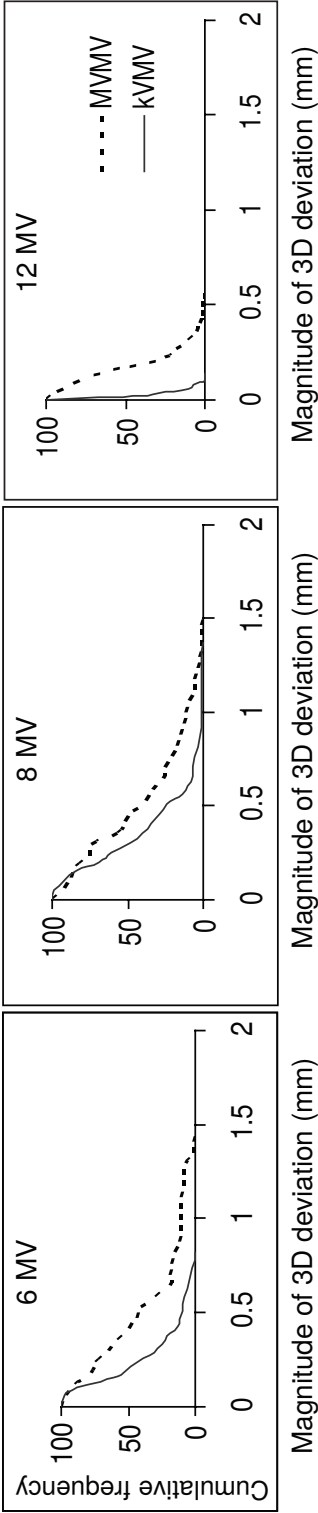
Figure 2.5: Cumulative frequency distributions of magnitudes of observed three-dimensional position deviations from ground truth as observed in experiments with phantom translations. For each energy, curves were constructed from data for all translations and megavoltage image exposures.

Table 2.2: Differences between SGT and ground truth for two exposures in experiments with combined translations and rotations

| | 6 MU | | | | | | 32 MU | | | | | |
| | Translation (mm) | | | Rotation (°) | | | Translation (mm) | | | Rotation (°) | | |
	X	Y	Z	Rx	Ry	Rz	X	Y	Z	Rx	Ry	Rz
MV/MV												
Mean	-0.1	0.6	0.1	-0.3	0.2	0.3	0.2	0.5	-0.2	-0.3	0.1	0.3
SD	0.4	0.4	0.7	0.8	0.7	0.6	0.4	0.2	0.3	0.4	0.5	0.4
Success Rate	70%						100%					
kV/MV												
Mean	0	0	0.3	-0.4	0.1	0.1	0.3	-0.1	0.2	-0.4	0.1	0.2
SD	0.4	0.2	0.3	0.6	0.5	0.4	0.3	0.2	0.3	0.4	0.5	0.3
Success Rate	100%						100%					

Abbreviations: SGT = stereographic targeting; R = rotation; MU = monitor unit; MV = megavoltage; kV = kilovoltage; SD = standard deviation;

Data shown for 2 cases, using both MV/MV and kV/MV image pairs; for MV/MV image pairs, exposure pertained to both images.

Success rates also shown for both image combinations.

2.3.2 Phantom verification: combined translations and rotations

Table 2.2 shows that even for the large combined rotations of = 20°, the kVI/MVI image pairs yielded a success rate of 100% for both studied MVI exposures. The success rate was scored as the match results for which the 3D magnitude of the difference with ground truth was < 2 mm for translations and < 2° for rotations. For the MVI/MVI image pairs, a 30% decrease in the success rate occurred with the lower MVI exposures. The reason for using a low exposure is evident; we wanted to deliver no more than a few MUs before correctly positioning the target volume. Hence, the combination of kVI and MVI used in SGT is superior to using EPIDs only.

2.3.3 TCSA accuracy

As can be seen in Table 2.3, the precision of the positioning achieved with TCSA was better than 0.3 ± 0.3 mm (mean ± SD) along all directions. This couch positioning precision was mainly limited by the TCSA tolerance setting of 0.3 mm, as well as the couch read-out accuracy.

2.3.4 Clinical results

Scatter plots of the deviations between the results obtained in the clinical application of SGT and ground truth are shown in Figure 2.6. The marker detection success rate

Table 2.3: Differences between prescribed and measured couch shifts obtained with TCSA

	Difference (mm)		
	LR	**CC**	**AP**
Mean	0.29	0.03	0.23
SD	0.27	0.21	0.28

Abbreviations: TCSA = Theraview Couch Set-up Assistant; LR = left-right; CC = craniocaudal; AP = anteroposterior.
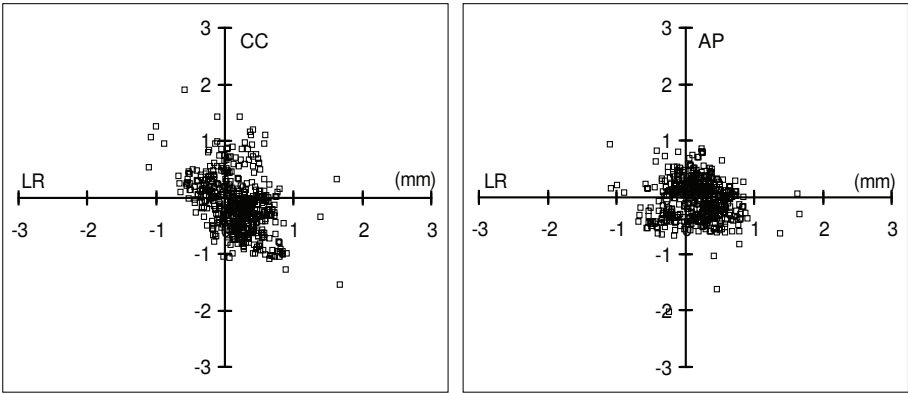

Figure 2.6: Scatterplots with deviations of prostate set-up errors (translational) measured in clinic with stereographic targeting and ground truth values obtained in manual offline analysis. AP = anteroposterior; CC = craniocaudal; LR = left-right.

for the clinical images was 99.6%, with most of the deviations from ground truth < 1 mm. The inaccuracy (mean ± SD) of the SGT match with respect to the ground truth was 0.2 ± 0.4 mm for the left-right, 0.1 ± 0.5 mm for craniocaudal, and 0.0 ± 0.4 mm for the anteroposterior direction. Table 2.4 summarizes the results of the measured

Table 2.4: Measured translational and rotational prostate positioning errors before and after SGT repositioning

	Translations (mm)						Rotations (°)					
	Σ_X	Σ_Y	Σ_Z	σ_X	σ_Y	σ_Z	Σ_{Rx}	Σ_{Ry}	Σ_{Rz}	σ_{Rx}	σ_{Ry}	σ_{Rz}
Pre SGT	1.7	4.1	2.9	1.6	2.7	3.2	4.9	1.3	1.7	4.2	1.6	1.3
Post SGT	0.2	0.5	0.4	0.6	0.7	0.8	5.0	1.4	1.9	3.9	1.6	1.3

Abbreviations: SGT = StereoGraphic Targeting; Σ = systematic error component; σ = random error component.

patient translational and rotational positioning (COM) errors before and after SGT positioning, accumulated for all treatment fractions. The small residual positioning errors obtained with SGT included the inaccuracies in the remotely controlled couch

shifts, inaccuracies in the COM translation obtained from the SGT match, and the intrafraction motion during the period between pre- and postcorrection images. Considering only the errors resulting from set-up (translation of the COM of the markers), the common equation of CTV-PTV margin = 2Σ + 0.7σ [26] resulted in margins > 12 mm without SGT and margins of about 2 mm after applying the SGT corrections. A cumulative histogram of 3D translational errors (3D vector length) of the COM of the prostate markers for all patients and fractions is shown in Figure 2.7, in which each 3D error represented the sum of the systematic and random error. Before SGT, the observed errors could exceed 10 mm in all directions but were reduced to < 3 mm after SGT. Furthermore, the procedure was fast. Considering the upper limits of the time ranges in Figure 2.2 revealed that SGT positioning was performed within 45 s/fraction.
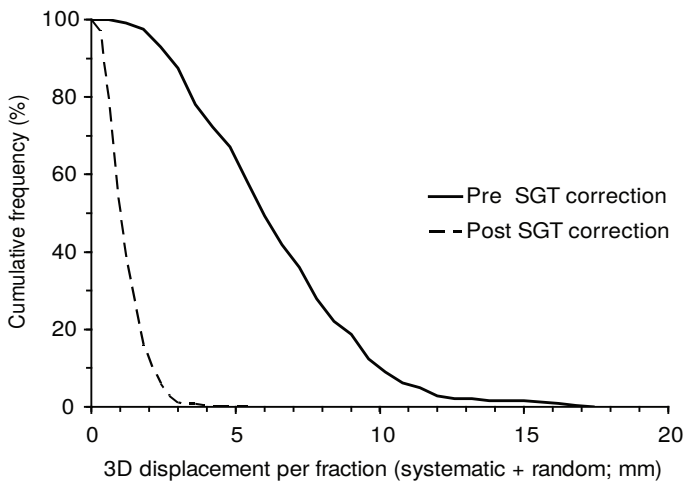
Figure 2.7: Cumulative frequency distribution of three-dimensional center-of-mass displacements of markers for all patients and fractions, before and after stereograhic targeting (SGT).

2.4 Discussion

Using SGT, the systematic and random errors were reduced to 0.5 mm and 0.8 mm (SD), respectively, within 1 min/treatment fraction. The crossfire imaging, accurate automatic match with a high success rate (> 99%), precise remote couch control system, and integration into one software environment are the ingredients that allow for this combination of speed and accuracy. Although in this study, the anteroposterior MV beam was used because it is a part of our treatment plan, the SGT can be started

at any gantry angle.

Apart from the combined kV/MV imaging, our approach to online prostate positioning might seem similar to other stereoscopic imaging systems such as the ExacTraC X-ray 6D system (BrainLab AG, Heimstetten, Germany) [48–50]. The published data on the final accuracy and timing achieved for prostate markers are limited, but the findings indicate that SGT is at least as accurate as the ExacTraC system [49]. A relevant difference is that SGT uses two imaging devices that have a use in their own right. The XVI system is also used for cone-beam CT acquisition to visualize soft tissues insufficiently visible on planar images (e.g., the seminal vesicles and rectum in the case of the prostate). Such information can be used in adaptive radiotherapy strategies [51, 52]. Furthermore, the EPID can be used for position verification without an additional kV dose (third to last paragraph before "Conclusion" section), as well as for EPID dosimetry [53]. Such flexibility is not offered by a dedicated planar imaging system such as the ExacTraC.

The combination of speed and accuracy for prostate positioning with implanted markers is hard to match with techniques relying on volumetric imaging alone [54]. Cone-beam strategies for the prostate will likely involve off-line correction schemes [51, 52], partly because of the workload, speed, and registration success rate, but also because the kV dose is not negligible. Off-line corrections might be less effective for the hypofractionation schemes currently under study for prostate RT [55, 56].

Although the importance of time trends for prostate targeting has not been fully established, a recent fiducial marker-based study indicated that the time trends must be taken into account for accurate prostate positioning ($\Sigma < 1$ mm) with off-line corrections [57]. We have recently proposed an off-line scheme to deal with the time trends [58]. The reduction of systematic and random positioning errors could be partially achieved with an adaptive strategy in which CT scans acquired during the initial week of treatment are used to estimate patient-specific PTVs in an offline manner [51]. Nevertheless, systematic and random positioning errors of < 1 mm (SD), regardless of the time trends, can only be achieved with an online approach.

The potential for planning margins as small as 2 mm when SGT is applied is hampered by various factors such as prostate rotation, intrafraction motion, target volume deformation, marker migration, and delineation (or generally, target definition) inaccuracies.

The measured prostate rotations (Table 2.4) are similar to the values reported in earlier studies [31, 39, 59, 60]. Various studies have shown that the prostate rotates mostly about the left-right axis, with the rotation center at the apex [39, 61]. If the

prostate position is corrected according to the COM of the markers, inadequate coverage could occur, especially near the base ("undercorrection") and apex ("overcorrection"), dependent on the chosen planning margin [39]. The measured COM displacements contain a contribution from the rotations, and the COM translation corrections are exact only at the COM position. The residual deviations at the prostate boundary depend on the prostate shape and size. For a perfectly spherical prostate with the marker COM at its center, the COM translation corrections will yield 0 residual errors along the entire prostate boundary (i.e., each point within the boundary will be covered by the boundary after correction), regardless of the rotations. We calculated the required margins for SGT in the case of the rotations (Table 2.4) for various prostate shapes, ranging from circular to flattened at the base and sharpened at the apex. We added in quadrature post-SGT translational errors and local distances between prostate hulls induced by rotations, as given in Table 2.4, to obtain the effective Σ and σ. Assuming a prostate base-apex length of 4 cm, application of a margin equation of $2\Sigma + 0.7\sigma$ yielded a maximal CTV-PTV margin of 4 mm. However, larger displacements can occur at the seminal vesicles, owing to rotations, as well as deformations [60, 62]. We are currently conducting a multiple CT study to investigate the motion of the seminal vesicles and prostate boundary (deformations) with respect to fiducial markers. In that study, we have included the residual errors resulting from prostate and seminal vesicle deformation into a population-based margin calculation to obtain well-defined margins for SGT. Furthermore, we are presently developing a strategy to correct for the rotational positioning errors using online selection of an optimal plan (matching the observed rotation) from a library of plans created for various prostate rotations. Because these plans could include seminal vesicle treatment, knowledge of the seminal vesicle motion in the presence of rotations is required to create optimally conformal plans.

Prostate intrafraction motion during EBRT has been well-studied [31, 37, 63, 64]. We are conducting a study on intrafraction motion for prostate cancer patients treated with SGT by acquisition of extra kVIs and MVIs during treatment. The initial results have indicated that the intrafraction motion is mainly random, with a SD of <1 mm in both the anteroposterior and the craniocaudal directions. Hence, the contribution to planning margins will be small compared with previously mentioned factors. Because of the speed of the SGT procedure, the intrafraction motion between the moment of prostate position measurement and treatment will be minimized and the intrafraction motion could be reduced further by repetition of the SGT procedure within one fraction (e.g., before each treatment beam). We are extending SGT with a system for continuous automatic detection of intrafraction motion using MVIs of the treatment beams (i.e., without an additional kV dose).

Marker migration and prostate deformation also contribute to the required planning margins. Recent studies have shown that the effect of marker migration is quite minimal for the prostate, and the overall effect of prostate deformations is <1 mm [60, 62]. In our study, no substantial migration of the markers was observed.

Finally, to fully use the possibility of margin reduction as a result of the reduction of patient positioning errors presented by SGT, one should minimize the delineation errors [60, 65, 66]. One can treat delineation errors as one of the sources of systematic errors [65], but care must be taken with this approach because delineation errors do not necessarily behave stochastically. For instance, the prostate volumes on CT tend to be systematically larger than those observed on MRI and ultrasonography in transversal slices. However, CT can systematically underestimate the volume near the superior and inferior boundaries [67, 68]. Apart from anatomic position, the magnitude of the intermodality and inter- and intraobserver differences is also dependent on the exact acquisition and delineation protocols applied. The use of a margin to account for small random delineation inaccuracies (e.g., intraobserver delineation errors) is reasonable. However, for systematic intermodality and interobserver variations, it is a rather crude tool. More promising approaches are offered by multimodality imaging and registration, as well as flexible delineation tools that allow for contouring in multiple planes simultaneously.

2.5 Conclusion

We have developed and clinically evaluated a fast and accurate procedure for daily online repositioning of the prostate using rapid sequential imaging of implanted markers with orthogonal kV and MV beams. The procedure is based on fully automated extraction and 3D registration of the imaged markers followed by remote couch control translations under control within a single software environment. This approach achieved residual systematic and random errors of < 0.8 mm (SD) in the three principal axes, with an addition of < 1 minute to the treatment time. Furthermore, the procedure limits the imaging-specific dose, because the MVI is obtained with the therapeutic dose and the planar kVIs are acquired for only one direction.

2.6 Acknowledgments

Day-to-day Reproducibility of Prostate Intrafraction Motion Assessed by Multiple kV and MV Imaging of Implanted Markers During Treatment

Theodore F. Mutanga, Hans C. J. de Boer, Vinayakrishnan Rajan, Maarten L. P. Dirkx, Luca Incrocci and Ben J. M. Heijmen

Abstract

Purpose

When performing online set up correction for prostate positioning errors prior to daily dose delivery, intrafraction motion can become a limiting factor to prostate targeting accuracy. The aim of this study was to quantify and characterise prostate intrafraction motion assessed by multiple kV and MV imaging of implanted markers during treatment for a large patient group.

Methods and Materials

Intrafraction motion in the sagittal plane was studied by retrospectively analysing displacements of implanted gold markers on (nearly) lateral kV and MV images obtained at various time points during the treatment fractions (on average 27 per patient) for 108 consecutive patients. The effective prostate motion in a fraction was defined as the time-weighted mean displacement.

Results

Prostate displacements in the sagittal plane increased during the fraction (on average 0.2 ± 0.2 mm per minute). Fourty percent of patients had a systematic (i.e. appearing in all fractions) effective displacement in the sagittal plane > 2 mm. Observed population systematic intrafraction motion ($\mu_{eff} \pm \Sigma_{eff}$) was 0.9 ± 1.1 mm and 0.6 ± 1.0 mm for the anterior-posterior and inferior-superior directions, respectively. Corresponding random motion (σ_{eff}) was 1.2 mm and 1.1 mm. Mean effective prostate motion in the first 5 fractions predicted for the mean effective displacement in remaining fractions (p<0.001).

Conclusion

For a large subgroup of patients the systematic component of intrafraction prostate motion was substantial. Intrafraction motion correction prior to each beam delivery or offline corrections could likely be beneficial for the subgroup of patients with significant motion. The systematic component is well predicted by measurements in the first fractions.

3.1   Introduction

In radiotherapy, variations in the position of the target between different treatment days (i.e., interfraction) and during a treatment fraction (i.e., intrafraction) present limitations to the accuracy and effectiveness of the delivered dose. To account for this, planning margins are generally added to the clinical target volume (CTV), yielding the planning target volume (PTV) to which the dose is prescribed [23]. To determine the size of the required margins, population based inter- and intrafraction position errors must be quantified accurately. When online correction of the set up errors is performed, there might be some residual errors due to limitations in the measurement and application of corrections. These residual errors should also be measured and taken into account when designing planning margins.

We previously implemented a fully automated and accurate daily (interfraction) position correction method (Stereographic Targeting, SGT) [69] based on imaging of prostate-implanted gold markers. The small residual errors achieved with SGT allow for reduced planning margins. However, intrafraction motion limits the achievable margin reduction. Intrafraction motion of the prostate has been associated with changes in rectal and bladder content, and to a lesser extent respiratory motion [70]. In our own experience, changes in the patient posture are also of importance (e.g. relaxation of pelvic muscles). Published data in studies using a variety of monitoring methods including ultrasound [71], magnetic resonance imaging [64], implanted electromagnetic transponders [72], portal, volumetric and fluoroscopic [31, 73, 74] imaging of implanted markers suggest that significant intrafraction motion occurs frequently during the treatment delivery times encountered in intensity modulated radiotherapy (IMRT).

Most commonly, the extent of prostate motion during treatment is derived by pre- and post-treatment imaging of the prostate or surrogates. Generally, the difference in position at both time points is quantified as intrafraction motion. However, for the time within which IMRT beams are delivered (11 minutes in our institute), the prostate can exhibit various types of motion from random, to transient, to constant drifts. Frequent imaging or even continuous online tracking of the prostate is therefore needed to obtain accurate intrafraction motion characteristics. Studies based on continuous tracking of the prostate by means of electromagnetic transponders [72, 75, 76] provide information on intrafraction motion data with the highest temporal resolution. However, in these studies, intrafraction motion patterns in individual fractions for a small number of patients are often presented [76], with little information on the day-to-day reproducibility of intrafraction motion. If such reproducibility

exists, it could introduce a systematic error that is not corrected for by commonly applied online corrections just prior to dose delivery. Knowledge of such systematic components is also paramount for accurate planning margin calculations [25, 26]. In this study, we report on characteristics of intrafraction motion and estimate the systematic and random components by means of multiple kV and MV imaging of implanted markers within the treatment fraction. We investigate if there is a significant subgroup of patients for which the intrafraction motion reproduces from day-to-day.

3.2 Methods and Materials

3.2.1 Patients and treatment technique

This study included 108 consecutive patients treated at our institute in a randomised trial comparing a conventional fractionation scheme (39 x 2 Gy, 5 times a week) and a hypofractionated scheme (19 x 3.4 Gy, 3 times a week). For daily position verification, 3-4 gold markers (cylinder with a diameter of 1 mm and a height of 5 mm) were implanted transperinnealy in the prostate under transrectal ultrasound guidance. The acquisition of the planning CT was scheduled at least one week after marker implantation to allow any possible edema to resolve. The patients were treated with an isocentric IMRT treatment plan with 10 MV photon beams from gantry angles of 0°, 155°, 110°, 50°, 305°, 255° and 205° (Figure 3.1). The applied order of beam angles in dose delivery assured a minimal gantry travel path. The CTV included the prostate and seminal vesicles. Planning margins of 5 and 8 mm, respectively, were added to these organs to get the PTV. At least 99% of the PTV was planned to get 95% of the prescription dose and a maximum dose of 107% was allowed. The dose constraint for the rectum was such that 35% of the volume would receive maximally 83% of the prescription dose. Our planning procedure ensures that the first segment of each treatment beam encompasses all markers and contains 6 monitor units (MU). These segments are used for imaging and allow the possibility to track marker positions throughout treatment.

All patients were treated in the supine position with a head rest and knee support. No further fixation devices were used. In order to maintain a uniform bladder volume, the patients were instructed to void their bladders 30 minutes before treatment and then drink 2 cups of water just before start of treatment. Laxatives were used for the planning CT but not during treatment. Patients did not receive instructions for emptying the rectum before the treatment and no specific diet was prescribed.
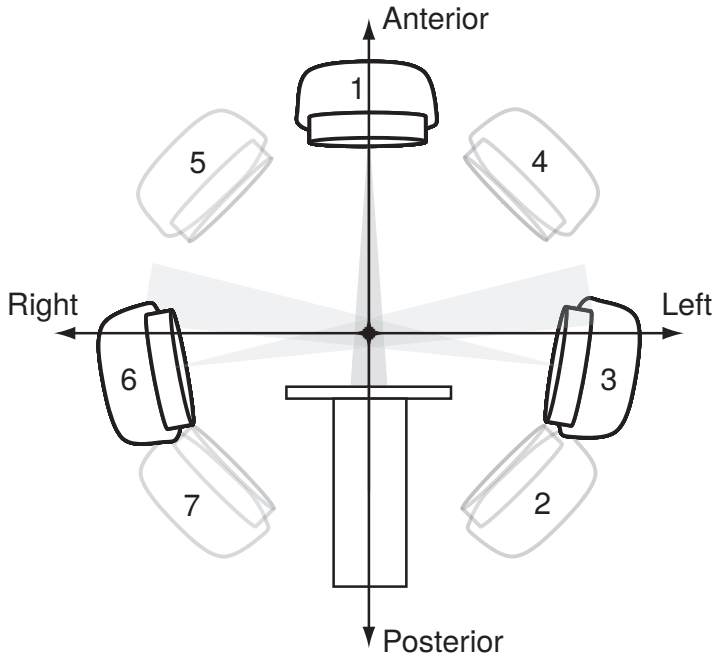
Figure 3.1: Beam arrangement and order (numbers) of our 7 field IMRT treatment technique. Online corrections were based on a crossfire of the first MV treatment beam (beam 1) and kV imaging. Analyses of intrafraction motion were in part based on EPID Images obtained with the nearly lateral treatment beams (3 and 6).

3.2.2 Pre-treatment imaging and prostate positioning

To allow for the small planning margins we use in our prostate treatments, all patients were treated with our previously reported online SGT automated positioning strategy implemented on the Synergy linear accelerator (Elekta, Crawley UK), using Theraview Technology imaging software (Cablon Medical, Leusden, the Netherlands). Prior to each treatment, patients were first positioned using the room lasers and skin tattoos. The SGT procedure was then applied as outlined in the following steps. 1) Markers were imaged with the EPID using the first 6 MUs of the first treatment beam (beam 1 in Figure 3.1) and orthogonal kV imaging. 2) Markers in the orthogonal kV and MV images were automatically segmented and used to derive the 3D marker centre of mass (COM) position. 3) By comparing with the COM position in the planning CT, the 3D translational displacements were obtained. 4) Any 3D set-up deviation greater than 2 mm in magnitude was corrected using couch

shifts via an integrated remote couch control. 5) A lateral verification kV image was acquired to verify applied corrections and if necessary, another correction was made before proceeding with the treatment. For all fractions, the last kV image taken before the delivery of the treatment beams was denoted as the kVpre image and used for intrafraction motion analysis (see next section *"Analysis of intrafraction motion"*). All steps in the imaging and set-up correction procedure were managed by the SGT Workflow manager present in the Theraview software. This process only requires user actions for approval of the automatically generated marker registrations and proposed couch shifts.

3.2.3 Analysis of intrafraction motion

To study intrafraction motion we used the kVpre images and MV images from the treatment beams at 110º (LeLatMV, beam 3 in Figure 3.1) and 255º (RiLatMV, beam 6 in Figure 3.1). Additionally, in each fraction we acquired a 90º kV image (kVpost) after delivery of the last IMRT beam, which was also used in the analyses. The main reasons for choosing these (almost) lateral beams are: 1. intrafraction motion predominantly occurs in the sagittal plane [31, 71, 77] and 2. Management of sagittal plane motion is the most crucial to minimize planning margins towards the most relevant organs at risk (rectum, and bladder and penile bulb). Furthermore, for the selected beam directions, the superior-inferior (SI) intrafraction displacement is derived exactly from the vertical marker displacements in the images whereas the anterior-posterior (AP) displacement is exact in the kV images and almost exact to the horizontal shift in the MV images. For the nearly lateral MV beams, exact AP shifts were derived by taking the ratio of the measured displacements to the sine of the gantry angle. Errors in using approximate AP shifts were better than 0.2 ± 0.3 mm (1 SD). For all (nearly) lateral images, the Theraview software was used for automatic marker detection and assessment of the 2D marker COM displacement in the sagittal plane relative to its position in the corresponding digitally reconstructed radiograph (DRR), derived from the planning CT-scan. Two experienced radiographers involved with daily patient set-up were enrolled to manually identify marker positions on all images. Figure 3.2 shows sample images together with the average elapsed time between imaging points. Although the success rate of the automatic markers matching was high (>90%), for the purpose of this study, the two involved radiographers also verified the accuracy of the automatic match results. This was done to ensure the highest accuracy in the obtained marker positions in all images.

For each patient and each treatment fraction, the COM displacements in the
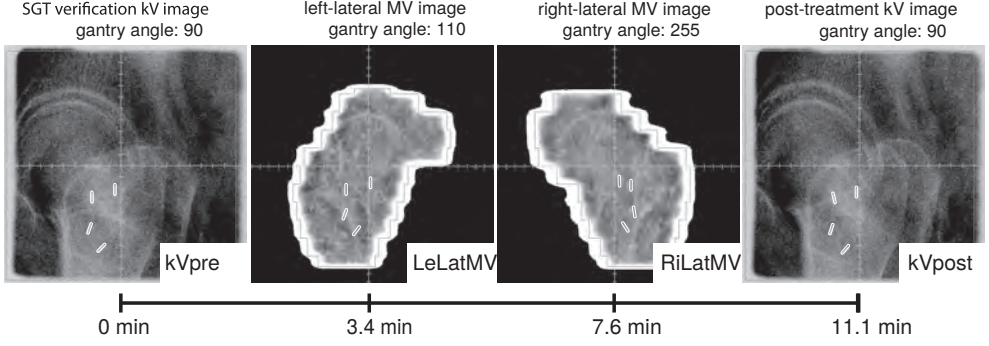
Figure 3.2: Time points for acquisition of the kV and MV images used for analyzing intrafraction motion, and sample

sagittal plane, derived at the four imaging time points, were stored in combination with the elapsed times from acquiring kVpre for further analysis. Because kVpre is obtained very shortly after performing an SGT correction (typically within 10 seconds), the observed displacements in this image mainly reflect residues from the correction procedure using the applied 2 mm correction action level and some (minor) intrafraction motion. For each fraction, the effective intrafraction displacement δ_{eff}^d for direction d was calculated using:

$$\delta_{eff}^d = \left[\frac{\left(\Delta t_{1,2} \cdot \left(\left(\delta_1^d + \delta_2^d\right)/2\right) + \Delta t_{2,3} \cdot \left(\left(\delta_2^d + \delta_3^d\right)/2\right) + \Delta t_{3,4} \cdot \left(\left(\delta_3^d + \delta_4^d\right)/2\right)\right)}{\Delta t_{1,2} + \Delta t_{2,3} + \Delta t_{3,4}} \right]$$
(3.1)

with indices 1, 2, 3, and 4 referring to set-up measurements based on kVpre, LeLatMV, RiLatMV, and kVpost, respectively. $\Delta t_{l,m}$ is the time difference between measurements l and m, $\delta_n{}^d$ is the set-up deviation in measurement n ($n = 1, 2, 3, 4$).

3.2.4 Reproducibility of intrafraction motion

To investigate the day-to-day reproducibility of intrafraction motion, for each patient and time point, the mean marker COM displacement and the SD over all treatment fractions were calculated. A similar analysis was performed for the effective intrafraction displacements, calculated with Eqn. 3.1. This data was used to derive for each time point and for the effective intrafraction motions population mean systematic errors (μ) and the corresponding standard deviation (Σ). The population random errors (σ) were computed as the root-mean-square of all patients random set-up errors. For each patient, linear regression analysis was used to compare the

mean effective displacement in the initial week of treatment to that in subsequent treatment weeks. A p-value < 0.05 was considered significant.

3.2.5 Effect of treatment time on intrafraction motion

To study the effect of treatment time on intrafraction motion, we obtained data from another group of prostate patients (n = 10) who were previously treated at our institution. The average treatment time of this group was 4.8 (±0.3) minutes. This shorter treatment time is due to irradiation with a smaller fraction dose (1.8-2 Gy), 3 static instead of 7 IMRT fields and a dose rate 600 MU/minute instead of 300 MU/min. We compared the effective intrafraction displacements observed in this group of patients to those observed in the larger patient population with longer treatment times.

3.3 Results

3.3.1 Intrafraction motion

For the 108 patients, MV and kV images from 2894 fractions were used for evaluation. Marker displacements were obtained from 5788 MV images and 5618 kV images. The post kV image was not acquired for some fractions (2.9%) either due to technician negligence or time constraints. Note that this post kV image was not part of our standard clinical protocol. Table 3.1 lists the means and standard deviations

Table 3.1: Interval times in minutes between imaging time points after SGT corrections and kV correction verification.

	kVpre-LeLatMV	LeLatMV-RiLatMV	RiLatMV-kVpost	Total
Mean	3.4	4.2	3.5	11.1
SD	1	1	1.5	2.2

kVpre and kVpost are pre and post kV image points
LeLatMV and RiLatMV are time points for beam 3 and beam 6, see Figure 3.2

(SD) of the interval times between image acquisitions after the SGT set up correction was performed. The intrafraction motion reported in this study occurred in a mean time interval of 11.1 ± 2.2 minutes (1SD). Scatter plots of the measured displacements in the sagittal plane at all time points are shown in Figure 3.3. There is a gradual increase in the spread of the displacements with increasing time and the shape of the distributions is consistent with previously reported prostate motion and rotations about the left-right axis. This would also be consistent with the idea that motion
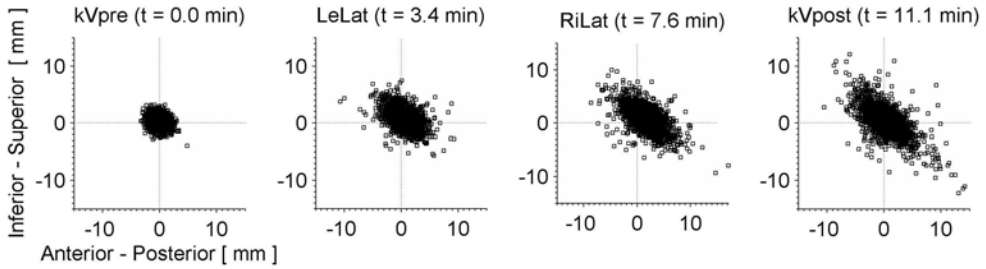
Figure 3.3: Scatter plots of COM displacements in the sagittal plane at various times.

of the prostate is driven by changes in the rectum and bladder content. On average, the increase in the magnitude of intrafraction displacements during a fraction for our patient population was 0.2 ± 0.2 mm per minute. Figure 3.4 shows cumula-
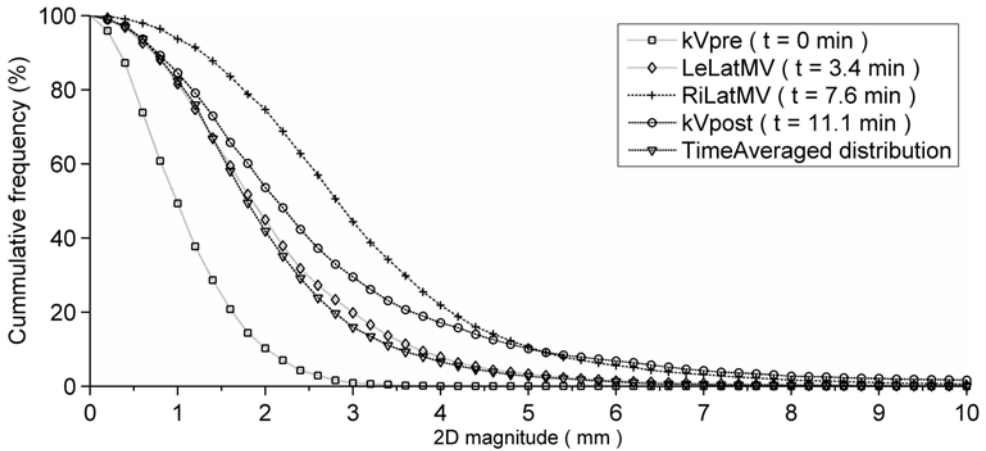
Figure 3.4: Cumulative histograms for 2D centre-of-mass (COM) displacements (systematic+random) in the sagittal plane at the different time points and for the effective displacement

tive histograms of displacements for all patients and all fractions, observed at times after SGT imaging (and online corrections). Ninety percent of the displacements derived from kVpre images were less than 2 mm. With perfect corrections and lack of intrafraction motion, this would have been 100%. The observed displacements increased steadily during the treatment when going from kVpre to LeLatMV and Rilat-MV. There appears to be a slight drop in the magnitudes when going from RiLatMV to kVpost. However, as can be seen also from the scatter plots in Figure 3.3, at the same time there is a net shift of the displacements in the Posterior Superior direction for the MV distributions. We quantified this net shift at the MV beam measurement

points to be <1.8 mm. This is possibly related to gantry hysteresis and will be investigated further. Nevertheless, at kVpost, the percentage of displacements larger than 5 mm was still higher than for RiLatMV. Table 3.2 summarizes the population-

Table 3.2: Intrafraction motion population characteristics at several time points and for the effective (time-averaged) distribution.

	kVpre		LeLatMV		RiLatMV		kVpost		Effective[1]	
	AP	CC	AP	CC	AP	CC	AP	CC	AP	CC
μ (mm)	0	0.3	0.5	0.8	1.8	0.7	0.6	0.3	0.9	0.6
Σ (mm)	0.5	0.5	1.1	1	1.6	1.3	1.7	1.4	1.1	1
σ (mm)	0.7	0.7	1.3	1.2	1.7	1.5	1.8	1.9	1.2	1.1

[1] Derived from time-weighted intrafraction displacements.
Abbreviations: CC = cranial-caudal; AP = anterior-posterior;

based values of μ, Σ and σ for the COM displacements at all time points as well as for the time-averaged (effective) displacements (Σ_{eff} and σ_{eff}). The systematic errors obtained directly after SGT correction, i.e. 0.0 ± 0.5 mm in the AP direction and 0.3 ± 0.5 mm in the CC direction, increased by $\mu_{eff} \pm \Sigma_{eff} = 0.9 \pm 1.1$ mm respectively 0.6 ± 1.0 mm due to intrafraction motion, in agreement with Figures 3.3 and 3.4.

3.3.2 Reproducibility of intrafraction motion

The non-zero μ_{eff} and Σ_{eff} shown in Table 3.2 indicate that intrafraction motion has a non-negligible systematic component. Figure 3.5 shows the cumulative histogram

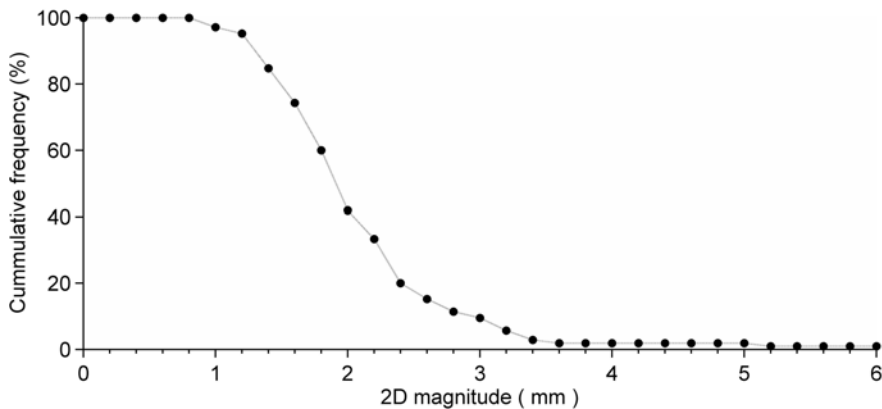**Figure 3.5:** Cumulative histogram of observed systematic intrafraction displacements in the sagittal plane. For each fraction of a patient, Eqn. 3.1 was used to assess the effective prostate set-up error. The curve was then constructed using for each patient the mean effective prostate set-up error over all fractions.

of the observed mean effective displacement per patient. Significant subgroups of

patients had systematic effective displacements greater than 2 mm (40%) and 3mm (10%). Figure 3.6 shows statistically significant correlations (p-value < 0.05) between patients' mean effective displacements in the initial 5 days of treatment with those in the subsequent days of treatment. This suggests that measurements in the initial fractions may be used to predict and correct patient systematic intrafraction prostate displacement in the remainder of the fractions. Figure 3.7 shows an example of a
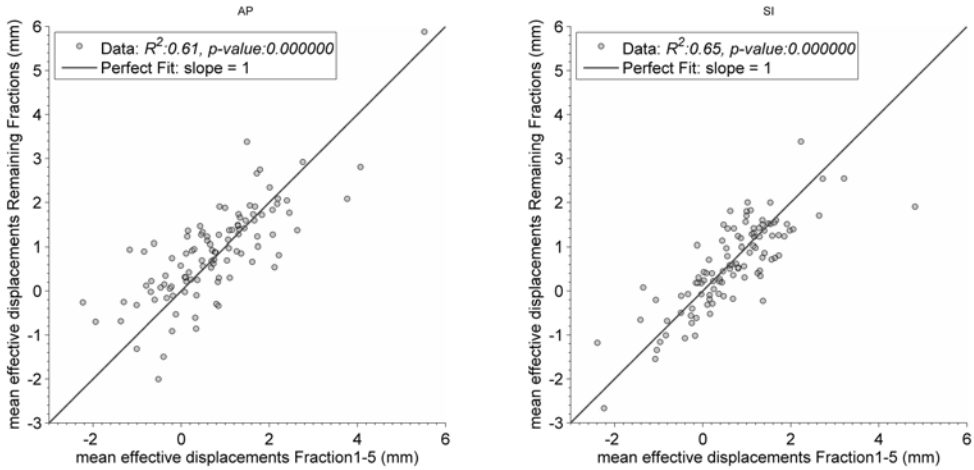
Figure 3.6: Correlation between mean effective displacements in the first 5 fractions with mean effective displacements in subsequent treatment weeks in the anterior-posterior (AP) and superior-inferior (SI) directions.

patient in which part of the intrafraction motion is caused by reproducible motion of the whole pelvic anatomy between start and end of treatment in four fractions. This observation recurred in at least 5 of the 108 patients, and indicates that systematic intrafraction motion is not only due to changes in bladder or rectal filling.

3.3.3 Effect of treatment time

We compared μ_{eff}, Σ_{eff} and σ_{eff} obtained between the groups of patients with long (11.1 minutes) and short (4.8 minutes) treatment times. Although the error distribution at kVpre after SGT correction was very similar between the two groups, intrafraction motion hardly deteriorated the initial set-up accuracy in the group with shorter treatment times: $\mu_{eff} \pm \Sigma_{eff}$ = -0.1 ± 0.6 mm in CC direction and 0.3 ± 0.6 mm in AP direction (p-value <0.01).
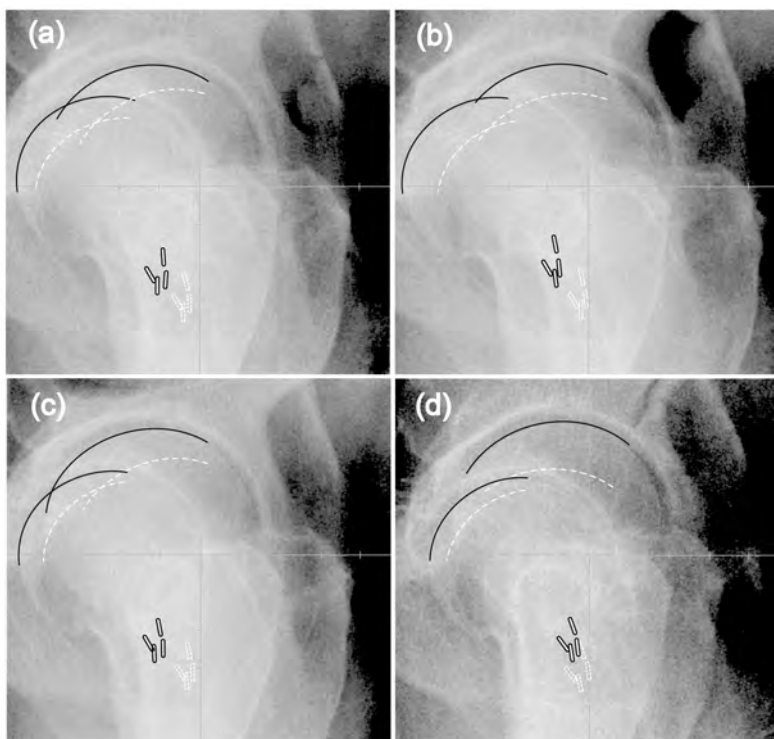
Figure 3.7: Sample images indicating systematic motion of markers as well as pelvic bony anatomy. Panels (a) - (d) correspond to fraction 1-4 of a representative patient. Solid black contours are from the kVpost image while dotted white contours are from the kVpre image of the corresponding fraction.

3.4 Discussion

In this paper, intrafraction motion was studied by performing measurements at several time points in IMRT treatment fractions for a large patient group. The main findings are 1) intrafraction motion distributions get broader with elapsed time (Figures 3.3 and 3.4, Table 3.2), 2) a significant component of the motion is systematic, i.e. reproducing from day-to-day (Table 3.2, Figure 3.5), 3) The systematic component of intrafraction motion can be predicted from measurements in the first 5 fractions (Figure 3.6), 4) Without the use of an appropriate protocol for correction of (systematic) intrafraction motion or adequate planning margins, a significant portion of patients may be at risk for partial tumor miss. The observation that systematic motion can be predicted by measurements performed in the first treatment week can be used to design correction protocols with acceptable imaging (analysis) workload.

A comparison of the observed motion magnitudes for patients with fraction dose

delivery times > 11 minutes to another group of patients with shorter fraction durations (< 5 minutes) showed an increase in intrafraction motion (p-value < 0.01). Although this increase in intrafraction motion with increased fraction duration has been observed in previous studies [77, 78], the day-to-day reproducibility of intrafraction motion (demonstrating systematic errors) has not been specifically reported

Most studies analyze intrafraction motion using images acquired before treatment and images acquired after treatment [31, 71]. This implies that motions occurring during the time frame between the two images that have already resolved by the end of treatment will be missed. A recent study shows that the sensitivity of using pre- and post-treatment imaging to estimate intrafraction motion during treatment is low [79], highlighting the need for more frequent imaging within the fraction to monitor intrafraction motion. Kotte et al. [77] studied the intrafraction motion on a large population (427) of patients, with treatment times of 5-7 minutes per fraction, by registering fiducial markers on portal images obtained at different time points within a fraction. Even though they found reversal of motion at times, a systematic increase of the frequency of set-up errors > 2 mm was observed with increase in time. The effective systematic errors we report are higher than those reported by Kotte et.al. (Σ_{eff} <= 1.1 mm vs. Σ = 0.6mm) due to the longer (almost double) treatment times for our IMRT treatments. In the study of Kotte et.al., there was no analysis on the predictability of systematic errors from measurements in initial fractions. The intrafraction motion SDs reported by Li et al. [80] using real-time tracking of the prostate with the Calypso$^{©}$ system and electromagnetic transponders are comparable to the effective SDs found in our study (Σ_{eff} <= 1.1 mm vs. Σ = 0.9 mm) and σ_{eff} = 1.2mm vs. σ = 1.6mm). It is interesting to see that we obtain similar findings even though we used a relatively simple 2D analysis on portal kV and MV images. The observed widening of prostate intrafraction motion distributions with time can be caused by a number of factors including increased probability of rectal activity and bladder filling [70] or (as observed here) movement due to relaxation and contraction of pelvic muscles and patient discomfort. From observations of displacements on kVpre and kVpost images, movements of the pelvic bony anatomy reproduced daily in some patients, thereby contributing to the systematic intrafraction displacements. This effect has not been clearly identified in previous studies. Figure 3.7 shows an example of such reproducible motion of the whole pelvic bony anatomy observed for one patient in four fractions. This reproducible motion was observed in 20 fractions for this particular patient.

It was reported earlier that rectum filling has significant influence on prostate motion observed in MRI based studies during time intervals relevant for radiothera-

py [64, 81, 82]. However, the systematic error reported by these studies is significantly lower compared to our results. Induced discomfort in maintaining a full bladder during treatment may be responsible for part of the systematic motion we find. Various immobilization strategies [61, 83, 84], and controlled diet and rectum filling [64, 82] are also being practiced by different groups, but it has yet to be demonstrated that these approaches reduce (systematic) intrafraction motion [85].

Information on intrafraction motion is only part of the knowledge needed to fully evaluate planning margins. Other residue errors after daily online re-positioning result from prostate deformation and delineation uncertainties [65, 86]. We previously quantified deformation of the prostate and seminal vesicles relative to prostate implanted markers with and without rotations [86]. The observed magnitudes of deformation indicate that deformation errors play a significant role, limiting achievable margin reduction when introducing daily online corrections. Furthermore, we developed a method [87] to evaluate the actual delivered dose in marker-based prostate radiotherapy taking into account all known geometric errors, including intrafraction motion. Such analysis is necessary to understand the clinical impact of the effect of the measured errors [88]. Figure 3.5 shows that around 40% of patients have a systematic effective intrafraction prostate motion of 2 mm or more. These patients could benefit from a protocol that corrects this motion. We have demonstrated that measurements in the first 5 treatment fractions may be used to predict the systematic component of intrafraction motion, allowing the use of an offline No Action Level (NAL) [39] correction protocol to reduce these errors. Recently we implemented an extension to the SGT procedure, allowing correction of both random and systematic intrafraction motion prior to each beam delivery.

3.5 Conclusion

Intrafraction prostate motion can severely impact treatment. This is largely caused by the significant systematic component (reproducing from fraction to fraction), as observed for a large portion of patients (40% with a mean set-up error of 2 mm or more). Measurements in the first fractions can be used to estimate expected mean errors in the remainder of the treatment, allowing development of time and workload efficient correction strategies.

3.6   Acknowledgements

CHAPTER 4

Software-Controlled, Highly Automated Intrafraction Prostate Motion Correction with Intrafraction StereoGraphic Targeting (iSGT): System Description and Clinical Results

Theodore F. Mutanga, Hans C. J. de Boer, Vinayakrishnan Rajan, Maarten L. P. Dirkx, Marjolein J. H. van Os, Luca Incrocci, Ben J. M. Heijmen

Abstract

Purpose

A new system for software-controlled and highly automated correction of infraction prostate motion, intrafraction StereoGraphic Targeting (iSGT), is described and evaluated.

Methods and Materials

At our institute, daily prostate positioning before delivery of the first IMRT beam is routinely achieved with stereographic targeting (SGT), which involves automated orthogonal kV/MV imaging of implanted markers, image registration, and remote couch translations to correct detected set-up errors. iSGT entails MV image acquisitions with the first segment of selected subsequent IMRT beams, followed by remote couch repositioning to correct for intrafraction motion above a pre-defined threshold, prior to delivery of the remainder of the segments. iSGT was implemented by extension of the SGT software to facilitate fast and accurate intrafraction set-up corrections with minimal user interaction. For a group of 120 patients, iSGT with corrections for two nearly lateral beams was evaluated in terms of workload and impact on effective intrafraction displacements in the sagittal plane.

Results

SDs of Systematic (Σ) and random (σ) displacements relative to planning measured directly after initial SGT set-up correction were < 0.5 mm and < 0.8 mm respectively. Without iSGT corrections, effective Σ and σ for the 11 minutes treatments would have grown to Σ_{eff} < 1.1 mm and σ_{eff} < 1.2 mm. With the iSGT procedure with an action level of 4 mm, effective positioning errors were reduced to Σ_{eff} < 0.8mm and σ_{eff} < 1.0 mm with 21.7% of all fractions requiring a correction. Computer simulations demonstrated that using an action level of 2 mm, the errors would have been reduced to Σ_{eff} < 0.6 mm and σ_{eff} < 0.7 mm with corrections in 46.6% of the fractions. Because iSGT is highly automated, the extra time added by iSGT is < 30 seconds if a correction is required.

Conclusion

Without increasing imaging dose, iSGT successfully reduces intrafraction prostate motion with minimal workload and increase in fraction time. An action level of 2 mm is recommended.

4.1   Introduction

A major challenge in the current application of prostate external beam radiotherapy is intrafraction target motion [89]. Using a variety of monitoring methods including magnetic resonance imaging (MRI), real-time tracking with implanted electromagnetic transponders, kilo voltage (kV) and megavoltage (MV) imaging of implanted fiducials, it has been shown that prostate intrafraction motion occurs frequently for IMRT delivery times [31, 64, 71, 72]. Intrafraction prostate motion is associated with changes in rectal and bladder content [64], respiratory motion and in our own experience changes in overall patient posture [64, 90]. Several studies [38, 63, 77] quantify inter- and intrafraction prostate motion using implanted markers, but few [91, 92] have comprehensively reported methods for dealing with intrafraction motion when using X-ray localization of implanted markers. Generally, intrafraction motion remains uncorrected and planning margins are extended [23–26]. The required extension depends on the dose conformity and steepness of dose gradients of the treatment technique as well as on the target localization technique [87, 88].

We previously reported the clinical implementation of stereographic targeting (SGT) for fast and accurate daily prostate positioning using automated orthogonal kV/MV imaging of implanted fiducial markers, fast and reliable marker detection and registration, and remote couch control for set-up correction [69]. With SGT, residual interfraction systematic and random positioning uncertainties were small (SD < 0.9 mm). In a recent study [90], using kV/MV imaging of implanted markers at multiple time points during treatment, we observed significant random and, more importantly, systematic intrafraction motion, i.e. intrafraction motion that reproduced from day-to-day. Depending on the patient, the high initial fraction set-up accuracy achieved with SGT could seriously deteriorate during the treatment fractions. In the current study, we report on the design, implementation and evaluation of our new system for daily prostate positioning including intrafraction set-up corrections, designated intrafraction StereoGraphic Targeting (iSGT). In iSGT intial positioning in a fraction is performed with SGT. Subsequent intrafraction corrections are based on acquired EPID images of the first segments of selected IMRT beams. With the automated MV image acquisitions, fast and reliable marker matching and automated couch shifts, iSGT aims for accurate prostate positioning with minimal user interaction, limited added treatment time, and no extra imaging dose.

4.2 Methods and Materials

4.2.1 Patients, treatment, equipment and image acquisition

We included 120 patients who participated in a nationwide randomised trial comparing a conventional fractionation scheme (39 x 2 Gy, 5 times a week) and a hypofractionated scheme (19 x 3.4 Gy, 3 times a week). All patients had 3-4 gold markers (cylinder of diameter =1 mm and height =5 mm) implanted in the prostate for set-up corrections. The corrections were executed using remote treatment couch control (no entrance in the treatment room) with a dedicated couch control system (Theraview Couch Set-up Assistant ((TCSA); Cablon Medical, Leusden, The Netherlands), with a couch repositioning accuracy of SD 0.3 mm [69]. Treatments were performed at Synergy (Elekta, Crawley, UK) linear accelerators with a 7-field IMRT technique with beams at gantry angles 0º, 95º, 110 º, 50º, 305º, 255º and 205º (Figure 4.1).
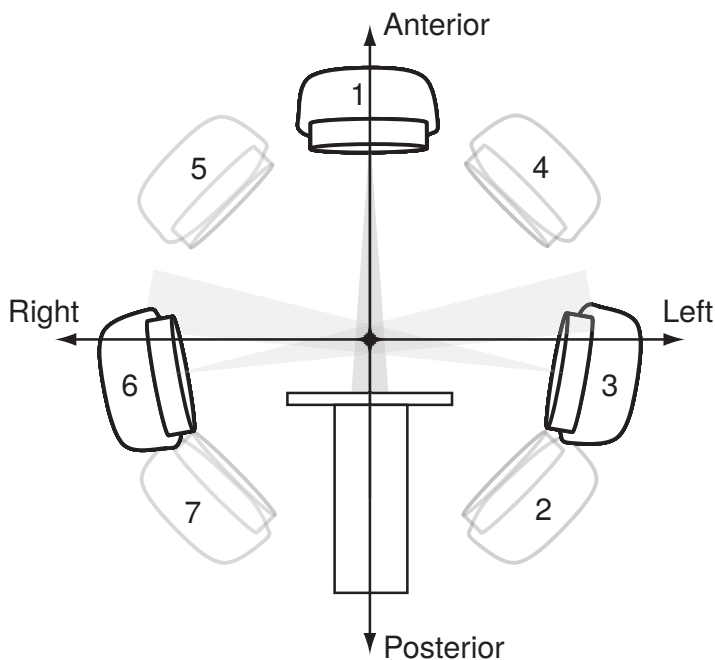

Figure 4.1: Beams for the 7-field IMRT technique. Beam 1 is used in combination with an orthogonal kV beam for 3D pre-treatment SGT corrections, while beams 3 and 6 are used for iSGT intrafraction corrections in the sagittal plane.

The analysis of intrafraction prostate motion correction was based on acquired kV images (kVI) and MV images (MVI). For each patient fraction, the first image used was "kVIpre", a lateral kVI acquired with the XVI system (Elekta, Crawley UK) at the end of the initial SGT prostate set-up procedure, prior to the start of treatment (details below). For research purposes, IMRT fields were designed with a field encompassing first segment containing 2-6 MU [42]. MVI were automatically acquired for these segments using Theraview NT electronic portal imaging devices (EPID) (Cablon Medical, Leusden, The Netherlands). After delivery of all fields, a final lateral kVI, designated "kVIpost", was always acquired. For the first 20 patients in this study no intrafraction corrections were performed and the acquired kVIpre, kVIpost and MVI were used to establish parameters for the use of MVI for intrafraction corrections (iSGT) in subsequent patients. Data from 100 of these patients were available for clinical evaluation of iSGT.

4.2.2 Initial prostate positioning in iSGT

The procedure for initial prostate positioning in iSGT prior to delivery of the first beam is similar to the SGT procedure described in details in [69], and schematically depicted in Figure 4.2. In summary, for gantry angle 0º, a megavoltage image (MVI) and an orthogonal kilovoltage image (kVI) are acquired in rapid succession to image the implanted gold markers. The 3D marker group center of mass (COM) position is then reconstructed in < 2sec with a success rate of 99% [69]. The deviation of the COM position from planning is then used as input for the TCSA system (above) for remote couch repositioning, considering a 3D correction vector length threshold of 2 mm. After repositioning, either a new MVI/kVI pair, or just a lateral kVI is obtained for verification purposes and if necessary for further correction. The last kVI acquired is designated kVIpre and used for the analyses of intrafraction motion correction in this paper.

4.2.3 Intrafraction motion correction in iSGT; the workflow

The iSGT workflow schematically illustrated in Figures 4.1 and 4.2 was implemented in the Theraview NT software in collaboration between Erasmus MC and Cablon Medical. The numbers in Figure 4.1 show the order of delivered beams. In the current iSGT design, only MVI for the two (nearly) lateral beams (3 and 6 in Figure 4.1) are used. These MVI will be denoted MVI-3 and MVI-6, respectively. Considering the order of delivered beams (Figure 4.1), beams 3 and 6 have favorite (symmetric) time points. Moreover, prostate intrafraction motion occurs predominantly in the sagittal
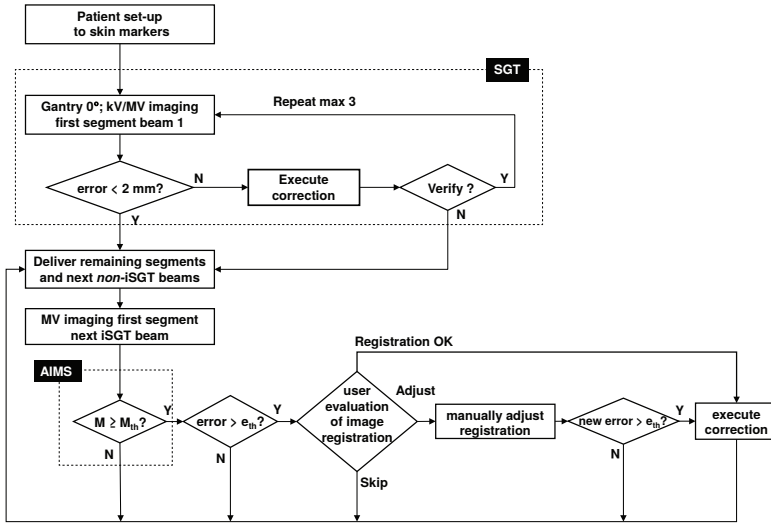
Figure 4.2: intrafraction StereoGraphic Targeting (iSGT) workflow. Abbreviations: AM= automated match, e_{th} = error threshold for correction in mm; AIMS = automated identification of marker match success; M = number of detected markers; M_{th} = threshold for M.

plane [71, 77], and sagittal motion is the most crucial for planning margins (especially towards the rectum). Therefore, obtaining the highest treatment precision may be most useful for (nearly) lateral beams. For beams 3 and 6, the superior-inferior (SI) intrafraction motion is derived exactly whereas the anterior-posterior (AP) motion is almost identical to the horizontal shift in the MVI (lateral contribution negligible).

Image acquisition and matching in iSGT is automatically synchronized with beam delivery and requires no user actions. The user only becomes involved when the software proposes a set-up correction. After user evaluation of the image registration, the TCSA system (above) may then be used for remote couch translations. The iSGT workflow can optionally generate an accelerator interlock until couch movement is ready. MVI-3 and MVI-6 are automatically processed to obtain the projected centre of mass (COM) of the markers using methods described in [69], followed by an AIMS test (see section 4.2.5 "AIMS" below) to objectively verify whether the marker match was successful. A set-up correction is only proposed by the software if 1) the match was successful according to AIMS ($M = M_{th}$ in Figure 4.2) and 2) the established 2D COM positioning error from the automatic marker match (AM) is larger than the pre-defined action level (e_{th} in Figure 4.2). In all other cases no correction is performed. In case of a successful match with AM > e_{th}, beam delivery is held after the first segment, the match result is automatically displayed on a screen, and the user is asked to evaluate the result (Figure 4.2). The user can approve, adjust or

skip (if the image is hard to judge) the match. If, after user evaluation, the (adjusted) match result is above e_{th}, the correction is executed by remote couch control, and the remaining beam segments and all segments of subsequent non-iSGT beams are delivered. Results from AM and AIMS become available within the time frame required for the linac record and verify system to continue with delivery of the remaining segments after the first MVI segment. If there is no correction necessary, beam delivery automatically continues. Consequently, for fractions that do not require intrafraction corrections, iSGT does not add time to treatment delivery.

4.2.4   AIMS: Algorithm for Automatic Identification of Marker Match Success

A pre-requisite for intrafraction prostate repositioning with iSGT is a marker match algorithm with a high success rate for accurately establishing marker COM displacements from MV-images, i.e. close to true movements. To minimize corrections based on unsuccessful automatic matches, while not having to rely on a time consuming user evaluation of each match, we introduced the AIMS test for automated identification of marker match success. The AIMS test is based on a student t-test performed on the image pixel grey scale values in each marker region. For each detected marker region the test parameter t, which is a measure of the detectability of the marker, is calculated from the means and standard deviations of the grey scale values in an area of pixels in the detected marker region and an area surrounding the marker [93]. For normally distributed image noise, this parameter behaves like the t-statistic in regions of constant mean intensity. The threshold for detecting a marker was set to 5 as proposed in the literature [94] and verified by visual inspection [95]. The AIMS test accepts a match if the number of markers with $t > 5$, M, is larger than or equal to the selected threshold M_{th} (selection discussed below) and rejects it otherwise.

4.2.5   Establishing iSGT parameters M_{th} and e_{th}

As mentioned above, the iSGT procedure was designed using image data from a group of 20 patients who were treated with daily SGT pre-fraction corrections. MV-images had been acquired for these patients but not used for intrafraction corrections. In total 970 MV images from the (nearly) lateral beams 3 and 6 were available for analyses. For each image, the marker COM displacement was established both with the AM and by manual identification of the individual markers, the latter resulting in the ground truth (GT) marker COM displacement.

For the parameter M_{th} in the AIMS test, the values 2, 3 and 4 were considered. For selection of M_{th}, we determined for each candidate value the sensitivity and specificity of AIMS for detecting true errors (|AM - GT| < 2 mm). For the subsequent establishment of e_{th}, the values of 3 mm and 4 mm were considered in detail. For the final choice of e_{th} we determined for both candidate values 1) the sensitivity and specificity for automatic detection of true errors that need to be corrected (GT > e_{th}), 2) the number of fractions with a request for user action (M >= M_{th} and AM > e_{th}, Figure 4.2 and above), and 3) effective residual set-up errors for the iSGT protocol. Items 2) and 3) were derived from computer simulations.

In the iSGT simulations, residue errors after intrafraction prostate positioning corrections were calculated by subtracting AM-established corrections from measured GT-errors as follows: if for MVI-3 M >= M_{th} and AM > e_{th}, then the AM-correction was subtracted from the GT-errors measured at MVI-3 and all later moments. This procedure assumes that the correction was obtained and executed so fast that it would not influence occurrence and measurement of intrafraction deviations at later moments. Similarly if M >= M_{th} and AM > e_{th} for MVI-6, the corresponding AM-correction was subtracted from the (residue) GT-errors at MVI-6 and kVIpost. For each patient fraction, the AP and SI components of the 2D effective residual set-up error vector were calculated as time-weighted averages of mean errors in the intervals Δ1: (kVIpre — MVI-3), Δ2: (MVI-3 — MVI-6) and Δ3: (MVI-6 — kVIpost), respectively, similar as in [90]. For the first interval, the mean set-up error was calculated as the average of the measured error in kVIpre and the GT-error in MVI-3. For the second interval, the mean error depended on whether or not an intrafraction set-up correction was required based on MVI-3 and the criterium M >= M_{th} and AM > e_{th}. Without a correction, the mean set-up error was calculated as the average of the GT-errors in MVI-3 and MVI-6. With a correction, the mean amounted to 0.5*((GT-error in MVI-6) - (AM-correction derived from MVI-3)), assuming immediate and exact implementation of the correction derived from MVI-3. Calculation of the mean error for interval 3 was performed similarly, but now depending on whether or not intrafraction corrections were required based on MVI-3 and MVI-6. From the effective fraction displacements, we computed population mean effective errors, i.e. the mean over all patients of the individual mean effective fraction displacements, μ_{eff}, and the standard deviations Σ_{eff} and σ_{eff}, describing systematic and random set-up errors in the patient population [25, 26, 58].

4.2.6   Clinical evaluation of iSGT

iSGT was evaluated for 100 patients that were treated with parameters M_{th} and e_{th}, selected as described in the previous section, and reported in the Results section. To this purpose, AM displacements for kVIpre, MVI-3, MVI-6, and kVIpost were extracted from the clinical database. Using the stored images, ground truth (GT) marker COM displacements were also obtained by manual marker matching in all images. The clinical performance of iSGT was evaluated by studying the AM accuracy, the performance of the AIMS test, and the magnitude of effective intrafraction errors. For comparison we also calculated effective errors from (estimated) GT errors that would have occurred without iSGT corrections by undoing all corrections that were actually applied clinically. This was possible since all corrections together with couch positions before and after each table shift were stored in the Theraview database. Based on the GT errors that would have occurred without corrections, we also simulated iSGT protocols for e_{th} values that were not used clinically, applying the same simulation approach as explained in the previous section.

4.2.7   Comparison with an offline intrafraction correction strategy

Recently, it was shown that the mean intrafraction motion measured during the first week of treatment correlates with the mean intrafraction motion in subsequent weeks [73, 96], suggesting that an offline strategy similar to the no-action-level (NAL) offline correction protocol [39] for interfraction errors could also be beneficial for intrafraction error correction. Using the established GT-errors that would have occurred in 100 patients without intrafraction corrections (previous section) we simulated such an offline correction strategy. For this we assumed acquisition of MVI-3 and MVI-6 in the first 5 fractions and absence of intrafraction set-up corrections in these fractions. After fraction 5 there was an offline assessment of both the mean set-up error observed in the MVI-3 and the mean error in the MVI-6 in these initial fractions. For the next fractions, a priori couch repositionings by -(mean set-up error in the initial fractions) prior to delivery of beams 3 and 6 were simulated. Residual effective displacements using this offline correction strategy were compared with residual displacements obtained with online corrections based on iSGT.

4.3 Results

4.3.1 Establishing iSGT parameters M_{th} and e_{th}

Table 4.1 shows the performance of the AIMS test for detecting successful and unsuccessful matches as a function of M_{th}. The success rate for automated matching was 90.9% (images with AM success according to GT). From Table 4.1, $M_{th} = 2$ was selected for the clinical iSGT procedure, based on the high sensitivity (93.6%) for correctly identifying match successes with acceptable specificity (58.4%). Only in 3.8% of cases AIMS claimed a successful match while it was not. For $M_{th} = 2$, 85.1% of all images had a correct match according to GT that was also recognized by AIMS. When using $M_{th} = 3$ and $M_{th} = 4$ the latter dropped to 68.5% and 33.3%, respectively. Table 4.2 presents the performance of the automatic match (AM) algorithm

Table 4.1: Performance of the AIMS test for detection of automatic match (AM) successes, defined as | AM-GT | < 2mm (GT= Ground Truth), as a function of the parameter M_{th}. The data were obtained from AM for a total of 970 MV-images.

According to GT:	AM Failure		AM Success		Sensitivity	Specificity
According to AIMS:	AM Success*	AM Failure*	AM Success*	AM Failure*	AIMS	AIMS
$M_{th} = 2$	37 (3.8 %)	52 (5.4%)	825 (85.1 %)	56 (5.8%)	93.60%	58.40%
$M_{th} = 3$	18 (1.9 %)	71 (7.3%)	664 (68.5 %)	217 (22.4 %)	75.40%	79.80%
$M_{th} = 4$	3 (0.3 %)	86 (8.9%)	323 (33.3 %)	558 (57.5 %)	36.70%	96.60%

Abbreviations: GT = Ground Truth, AM = Automatic Match, AIMS = Automatic Identification of Match Success
* Indicated are numbers of images. The values in brackets are percentages of the total number of images.

Table 4.2: Performance of the automatic match (AM) algorithm in detecting true set-up errors larger than the threshold error, e_{th}, for $e_{th} = 3$ mm and 4 mm. The data were obtained from AM for a total of 970 MV images.

	GT > e_{th}		GT < e_{th}		Sensitivity	Specificity
	AM > e_{th}*	AM < e_{th}*	AM > e_{th}*	AM < e_{th}*	AM	AM
$e_{th} = 4$ mm	173 (17.8 %)	27 (2.8 %)	36 (3.7 %)	734 (75.7 %)	86.50%	95.30%
$e_{th} = 3$ mm	300 (30.9 %)	33 (3.4 %)	67 (6.9 %)	570 (58.8%)	90.00%	89.50%

Abbreviations: AM = Automatic Match, GT = Ground Truth
* Indicated are numbers of images. The values in brackets are percentages of the total number of images

in detecting true set-up errors larger than the threshold error $e_{th} = 3$ mm or $e_{th} = 4$ mm. Table 4.3 shows effective set-up errors for these thresholds, resulting from iSGT simulations. When using an action level of 3 mm, intrafraction corrections were proposed in 32.5% of the fractions. When the action level was increased to 4 mm, this percentage reduced to 18.0%. Considering the moderate differences between 3

Table 4.3: Simulated population effective set-up errors for the initial group of 20 patients in superior-inferior (SI) and anterior-posterior(AP) directions

	Effective set-up errors (mm)			
	$\mu \pm \Sigma$ (SI)	$\mu \pm \Sigma$ (AP)	σ (SI)	σ (AP)
After SGT correction, prior to first beam	0.0±0.5	0.3±0.5	0.7	0.6
No intrafraction set-up corrections	-0.1±1.2	0.6±1.1	1.0	1.1
iSGT with action level of 4 mm	-0.3±0.7	0.3±0.6	0.8	1.0
iSGT with action level of 3 mm	-0.4±0.7	0.1±0.5	0.8	0.9

Abbreviations: AP = anterior-posterior, SI = superior-inferior, iSGT = intrafraction StereoGraphic Targeting, SGT = StereoGraphic Targeting, Σ = systematic error, σ = random error

mm and 4 mm in Tables 4.2 and 4.3 and the (at that time considered rather large) difference in expected workload as resulting from proposed corrections, $e_{th} = 4$ mm was selected for the clinical iSGT procedure.

4.3.2 Performance of iSGT and comparison with offline strategy

We obtained a total of 5788 MVI and 5618 kVI from 100 patients treated with iSGT corrections with $M_{th} = 2$ and $e_{th} = 4$ mm. For the MVI the success rate of automatic marker match (images with AM success according to GT) was 90%, very close to what was found for the images of the 10 patients used to establish iSGT parameters (above). For the clinical iSGT procedure with $M_{th} = 2$, only in 6.3% of cases AIMS claimed a successful match while it was not. In 87.8% of all images, the match outcome according to GT agreed with that of AIMS. The sensitivity was 96.9% for correctly identifying match successes and the specificity was 48.0%, lower than predicted. The first data

Table 4.4: Performance of the automatic match (AM) algorithm in detecting true set-up errors larger than the threshold error, e_{th}. The data were obtained from a total of 5788 MV-images. Clinically $e_{th} = 4$ mm was used. Computer simulations were used to generate data for $e_{th} = 3$ mm and $e_{th} = 2$ mm.

	GT > e_{th}[1]		GT < e_{th}[1]		Sensitivity	Specificity
	AM > e_{th}	AM < e_{th}	AM > e_{th}	AM < e_{th}	AM	AM
$e_{th}= 4$ mm (clinical)	622 (10.8%)	185 (3.2%)	286 (4.9%)	4695(81.1%)	77%	94%
$e_{th}= 3$ mm (simulation)[2]	1566 (27.1%)	234 (4.04%)	411 (7.1%)	3577 (61.8%)	87%	90%
$e_{th}= 2$ mm (simulation)[2]	3180(54.9%)	244(4.2%)	419(7.2%)	1945(33.6%)	93%	82%

[1] Indicated are numbers of images. The values in brackets are percentages of the total number of images
[2] From simulations using clinical data

row in Table 4.4 quantifies the clinical performance of the AM. Comparison with the first data row in Table 4.2 reveals that the actual sensitivity of AM for detecting errors larger than $e_{th} = 4$ mm was almost 10% lower than predicted for the initial group of 10 patients. The second and third data rows in Table 4.4 show AM performances for $e_{th} = 3$ mm and $e_{th} = 4$ mm, respectively, as resulting from the simulations. The impact

Figure 4.3: Cumulative distributions of residual effective fraction set-up errors; The errors are given as vector lengths of 2D effective fraction error in the sagittal plane and comprise both systematic and random components.

of the clinical iSGT protocol on effective set-up errors, compared to no intrafraction corrections, can be derived from data rows 2 and 3 in Table 4.5 and by comparing corresponding curves in Figures 4.4 and 4.3. Clearly, iSGT with $e_{th} = 4$ mm had a positive but modest impact on set-up accuracy. Reductions in Σ and σ were 0.2 - 0.3 mm and 0.1 - 0.2 mm, respectively. With the clinical iSGT corrections, the percentage of effective systematic+random errors exceeding 4 mm was reduced from 10% to 3.9% (Figure 4.3). In Figure 4.4, iSGT could reduce effective systematic errors >2 mm and >3 mm from 42% to 25% and from 7% to 2% respectively. Table 4.5 and Figures 4.3 and 4.4 clearly show that significant reductions in effective set-up errors can be obtained using iSGT with $e_{th} = 3$ mm, and especially with $e_{th} = 2$ mm. With the latter, both the effective random and systematic errors can be kept close to the errors measured with the kVIpre just after SGT correction and prior to delivery of the first beam. Table 4.6 shows numbers of fractions for which the outcome of AM and AIMS result in a proposed iSGT correction as a function of e_{th}. Table 4.5 and Figures 4.3 and 4.4 show that the offline NAL procedure for intrafraction corrections performs a little bit better than iSGT with a threshold of 4 mm. Considering the 5 strategies
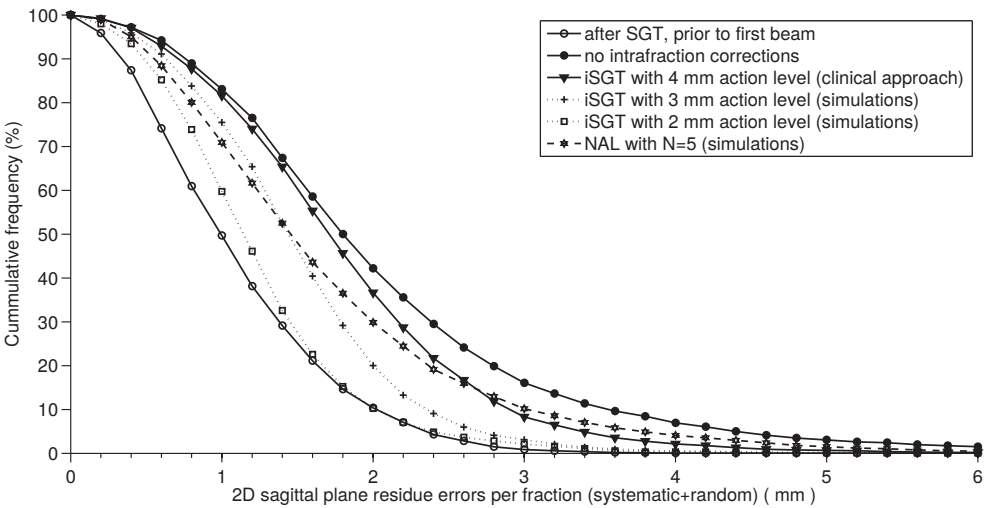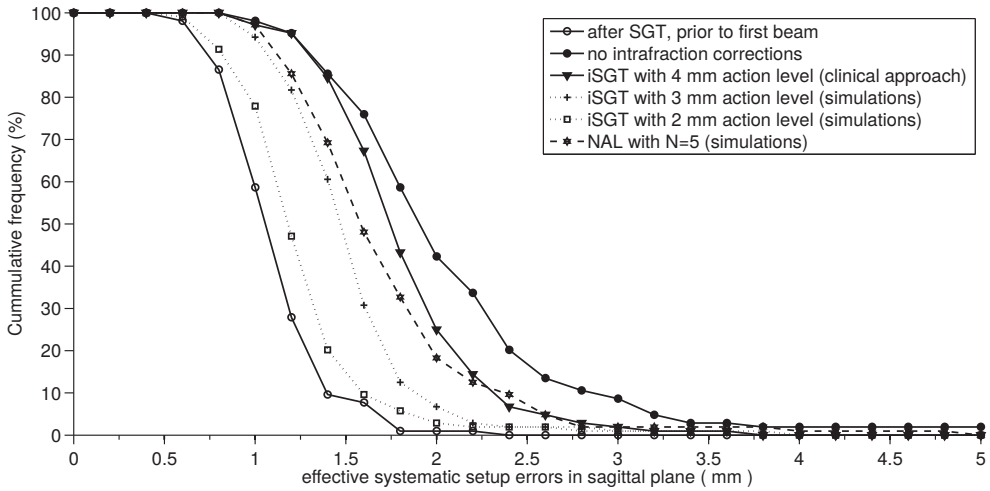
Figure 4.4: Cumulative distributions of residual effective systematic set-up errors per patient; The errors are given as vector lengths of 2D effective fraction error in the sagittal plane and comprise only the systematic component.

Table 4.5: Evaluation of iSGT using images from the 100 clinical iSGT patients; the table shows measured displacements just after initial set-up and as well as displacements without and with iSGT corrections for the clinical action level of 4 mm. Simulated displacements for action levels of 3 mm and 2 mm as well as for the no-action level (NAL)-based offline protocol to correct intrafraction motion are also shown.

	Effective set-up errors (mm)			
	$\mu \pm \Sigma$ (SI)	$\mu \pm \Sigma$ (AP)	σ (SI)	σ (AP)
After SGT correction, prior to first beam	0.3±0.5	0.0±0.5	0.8	0.7
No intrafraction set-up corrections	0.6±1.0	0.8±1.1	1.1	1.2
iSGT e_{th} = 4 mm (clinical protocol)	0.6±0.8	0.6±0.8	1.0	1.0
NAL, with 5 initial measurements[1]	0.3±0.6	0.6±0.8	1.1	1.2
iSGT with e_{th} = 3 mm[1]	0.5±0.7	0.5±0.7	0.9	0.9
iSGT with e_{th} = 2 mm[1]	0.3±0.6	0.5±0.6	0.7	0.7

Abbreviations: μ = population mean error, Σ = systematic error, σ = random error, NAL = No Action Level, other abbreviations as in previous tables.
[1] From simulations using clinical data.

studied for dealing with intrafraction prostate motion (no intrafraction corrections, iSGT with e_{th} = 2, 3, 4, and NAL), iSGT with a 2 mm threshold result in the lowest effective errors.

4.4 Discussion

In a recent study [90], we observed in a group of 108 patients significant random and systematic intrafraction motion, i.e. intrafraction motion that reproduced from day-

Table 4.6: Numbers and percentages of fractions with 0, 1 and 2 proposed corrections (requiring user action) as a function of error threshold. Corrections are proposed after positive outcome of AIMS and AM (Figure 4.2). The total number of fractions was 2894 and $M_{th} = 2$

Number of corrections in fraction	0		1		2	
	Number	%	Number	%	Number	%
e_{th} = 4 mm(clinical protocol)	2225	76.9	629	21.7	40	1.4
e_{th} = 3 mm[1]	1432	49.5	1124	38.8	338	11.7
e_{th} = 2 mm[1]	507	17.5	1350	46.6	1037	35.8

[1] From simulations using clinical data of 100 patients treated clinically with iSGT.

to-day. Depending on the patient, the high initial prostate set-up accuracy achieved with SGT could seriously deteriorate during the treatment fractions. In this paper we have developed, implemented and clinically evaluated for 100 patients the intrafraction StereoGraphic Target (iSGT) system for intrafraction prostate set-up corrections, based on planar MV-imaging of implanted fiducials. The system is software controlled and integrated in the linac workflow. User interaction is only required if the software proposes an intrafraction set-up correction based on an acquired MV-image. The proposed correction can then be approved, adjusted, or skipped, based on the presented result of the underlying MV image registration. Set-up corrections are executed using a commercial system for remote couch control. Patients in this study were treated with an error threshold (e_{th}) of corrections of 4 mm. This resulted in a clear but modest improvement compared to no intrafraction corrections. Computer simulations indicate that with e_{th} = 2 mm effective random and systematic fraction errors can be kept close to the errors measured just after initial SGT set-up correction, prior to delivery of the first beam. Obviously, with a lower threshold, more corrections are proposed. As explained in the Material and Methods section, iSGT (only) results in increased fraction duration in case of these correction proposals. For the 100 patients in this study, user interaction after a correction proposal and correction execution took generally < 30 sec, resulting in a total maximum fraction time increase due to iSGT of approximately 1 minute (maximum of two intrafraction set-up corrections).

Because intrafraction motion is partly systematic [90], patient set-up accuracy might benefit from intrafraction set-up corrections based on an offline correction protocol such as the No Action Level (NAL) protocol [39], widely used to correct systematic interfraction set-up motion. In this study we performed computer simulations to investigate the impact of such a protocol based on intrafraction set-up measurements in the first 5 fractions (without corrections). After the fifth fraction, patients were then repositioned, compensating for mean set-up errors measured during the

first 5 fractions (no further imaging needed). The simulations demonstrated that reductions of effective set-up errors with this offline protocol were similar to iSGT with a threshold of 4 mm, while iSGT with a threshold of 2 mm performed substantially better.

This study and the iSGT method for intrafraction prostate set-up correction have some limitations. Like the other (published) methods, iSGT depends on 1) imaging of fiducials implanted in the prostate and 2) translational corrections. Clearly, such an approach is limited in case of prostate deformation and/or rotation, and does often not always allow accurate correction of movements of the seminal vesicles [86]. In a recent study [87] we proposed a method to select margins that account for the residual errors. Another limitation of iSGT is that corrections are based on measurements at specific time points in each fraction, not on continuous monitoring. Effective errors were computed assuming that the mean position in a time interval could be calculated as the average of the measured positions in the images that defined the beginning and the end of the interval, neglecting asymmetric set-up variations around this calculated mean within the interval. For sure this will result in some inaccuracies in calculated effective errors. However, we believe that considering all patients and all fractions, this simplified approach for assessment of the mean set-up error in an interval will on average be accurate. In the current iSGT procedure, intrafraction set-up verification and correction was only performed prior to delivery of the nearly lateral beams. These beams were selected to maximally protect the rectum. Due to this choice, corrections were however limited to the sagittal plane, which on the other hand is also the plane with the most prostate motion [77, 90]. More time points for intrafraction correction could be used, but with the current selection of two time points and an error threshold of 2 mm, effective fraction set-up errors were already close to the errors measured just prior to start of treatment.

4.5   Conclusion

We have implemented and evaluated for 100 patients a software-controlled, highly automated procedure for intrafraction prostate set-up corrections using MV imaging of implanted markers. With generally less than 1 minute prolongation of treatment time, effective fraction set-up errors can become close to the errors measured at the start of treatment.

4.6 Acknowledgements

Deformation of Prostate and Seminal Vesicles Relative to Intraprostatic Fiducial Markers

Gerard J. van der Wielen, Theodore F. Mutanga, Luca Incrocci, Wim J. Kirkels, Eliana M. Vásquez Osorio, Mischa S. Hoogeman, Ben J.M. Heijmen and Hans C.J. de Boer

Abstract

Purpose

To quantify the residual geometric uncertainties after online corrections with intraprostatic fiducial markers, this study analyzed the deformation of the prostate and, in particular, the seminal vesicles relative to such markers.

Patients and Methods

A planning computed tomography (CT) scan and three repeat CT scans were obtained for 21 prostate cancer patients who had had three to four cylindrical gold markers placed. The prostate and whole seminal vesicles (clinical target volume [CTV]) were delineated on each scan at a slice thickness of 1.5 mm. Rigid body transformations (translation and rotation) mapping the markers onto the planning scan positions were obtained. The translation only (T_{only}) or both translation and rotation were applied to the delineated CTVs. Next, the residue CTV surface displacements were determined using nonrigid registration of the delineated contours. For translation and rotation of the CTV, the residues represented deformation; for T_{only}, the residues stemmed from deformation and rotation. T_{only} represented the residues for most currently applied online protocols. The patient and population statistics of the CTV surface displacements were calculated. The intraobserver delineation variation was similarly quantified using repeat delineations for all patients and corrected for.

Results

The largest CTV deformations were observed at the anterior and posterior side of the seminal vesicles (population average standard deviation = 3 mm). Prostate deformation was small (standard deviation = 1 mm). The increase in these deviations when neglecting rotation (T_{only}) was small.

Conclusion

Although prostate deformation with respect to implanted fiducial markers was small , the corresponding deformation of the seminal vesicles was considerable. Adding marker-based rotational corrections to online translation corrections provided a limited reduction in the estimated planning margins.

5.1   Introduction

Prostate cancer is the most common type of cancer for men in Western countries [97] and is often treated with external beam radiotherapy. However, external beam radiotherapy leads to Grade 2 late gastrointestinal toxicity in 1.6-32% of patients, Grade 2 late urinary toxicity in 15-41%, and erectile dysfunction in 36-43% [11, 17, 98]. Therefore, a large patient population would benefit from techniques able to reduce these common sequelae. Apart from imperfect target delineation, several uncertainties exist regarding movement of the clinical target volume (CTV), CTV deformation, and variations in beam geometry characteristics. A margin is added to the CTV to account for these uncertainties. The planning target volume (PTV) is the CTV plus this margin [23, 24]. A reduction of the CTV-PTV margin can lead to lower toxicity [99]. The CTV-PTV margin can be reduced to less than the commonly used 1 cm with image-guided radiotherapy or adaptive radiotherapy [39, 51, 69]. In our clinic, a fully automated method for fast and accurate daily online prostate positioning during external beam radiotherapy was developed for the Synergy system (Elekta, Crawley UK) and clinically implemented [69]. This method, Stereographic Targeting (SGT), is based on intraprostatic fiducial markers that are imaged in a crossfire of megavoltage and kilovoltage beams, followed by fully automated image analysis and remotely controlled couch shifts. Despite a high positioning accuracy for the center of mass (COM) with SGT, the margin reduction must be based on knowledge of the residue displacements over the entire surface of the CTV. In this study, the residue displacements were obtained from repeat computed tomography (CT) scans delineated at a high resolution after rigid registration of the fiducial markers using nonrigid registration. Quantification of these residues allows for the assessment of margins for marker-based set-up corrections. For instance, the marker registration method allowed us to quantify the residue displacements when only translation corrections were applied. The latter displacements depend not only on the CTV shape, but also on the behavior of the seminal vesicle deformation in the presence of prostate rotations. Knowledge of these displacements is clinically relevant because online corrections are often limited to translation corrections [49, 69]. To our knowledge, this is the first study to quantify these rotation deviations in detail. The use of fiducial markers as a reference frame in this study had another major advantage: the markers are clearly distinguishable on the CT scans and their relative positions are very stable [39, 57]. In contrast to methods that use delineated CTVs for initial rigid body registration [100], the rigid body match with markers hardly depends on the sought deformations or on the delineation errors. Therefore, fiducial markers present a suitable frame of reference for quantifying the deformations.

5.2   Patients and Methods

5.2.1   Patients

Patients scheduled for external beam radiotherapy for prostate cancer were asked to participate in this study (i.e., undergo multiple CT scan sessions). Between August 2006 and March 2007, 21 patients agreed to participate and gave written informed consent. The clinical T category was as follows: Stage T1, 9 patients; T2, 5 patients; and T3, 7 patients. Patients with T3 tumors were treated with adjuvant hormonal therapy. Although not all patients were treated to the seminal vesicles, the whole seminal vesicles were analyzed for each patient in this study. In each patient, three to four fiducial markers (gold cylinders, 1 mm x 5 mm) were implanted transperineally using 18-gauge needles under transrectal ultrasound guidance and local anesthetic. The Medical Ethical Committee of our hospital approved the study, which was conducted in accordance with the Declaration of Helsinki.

5.2.2   Data acquisition

For the planning CT scan, the patients followed our routine clinical protocol. The planning CT scan (Somatom Sensation Open with HiRes-option, Siemens Medical Solutions, Erlangen, Germany) was scheduled = 1 week after marker implantation to allow any possible edema to resolve. Patients used a laxative and were instructed to empty their rectum before the planning CT scan. Furthermore, they were instructed to empty their bladder and drink 0.5 litre of fluid 1 hour before the planning CT scan. In treatment weeks 2, 4, and 6, a repeat CT scan was acquired directly before or after a treatment fraction. Patients followed the same instructions, except for the use of a laxative. All four scans were performed with the patient set up as during treatment (supine position, head rest, and knee and feet support). The CT scans were reconstructed with a slice thickness of 1.5 mm and a transversal pixel size of 0.7 x 0.7 mm^2. The prostate and the whole seminal vesicles (CTV) were delineated on each CT scan by a single observer (GJW) at the same slice resolution (1.5 mm). The distance from the inferior-most fiducial marker to the apex of the prostate from the planning CT scan was used as a guide to identify the apex on the repeat CT scans.

5.2.3   Statistical analysis

The analysis was performed using in-house developed software (C++ using the ITK and VTK toolkits and Matlab). Surface meshes were created from the Digital Imaging

and Communications in Medicine (DICOM) exported contours. Hereafter, the CTV surface is referred to as the CTV and any quantity obtained from the planning and repeat CT scan is termed *reference* and *repeat*, respectively. The rigid body transformation between the repeat and reference scans was obtained with a dedicated tool. A single marker was defined by the two longitudinal end positions of each marker. In each repeat scan, the markers were identified, and a rigid body transformation solving for translation and rotation about the COM of all markers, was performed. This transformation was then applied to the repeat CTV. Next, the residual deformation between the repeat and reference CTV was estimated by nonrigid registration; see Chui; Rangarajan [101], Osorio et al. [102], Vásquez Osorio et al. [103] for details. The nonrigid registration finds a transformation function between two point sets derived from the CTV meshes. Then, the transformation function generated vectors that connect the points on the repeat CTV to the reference CTV. These vectors are referred to as *residue displacements*. For each patient, the residue displacements were used to create an average CTV shape, and the standard deviations (SDs) of the vector field projections on the local surface normals were derived. We restricted ourselves to reporting motion along these normals because such motion is the most relevant to determine CTV coverage and required margins. To calculate and visualize the population statistics, the same nonrigid transformation software was used to create the population average CTV and to map patient-specific local SDs onto the population average CTV. The procedure, described in detail in the Appendix 5.7, is illustrated in Figure 5.1.

5.2.4 Correction for delineation variation

The SDs described in the previous section might have been overestimated owing to delineation inaccuracies. Because all scans were delineated by a single observer (GJW) and because only variations from scan to scan determined the SDs, the overestimate resulted from intraobserver variation. Hence, two repeat scans in each patient were recontoured by the same observer (GJW). The same nonrigid matching was applied to register *delineation 1* onto *delineation 2*. The length of the subsequent deformation vectors was taken in quadrature and averaged for both redelineated scans to estimate the local SDs due to the delineations. Because these SDs comprise the inaccuracies in both delineations, they were divided by $\sqrt{2}$ to obtain the single delineation SD. The latter SDs were subtracted in quadrature from the deformation SDs to obtain the actual CTV shape variations.
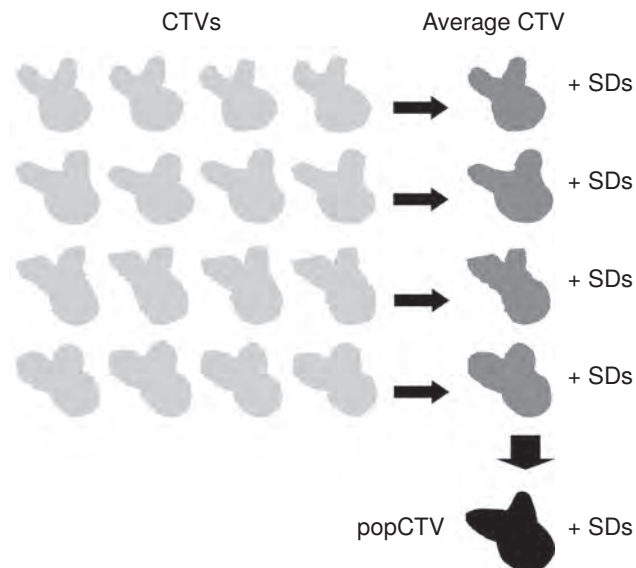
Figure 5.1: Light gray shapes represent rigidly registered clinical target volumes (CTVs). Subsequent nonrigid registration yielded average CTV for each patient (dark gray) and corresponding interfraction standard deviations of deformations. Patient-specific standard deviations are then projected on population average CTV (black).

5.2.5 Full correction vs. translation only correction

Large systematic and random rotations of the prostate about the left-right axis have been observed (SD, 4°-5°) when only translational corrections are applied [39, 57, 59]. To study the residue displacements due to rotations and deformations in the case of translational corrections determined from the markers' COM, we repeated the nonrigid registration analysis after only the translation part of the rigid body transformation (T_{only}) was applied to the CTVs. The effect of the rotations in a T_{only} correction protocol can increase if the COM of the markers is not coincident with the prostate COM [39]. Because we used marker-based COM translations for registration, this effect was implicitly taken into account in our study.

5.2.6 Separation into systematic and random residue displacements

The SDs described in the previous section reflect the interfraction variation of residue displacements at the CTV surface. Interfraction variations are commonly referred to as random errors and are usually denoted by σ [104]. If the displacements have no systematic time dependency during the treatment course (i.e., it is unimportant when

the planning and repeat CT scans are obtained), the SD of systematic errors, Σ, equals the SD of the random errors: $\Sigma = \sigma$ [51, 104]. The number of scans and patients in this study was too small to test this assumption in detail. Nevertheless, if Σ is locally significantly smaller or larger than σ, this should be taken into account in the margin calculations. We therefore investigated whether we could find large deviations from $\Sigma = \sigma$. The calculation of the Σ-maps is described in the Appendix 5.7.

5.3   Results

5.3.1   Marker registration results and accuracy

The rigid body registration on fiducial markers determined the frame of reference in this study. We, therefore, determined the accuracy of this registration method. After registration, the match gives the remaining displacements for each marker. The SD of these displacements for all registrations was 0.4 mm in each direction. This SD included all deviations in the registration process, such as the accuracy of defining markers on the CT scans and the relative displacements of the markers. Consistent with the published data, these effects are small [39, 57], and the assumption that the markers provide a proper frame of reference was thus confirmed. The SD for the COM position was 0.2 mm, equal to the accuracy of the translation part of the rigid body transformations we applied. The SDs of the systematic (Σ) and random (σ) prostate rotation angles were approximately 4° about the left-right axis and <2° about the other axes. The average measurement inaccuracy of these rotations, calculated from the marker separations and the above-mentioned residue errors (0.4 mm SD) for each marker was <1° (SD).

5.3.2   Residue interfraction displacements due to deformations and rotations

Figure 5.2 and Table 5.1 and Table 5.2 summarize the residue displacements along the local surface normals, as obtained for the translation plus rotation (T+R) (residues due to deformation) and T_{only} (residues due to both deformation and rotation). Table 5.1 and Table 5.2 list the average residue displacements of the different regions. Figure 5.2a shows the maps of the population averaged SDs (σ, see Appendix 5.7) of the residue displacements, uncorrected for delineation variation, along the CTV surface normals, projected onto the population average CTV shape in the case of T+R.
   Table 5.1 and Table 5.2 and Figure 5.2b summarize the intraobserver delineation
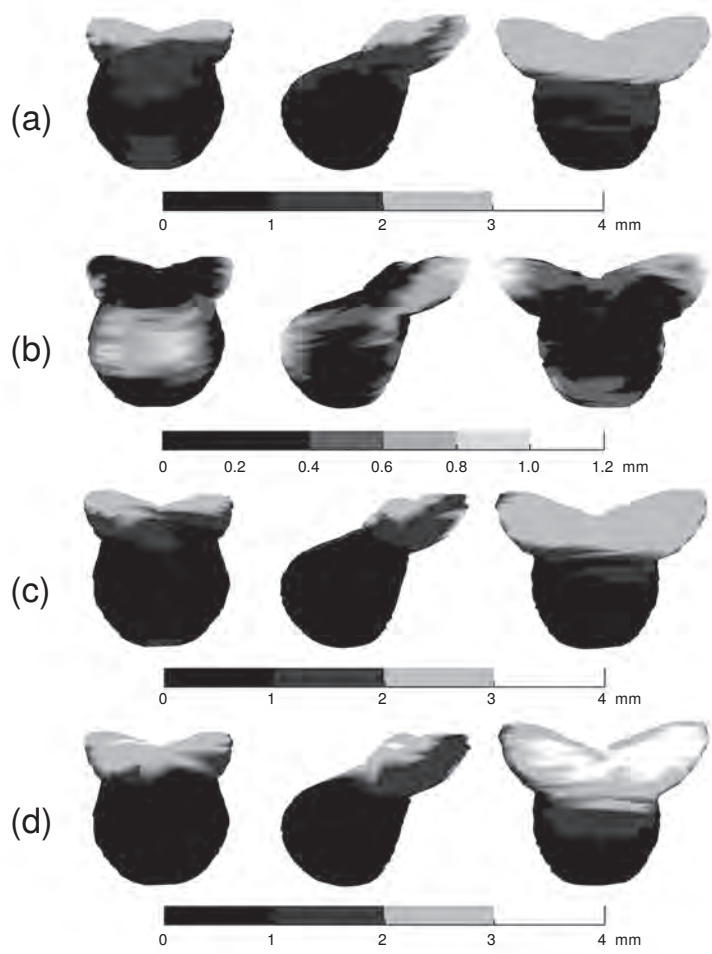
Figure 5.2: (a) Standard deviation of interfraction variation (s) after marker-based rigid body registration (translation plus rotation [T+R]), as projected onto the population-averaged clinical target volume, uncorrected for intraobserver delineation variation. (b) Corresponding standard deviations of intraobserver delineation variation. (c) Same as in Figure 5.2a, but now corrected for delineation variation in Figure 5.2b (i.e., actual variation). (d) Same as Figure 5.2c, but now for only rigid translation applied (T_{only}).

variation. This small variation was comparable for the prostate and seminal vesicles. Correcting the full variation for intraobserver variation yielded the actual variation, as listed in Table 5.1 and Table 5.2 and displayed in Figure 5.2c,d. The effect of the intraobserver correction was small. The actual variation for T+R reflects the interfraction motion of the CTV surface relative to the fiducial markers. Apparently, the prostate surface moves along with the fiducial markers as an almost fully rigid body

Table 5.1: Standard deviations (σ) for deviations along local surface normals in various regions of interest of prostate

	Left	Right	Cranial	Caudal	Anterior	Posterior
Full variation, T+R	0.5	0.6	1.2	1.00	1.00	1.00
Intraobserver variation, T+R	0.4	0.5	0.3	0.4	0.7	0.5
Actual variation, T+R	0.3	0.3	1.1	0.9	0.7	0.8
Actual variation, T_{only}	0.3	0.3	1.4	0.9	0.7	1.3

Abbreviations: T+R = correction for rotation and translation; T_{only} = correction for translation only.

Table 5.2: Standard deviations (σ) for deviations along local surface normals in various regions of interest of seminal vesicles

	Lateral SV		Tip SV		Anterior SV		Posterior SV	
	left	right	left	right	left	right	left	right
Full variation, T+R	2.0	1.8	2.2	2.6	2.4	2.5	2.6	2.8
Intraobserver variation, T+R	0.8	0.9	0.7	0.7	0.3	0.3	0.4	0.6
Actual variation, T+R	1.7	1.6	2.1	2.5	2.3	2.5	2.5	2.7
Actual variation, T_{only}	1.7	1.7	2.2	2.7	2.8	2.9	3.1	3.4

Abbreviations: SV = seminal vesicle; other abbreviations as in Table 5.1

(SDs of = 1 mm). In contrast, the seminal vesicles exhibited considerable relative motion. For the seminal vesicles, the SDs ranged = 3 mm and was dependent on the position.

5.3.3 Influence of rotations on residue displacements

When only the translation correction for the markers' COM was applied, we obtained the SD maps (Figure 5.2d and last rows of Table 5.1 and Table 5.2). For the prostate, the residue displacements for T_{only} became slightly larger cranially and posteriorly with respect to T+R. These local increases were as expected, because the average prostate shape (Figure 5.2) was most flattened in these regions (for a perfectly spherical prostate with the marker COM at its center, the increase would be zero). Similarly, the residue displacements for the seminal vesicles increased for T_{only}. Hence, the vesicles co-rotated with the prostate to a certain extent. Nevertheless, owing to the large deformation of the vesicles relative to the markers, the relative influence of the rotations on residue displacements was small (everywhere, < 0.7 mm).

5.3.4 Systematic and random residue displacements

The residue errors in Figure 5.2 were random interfraction displacements. Figure 5.3 shows the absolute values of the difference of the systematic (Σ) and random (σ)

residue displacements as mapped onto the average CTV shape. The smallness of this difference (everywhere, < 0.7 mm, and usually, < 0.5 mm) was consistent with the assumption that $\Sigma = \sigma$. Hence, the CTV deformations with respect to the markers can be considered to be equal in the planning and repeat CT scans.
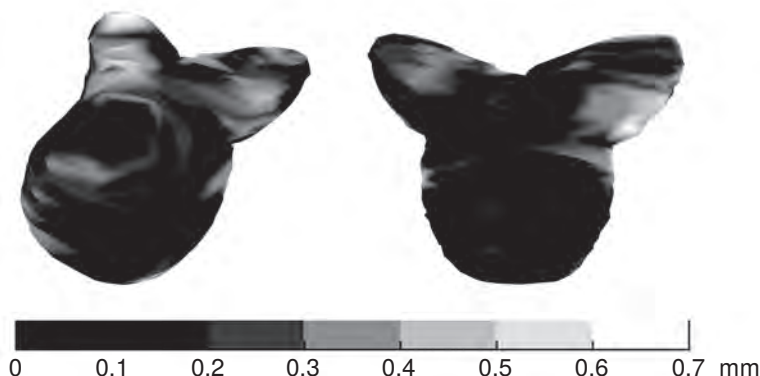
Figure 5.3: Absolute values of difference of systematic (Σ) and random (σ) residue displacements, projected onto the population-averaged clinical target volume.

5.4 Discussion

The most detailed previous study on prostate and seminal vesicle deformation was by Deurloo et al. [100], who quantified the shape variations of the prostate and seminal vesicles using repeat CT scans. Apart from the use of thicker CT slices than in the present study (3 mm vs. 1.5 mm), an important distinguishing feature was their initial rigid body transformation. This transformation was obtained from a chamfer match of the entire delineated gross tumor volume (prostate and vesicles). Therefore, the deformation might have influenced their rigid body transformations. For Deurloo et al. [100], this problem was not as relevant, because their study considered residue displacements in correction strategies based on prostate delineations from multiple CT scans. However, when using prostate markers for the rigid body registration, the actual shape variation near the seminal vesicles is expected to be greater than that derived in their approach. Deurloo et al. [100] obtained an average SD of 1.5 mm near the seminal vesicle tips. In contrast, we obtained 2.3 mm, and even larger SDs posteriorly (2.6 mm; Table 2). Consequently, for marker-based correction strategies, the larger numbers for the seminal vesicles presented in this report might

apply. The small prostate deformation reported by Deurloo et al. [100] is very similar to the findings of the present study. Meijer et al. [105] presented a repeat CT scan study with intraprostatic fiducial markers. The prostate and the first 2 cm of the seminal vesicles were included in the CTV. The results were reported in terms of the local planning margins for various correction strategies, instead of local deformations. Consequently, these derived planning margins pertain to their specific dose distributions. Their result that perfect online set-up corrections based on markers allowed for margins of 3 mm for the prostate and 7 mm for the first 2 cm of the seminal vesicles is consistent with the margins we derived in the next paragraph.

The planning margin calculation in the presence of deformations is a nontrivial subject. Margin recipes such as the CTV-PTV margin = $2\Sigma + 0.7\sigma$ [26] were derived for rigid body translation motions [25, 26], in which the values of Σ and σ are constant along the surface of the CTV, together with assumptions on the dose distribution. Such recipes are already approximate and somewhat arbitrary for ideal cases [25, 26]. To discuss the full effect of nonrigid motion on planning margin estimates was beyond the scope of this study. For delineation errors, which can be considered to be small deformations, because they can be different at each point on the CTV surface, it has been suggested that a margin recipe such as given above is still approximately valid [25]. Therefore, purely for illustrative purposes, we estimated the margins by applying local values of Σ and σ along the surface normals in a margin recipe. The thus-obtained margins in the case of online correction by SGT are shown in Figure 5.4, for translation corrections (T_{only}) and translation plus rotation corrections (T+R). The corresponding residue displacements, as reported in this study, were added in quadrature to the Σ and σ values of COM displacements remaining after SGT correction [106]. The latter contribution consisted of the small residue errors ($\Sigma = 0.5$ mm, $\sigma = 0.8$ mm in each direction) directly after online correction (8), as well as those caused by intrafraction motion. Kotte et al. [77] performed a marker-based study on prostate intrafraction motion in 427 patients. We took the values from their Table 5.2 ($\Sigma = 0.6$ mm, $\sigma = 0.9$ mm in each direction), consistent with the results we obtained in a smaller group. Furthermore, the presently unavoidable random intraobserver delineation errors (Figure 5.2b) satisfied the criteria for inclusion in a CTV-PTV margin expansion and were included in the margin calculation. The decrease in margins when adding online (marker-based) rotation corrections was modest (Figure 5.4b). For the prostate, this decrease was negligible, but for the vesicles it was approximately 1 mm. This small reduction was expected because the vesicles only partly co-rotated with the prostate. Despite the small residue errors near the prostate, the margins for the seminal vesicles could not be reduced much < 1 cm. However, Figure 5.4 shows that when anisotropic margins would be used an addi-
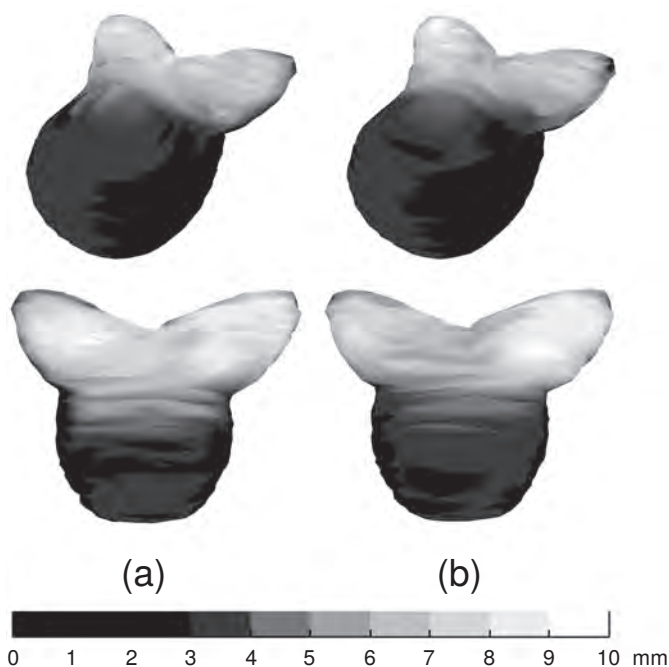
Figure 5.4: Local clinical target volume to planning target volume margins derived for online correction strategies, projected onto the population-averaged clinical target volume. (a) Only translation corrections (T_{only}). (b) Translation and prostate rotation corrections (T+R)

tional reduction could be made at the lateral part of the seminal vesicles. The seminal vesicles seemed to deform mostly in the anterior-posterior and cranial caudal direction because of variation in rectal and bladder filling. In this study, a mild laxative was only used before the planning CT scan. The use of a mild laxative to promote an empty rectum during treatment (if no diarrhea is present), might enable an additional reduction of the treatment margin, especially for the seminal vesicles. Nonetheless, these results stemmed from the mainly geometric considerations underlying the margin recipes. In particular for the seminal vesicles, it is unclear whether such relatively large margins need to be applied. Even when a risk of seminal vesicle invasion is present, it might not be necessary to guarantee full-dose coverage for the entire seminal vesicle volume. However, only one study has provided quantitative information on seminal vesicle involvement. Kestin et al. [20] analyzed 334 Stage T1 and T2 prostatectomy specimens. Of the 51 patients with seminal vesicle invasion, only 10% had tumor beyond the proximal 2.0 cm. They advised treating the seminal vesicles only in patients with sufficient expected risk and to include only the first 2.0-2.5 cm of the seminal vesicles in the CTV. However, no evidence has been provided

to support the inclusion of only a part of the seminal vesicles in the CTV for Stage T3-T4 tumors. Geometric considerations alone are too limited to predict the clinical effect of margin and volume reductions at the seminal vesicles. Factors such as tumor clonogen density and characteristics, dose fractionation, and the conformality of the dose distribution should be taken into account [107]. We, therefore, are conducting a study, using the deformation data presented in the present study, to validate the planning margins for the prostate and, in particular, the seminal vesicles in a full (radiobiologic) dose reconstruction.

5.5 Conclusion

The deformation of the prostate relative to the intraprostatic fiducial markers was small (SD < 1 mm). In contrast, the deformation of the seminal vesicles relative to these markers was significant (SD = 3 mm). Consequently, the effect on treatment planning margins of the corrections for prostate rotation was small. Future work, including actual dose distribution analyses, is required to conclude whether the CTV-PTV margin of the seminal vesicles can be reduced significantly less than the commonly used 1 cm for online set-up corrections based on fiducial markers.

5.6 Acknowledgments

We thank Wilco Schillemans, Hans Joosten, Marjolein van Os, and Ruud Kuipers for their contribution to this study.

5.7 Appendix

5.7.1 Derivation of local systematic and random residue displacements after rigid body registration

In each patient i ($1 \leqslant i \leqslant N_P$), prostate and seminal vesicles are delineated in each CT scan j ($1 \leqslant j \leqslant N_S$; $j = 1$ is a reference scan). The so obtained CTV surface meshes $S_{i,j}$ can be represented as a collection of $N_{i,j}$ 3D vectors $\vec{r}_{i,j}(k)$, each vector representing a surface point:

$$S_{i,j} = \{\vec{r}_{i,j}(1), \ldots, \vec{r}_{i,j}(N_{i,j})\}; \vec{r}_{i,j}(.) \in \mathfrak{R}^3. \tag{5.1}$$

Each repeat scan ($j > 1$) is rigidly registered with scan 1 using the fiducial markers. As mentioned in the manuscript, two cases were studied:

1. Apply only the translation

$$S_{i,j}^t = S_{i,j} + T$$

2. Apply both translation and rotation

$$S_{i,j}^t = RS_{i,j} + T$$

The analysis will continue with the rigidly transformed surfaces, $S_{i,j}^t$, which are now in the marker-based coordinate frame of the reference surface. We will henceforth drop the superscript "t" for readability.

Calculating patient average displacement vectors and average surface

For patient i and scan j, non-rigid transformations $f_{i,j} (j > 1)$ mapping the points of reference surface $S_{i,1}$ to points on repeat surface $S_{i,j}$ were obtained using the thin plate spline -robust point matching method. This method solves for both the transformation as well as the point-to-point correspondence between the surfaces [101, 103].

With these transformations, we obtain the residue displacement vector fields

$$v_{i,j} = f_{i,j}(S_{i,1}) - S_{i,1} = \{\vec{v}_{i,j}(1), \vec{v}_{i,j}(2), \cdots , \vec{v}_{i,j}(N_{i,1})\} \tag{5.2}$$

where the notation for $v_{i,j}$ is the same as for $S_{i,j}$ in Eq. (5.1). Note that, because $f_{i,1}(S_{i,1}) \equiv 0$, we have $v_{i,1} \equiv 0$. Also, each matrix $v_{i,j}$ for patient i has the same number of columns $N_{i,1}$. The average surface $S_{i,a}$ of patient i is obtained from:

$$S_{i,a} = S_{i,1} + v_{i,avg} \tag{5.3}$$

with $v_{i,avg} = \frac{1}{N_S} \sum_{j=1}^{N_S} v_{i,j}$

Construction of the population averaged CTV surface (*popCTV*)

A specific patient average shape is chosen ($S_{1,a}$) and non-rigid transformations $\{F_i\}$ from $S_{1,a}$ to $S_{i,a}$ are obtained. Similar to Eq. (5.1), the vector fields V_i that map the average surface of patient 1 onto that of patient i ($1 \leqslant i \leqslant N_P$) are

$$V_i = F_i(S_{i,a}) - S_{1,a} \tag{5.4}$$

Again, $V_1 \equiv 0$ by definition. The popCTV surface is obtained as

$$S_{AVG} = S_{1,a} + V_{avg} \tag{5.5}$$

where V_{avg} is the average over *i* of the fields $\{ V_i \}$.

Patient specific systematic and random residue displacements

At each point k ($1 \leqslant k \leqslant N_{i,1}$) spanning the average surface $S_{i,a}$ of patient i, the systematic displacement $\varepsilon_i^n(k)$ along the surface normal $\vec{n}_i(k)$, was obtained from

$$\varepsilon_i^n(k) = \frac{1}{N_S - 1} \sum_{j=1}^{N_S} \vec{n}_i(k) \bullet \vec{v}_{i,j}(k) \tag{5.6}$$

The corresponding SDs of random displacements along the surface normals, $\delta_i^n(k)$, were calculated using,

$$\delta_i^n(k) = \frac{1}{N_S - 1} \sqrt{\sum_{j=1}^{N_S} \left((\vec{v}_{i,j}(k) - \vec{v}_{i,avg}(k)) \bullet \vec{n}_i(k) \right)^2} \tag{5.7}$$

Population systematic and random residue displacements

The systematic and random residue displacements defined in Eq. (5.6) resp. (5.7) are defined on the surface points of each patient specific average CTV surface $S_{i,a}$. We can map these points onto popCTV using the non-rigid transformation of Eq. (5.4). Thus, we obtain N_P values of ε_i^n and δ_n at each point spanning popCTV. The population random displacement σ is calculated by taking the root mean square average of the N_P patient specific random errors δ_n at each point on the popCTV surface. Although ε_i^n is an unbiased estimator of the systematic displacement for patient i, its standard deviation, SD(ε_i^n) slightly overestimates Σ due to a contribution by the random displacements for a finite number of scans (N_S): SD($\varepsilon_i^n)^2 = \Sigma^2 + \sigma^2/(N_S - 1)$ (see Boer; Heijmen [108]. Using σ, this bias was corrected for. Thus obtained maps of Σ and σ were used in Figures 5.2-5.3.

Margin Evaluation in the Presence of Deformation, Rotation, and Translation in Prostate and Entire Seminal Vesicle Irradiation with Daily Marker-Based Set-up Corrections

Theodore F. Mutanga, Hans C. J. de Boer, Gerard J. van der Wielen, Mischa S. Hoogeman, Luca Incrocci and Ben J. M. Heijmen

Abstract

Purpose

To develop a method for margin evaluation accounting for all measured displacements during treatment of prostate cancer.

Methods and Materials

For 21 patients treated with stereographic targeting marker-based online translation corrections, dose distributions with varying margins and gradients were created. Sets of possible cumulative delivered dose distributions were simulated by moving voxels and accumulating dose per voxel. Voxel motion was simulated consistent with measured distributions of systematic and random displacements due to stereographic targeting inaccuracies, deformation, rotation, and intrafraction motion. The method of simulation maintained measured correlation of voxel motions due to organ deformation.

Results

For the clinical target volume including prostate and seminal vesicles (SV), the probability that some part receives <95% of the prescribed dose, the changes in minimum dose, and volume receiving 95% of prescription dose compared with planning were 80.5% ± 19.2%, 9.0 ± 6.8 Gy, and 3.0% ± 3.7%, respectively, for the smallest studied margins (3 mm prostate, 5 mm SV) and steepest dose gradients. Corresponding values for largest margins (5 mm prostate, 8 mm SV) with a clinical intensity-modulated radiotherapy dose distribution were 46.5% ± 34.7%, 6.7 ± 5.8 Gy, and 1.6% ± 2.3%. For prostate-only clinical target volume, the values were 51.8% ± 17.7%, 3.3 ± 1.6 Gy, and 0.6% ± 0.5% with the smallest margins and 5.2% ± 7.4%, 1.8 ± 0.9 Gy, and 0.1% ± 0.1% for the largest margins. Addition of three-dimensional rotation corrections only improved these values slightly. All rectal planning constraints were met in the actual reconstructed doses for all studied margins.

Conclusion

We developed a system for margin validation in the presence of deformations. In our population, a 5-mm margin provided sufficient dosimetric coverage for the prostate.

In contrast, an 8-mm SV margin was still insufficient owing to deformations. Addition of three-dimensional rotation corrections was of minor influence.

6.1   Introduction

To produce dose distributions that remain robust to changing anatomy during treatment delivery, the planning target volume (PTV) is created by expanding the clinical target volume (CTV) with a planning margin [24]. With our previously reported approach for daily prostate positioning, stereographic targeting (SGT) [69], we obtain small residual translational set-up errors using orthogonal kilovoltage (kV) and megavoltage (MV) imaging of prostate-implanted markers followed by remote couch corrections, allowing for smaller planning margins. We previously [86] determined residual displacements at the prostate and seminal vesicles (SV) surfaces with respect to prostate-implanted markers, thus allowing for a more accurate estimate of margins. At the prostate surface these displacements were small compared with the penumbra width of dose distributions. The larger displacements at the SV were mainly rooted in deformations. Under these circumstances, commonly used planning margin recipes [25, 109] derived under assumptions of rigid motion are not applicable. We therefore developed a system for margin evaluation that determines the influence of all known geometric errors (including nonrigid motion) on the delivered dose. Large sets of possible treatment cumulative dose distributions were simulated by moving voxels within the planned dose distribution. Voxel displacements included systematic and random contributions from SGT positioning residues, deformation, rotations, and intrafraction motion obtained from measured patient-specific data. By simulating cumulative dose distributions for a large number of treatments, expected (mean) values of dose-derived parameters with corresponding spreads were obtained to test the robustness of tested planning margins. We applied this system to the case of prostate and SV irradiation, to validate treatment planning margins when using marker-based online corrections. Additionally, we investigated whether planning constraints for the rectum are expected to be met in the delivered cumulated doses.

6.2   Methods and Materials

6.2.1   Patient data and dose distributions

We included 21 prostate patients previously treated with SGT online corrections with clinical staging as follows: T1, 9 patients; T2, 5 patients; and T3, 7 patients. These patients were previously implanted with three to four cylindrical gold markers (length, 5 mm; diameter, 1 mm). All patients received a planning CT scan and three repeat

CT scans throughout treatment. According to our routine clinical protocol, patients received mild laxatives before planning CT acquisition but not for the repeat CT. The prostate, SV, and rectum were delineated on 1.5-mm-thick transversal slices in all CT scans by one observer. The rectal volume was delineated from the level of the ischial tuberosities to the level of the inferior border of the sacroiliac joints [110]. For each patient, we created a clinical intensity-modulated radiotherapy dose distribution and ideally conformal steep-gradient synthetic dose distributions (Figure 6.1). The synthetic distributions allowed for maximum sensitivity to displacements. The clinical dose distributions were created according to our clinical protocol giving 95% of the prescription dose (78 Gy) to 99% of the PTV in 39 fractions of 2 Gy. The rectum was constrained by the fractional volume receiving 83% of the prescribed dose (i.e., V83% = 35%) [111]. The clinical CTV included prostate and SV expanded by 5 mm and 8 mm, respectively. However, for prostate, an additional 2 mm cranial-caudal margin was added at the base and apex to account for steep dose gradients and target definition variability. To create the synthetic dose distributions, the PTV mask was first made and expanded with a margin of 1.64 x estimated penumbra width (σ_p; set to 5 mm in this study). The factor of 1.64 ensures that the 95% isodose line conforms around the intended PTV and was derived from Herk et al. [25] for a one-dimensional scenario. We use it here as an approximation to the three-dimensional (3D) case. The resulting 3D volume was convolved with a 3D isotropic Gaussian kernel of width σ_p. In the resulting distribution, the 95% isodose line follows the PTV and the 50-95% distance conforms to σ_p, except in areas where the radius of local curvature is of the order of, or smaller than σ_p. If the PTV surface is strongly concave or convex, the 95% isodose can be either slightly outside or inside the PTV. We adjusted this local lack of curvature by iteratively adjusting the PTV surface in these areas before the convolution step mentioned above. For margin evaluation and validation, synthetic dose distributions were created for PTVs comprising three different prostate and SV margins, as follows: (1) prostate + 3 mm, SV + 6 mm; (2) prostate + 4 mm, SV + 7 mm; and (3) prostate + 5 mm, SV + 8 mm. Henceforth, these PTVs together with their dose distributions will be referred to as PTV1, PTV2, and PTV3, respectively. The clinical PTV and dose distribution will be referred to as PTV4 (Figure 6.1). The simulation code was written in Matlab (Mathworks, Natick, MA), using routines from a freely available research tool (CERR) [112]. For marker-based registration of CT datasets, we used in-house software written in C++.
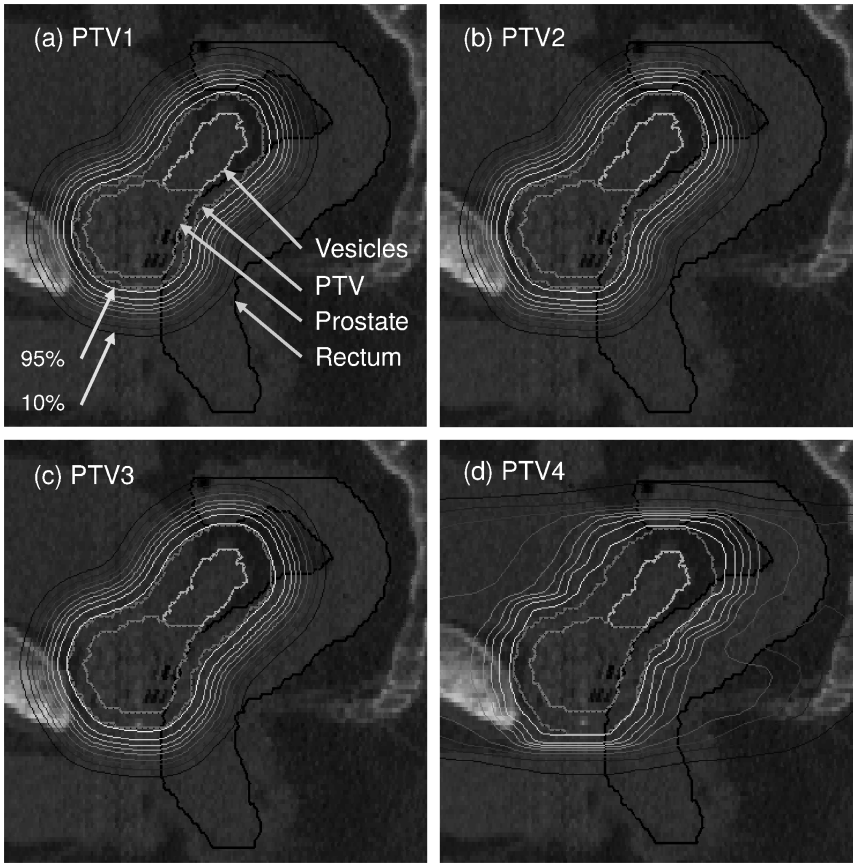
Figure 6.1: Synthetic (a-c) and clinical intensity-modulated radiotherapy (d) dose distributions; clinical target volume-planning target volume (PTV) margins increase from a to d.

6.2.2 Measurement of geometric errors used for simulations

After SGT corrections, three main sources of geometric errors that affect the delivered dose are (1) SGT positioning inaccuracies, (2) deformation and rotation, and (3) intrafraction motion during treatment. Population SDs of systematic ($\vec{\Sigma}$) and random ($\vec{\sigma}$) errors due to (1) and (3) obtained by retrospective analysis of portal MV and kV images are shown in Table 6.1 [69, 113]. We previously quantified residual systematic and random errors due to rotation and deformation at the prostate, SV, and rectum surfaces relative to implanted markers using delineations from repeat CT scans of the patient population described here [86]. Briefly, each repeat CT scan was rigidly registered onto the planning CT scan using the markers as reference. This provided a translation and rotation (3D) about the center of mass of the markers.

Table 6.1: Systematic and random errors used for simulations

Parameter	Systematic (Σ)			Random (σ)		
	LR	AP	CC	LR	AP	CC
Rotations (°)	4.3	2.0	2.2	4.5	1.2	1.8
SGT residues (mm)	0.2	0.4	0.6	0.6	0.8	0.7
Intrafraction (mm)	1.3	1.3	1.3	1.2	1.2	1.2

Abbreviations: LR = left-right; AP = anterior-posterior; CC = cranial-caudal; SGT = stereographic targeting.

The SGT corrections were simulated by applying only the translation (Tonly). Additionally, we applied both translation and rotation (TplusR) to simulate a strategy that also corrects for 3D rotations online. Next, a modified thin-plate-spline-based nonrigid registration method [114] was used to quantify the residue displacements at the organ surfaces, in fact representing deformation relative to the markers. The nonrigid registration automatically estimates point correspondences while solving for the transformation, thus enabling mapping of points between CT scans.

6.2.3 Voxel tracking and simulation of delivered dose

In the reference frame provided by the markers, we modelled the position in 3D $\vec{r}(k, t, f)$ of the kth voxel of a structure in a simulated treatment course t and fraction f as:

$$\vec{r}(k, t, f) = \vec{m}(k) + \vec{s}(k, t) + \vec{\Delta}(k, t, f) + \vec{\alpha}(k, t) + \vec{\beta}(k, t, f) \qquad (6.1)$$

In Eq. 6.1, $\vec{m}(k)$ is the mean position of the voxel, whereas $\vec{s}(k, t)$ and $\vec{\Delta}(k, t, f)$ are systematic and random error contributions due to translational errors (SGT set-up residues and intrafraction motion). $\vec{s}(k, t)$ and $\vec{\Delta}(k, t, f)$ are drawn from 3D normal distributions $N(0, \vec{\Sigma})$ for each simulated treatment and $N(0, \vec{\sigma})$ for each simulated fraction. $\vec{\alpha}(k, t)$ and $\vec{\beta}(k, t, f)$ are vectors obtained from vector fields that describe systematic and random displacements due to deformation and/or rotation, respectively (see Appendix 6.7). Voxel doses for positions from Eq. 6.1 were obtained by interpolating the planned dose distribution. A total of 1000 fractionated treatments (i.e., systematic errors) of 39 2Gy fractions (i.e., random errors) were simulated, corresponding to our clinically applied schedule. The dose per voxel was accumulated over the fractions for each treatment and stored for further analysis.

6.2.4 Analysis of simulated dose distributions

For each accumulated dose distribution we derived the cumulative dose volume histogram (DVH) (Figure 6.2) and dose-volume derived parameters. For each studied margin and patient CTV, distributions of 1000 minimum doses (D_{min}) and 1000 V95% values were thus obtained. Further we computed the probability of underdosage (P_u), which measures the fraction of simulated treatments in which the CTV dose is anywhere <95% of the prescribed dose. In the classic International Commission on Radiation Units and Measurements Report 50 (ICRU-50) concept [24], the CTV-PTV margins should be chosen such that this probability is acceptably small, for example 10% in the commonly used van Herk margin recipe [25]. The P_u was obtained per patient because in contrast to margin recipe assumptions, this probability is patient (as well as dose distribution) specific owing to rotations and deformations.
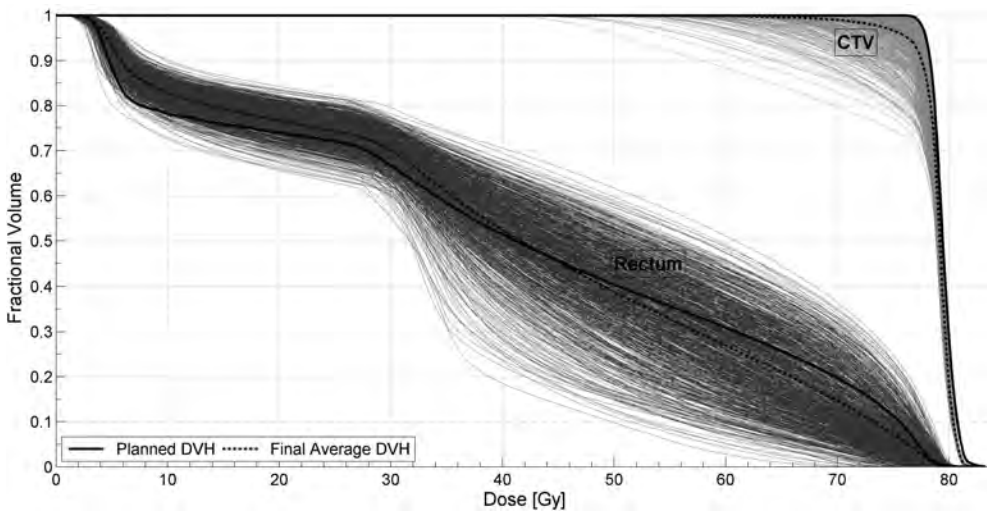
Figure 6.2: Simulated dose volume histograms (DVHs) for the rectum and clinical target volume (prostate plus seminal vesicles) for a clinical dose distribution. The planned DVH (thick solid line) and expected DVH (thick dashed lines) are shown together with the spread (thin lines). Each simulated DVH is based on the accumulated dose over an entire treatment of 39 fractions.

For the rectum, we evaluated whether the V83% planning objective would also be realized during treatment. Furthermore, we obtained values of V50Gy and V70Gy (percentage rectal volume receiving a dose = 50 Gy and = 70 Gy, respectively) [115]. In addition, we computed expectation values for the rectal equivalent uniform dose (EUD) using parameters published from results of a Dutch national dose escalation trial [111]. All dose derived parameters were compared with corresponding

values obtained from the planned dose distribution and the differences summarized for the patient population using the quantities M, Ω, and ω (Figure 6.3). M is the population mean, whereas Ω is the spread around the mean, and ω quantifies the intrapatient spread. The Wilcoxon signed-rank test was used on differences between measured and planned dosimetric parameters, as well as on differences between values obtained for correction strategy Tonly and TplusR, with a threshold of 0.05 for significance.

	Patient 1	Patient 2	...	Patient Np
Treatment 1	$\Delta Q_{1,1}$	$\Delta Q_{1,2}$	...	$\Delta Q_{1,N_p}$
Treatment 2	$\Delta Q_{2,1}$	$\Delta Q_{2,2}$	...	$\Delta Q_{2,N_p}$
...	...	...	...	...
Treatment Nt	$\Delta Q_{N_t,1}$	$\Delta Q_{N_t,2}$	...	$\Delta Q_{N_t,N_p}$

Mean	m_1	m_2	...	m_{N_p}
SD	sd_1	sd_2	...	sd_{N_p}

$$M = \text{mean}(m_1,...,m_{N_p})$$
$$\Omega = \text{SD}(m_1,...,m_{N_p}) \; ; \; \text{SD} = \text{standard deviation}$$
$$\omega = \left((sd_1^{\,2}+sd_2^{\,2},...,+sd_{N_p}^{\,2})/N_p\right)^{1/2}$$
$$\Delta Q = \text{change in parameter (e.g. } D_{min},\text{V95\%)} \text{ from plan}$$

Figure 6.3: Method of summarizing simulated parameters for the patient population. Here, Q is a parameter of interest (e.g., D_{min}).

6.3 Results

6.3.1 CTV coverage

Distributions of D_{min} and V95% for all patients and investigated margins are shown in (Figure 6.4 and Figure 6.5). For both CTV including SV (CTVp+sv) and prostate-only CTV(CTVp), deviations from the planned values decreased with increasing margin size, as expected. All deviations were statistically significant ($p < 0.05$). The

improvement from PTV3 to PTV4 is not only due to the extra 2 mm cranial-caudal prostate margin but also due to the fact that the clinical dose PTV4 has a broader penumbra and therefore is less sensitive to errors. The intrapatient spread (length of error bars in plots) also seems to decrease with larger margins. For the largest margins and clinical dose distribution (PTV4), there was no patient with any measurable deviation in D_{min} and V95% for CTVp, whereas for CTVp+sv there were 3 patients with mean V95% > 2% lower than planned and even more patients with on average >5 Gy reduction in D_{min}. The population statistics for the deviations in D_{min} and V95% for the CTVs are shown in Table 6.2, along with the planned values (patient averaged) for comparison. As with (Figures 6.4 and 6.5), the deviations for D_{min} and V95% were larger if the CTV included vesicles, even for the largest margins. This could be explained by the relative motion and deformation of vesicles with respect to the prostate. In Table 6.3, the mean and SDs (across all patients) of P_u are shown

Figure 6.4: Plots of D_{min} as a function of increasing margins (PTV1-PTV4) for all patients. Closed circles are the mean planned values. Open circles are the mean simulated values. Outer error bars are the 90th and 10th percentiles. Inner error bars are 25th and 75th percentiles. Values are shown for CTVp+sv (top row) and CTVp (bottom row). PTV = planning target volume; CTV = clinical target volume; p = prostate; sv = seminal vesicles.

for all PTVs. Note that P_u was calculated per patient. For the 5 mm prostate margin in PTV4, the average of P_u was 5.2%, well below 10%, and therefore considered clinically acceptable. Note, however, the considerable interpatient spread of 7% not apparent from the standard margin recipe. For CTVp+sv, the mean P_u was larger than 10%, even for the 8 mm vesicle margins. However, the volume that is systematically underdosed can be very small and occur near the tips of the vesicles.
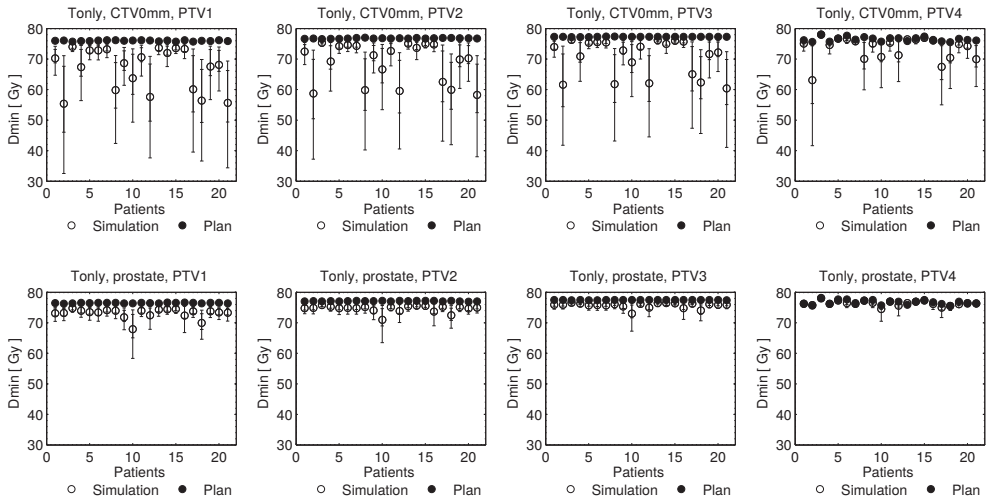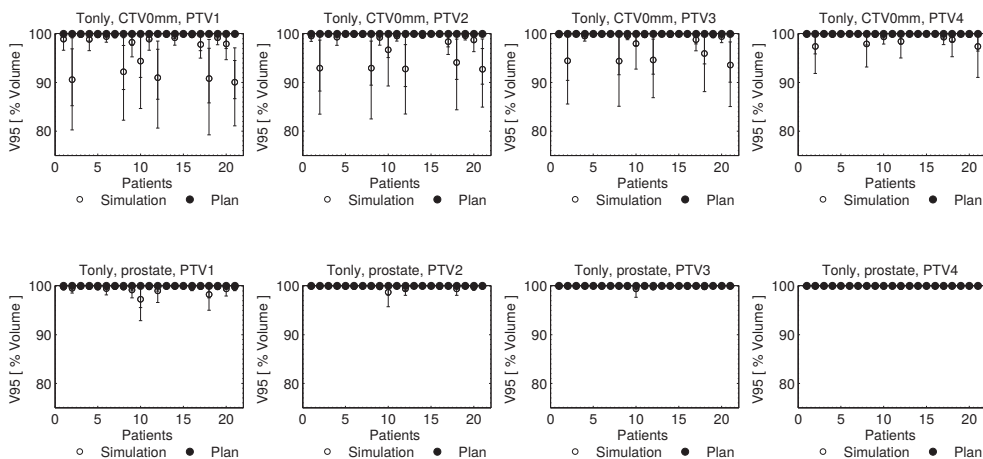
Figure 6.5: Plots of V95% as a function of increasing margins (PTV1-PTV4) for all patients. Closed circles are the mean planned values. Open circles are the mean simulated values. Outer error bars are the 90th and 10th percentiles. Inner error bars are 25th and 75th percentiles. Values are shown for CTVp+sv (top row) and CTVp (bottom row). PTV = planning target volume; CTV = clinical target volume; p = prostate; sv = seminal vesicles.

Table 6.2: Group statistics for the change (plan - simulation) in D_{min} and V95% parameters for CTV including seminal vesicles and for prostate-only CTV

Parameter	D_{min} (Gy)				V95% (% volume)			
	PTV1	PTV2	PTV3	PTV4	PTV1	PTV2	PTV3	PTV4
CTVp+sv								
Plan	76	76.8	77.2	76.5	100	100	100	100
M	9.0	7.8	6.7	2.9	3.0	2.1	1.6	0.6
Ω	6.8	6.4	5.8	3.4	3.7	2.9	2.3	0.9
ω	8.5	8.1	7.5	5.3	3.9	3.4	3.0	1.8
CTVp								
Plan	76.4	77.1	77.4	76.7	100	100	100	100
M	3.3	2.5	1.8	0.3	0.5	0.2	0.1	0.0
Ω	1.6	1.2	0.9	0.6	0.6	0.3	0.1	0.0
ω	2.8	2.2	1.8	1.3	1.1	0.7	0.4	0.1

Abbreviations: CTV = clinical target volume; PTV = planning target volume; p = prostate; sv = seminal vesicles.
All differences were statistically significant (p < 0.05).

6.3.2 Rectum dose

Because the rectum and prostate are in close proximity, prostate marker-based corrections will inherently move the part of the rectal wall close to the prostate into the same (high) dose region. Next to that, the large deformations of the rectum will lead to a considerable amount of dose blurring (Figure 6.2). Table 6.4 shows the dose-

Table 6.3: Mean and SD (across all patients) of the probability of CTV underdosage (P_u) for CTV including seminal vesicles and for prostate-only CTV

Parameter	PTV1	PTV2	PTV3	PTV4
P_u, CTVp+sv (%)				
Mean	80.5	59.6	46.5	28.8
SD	19.2	31.1	34.7	26.9
P_u, CTVp (%)				
Mean	51.8	23.5	11.0	5.2
SD	17.7	16.6	12.8	7.4

Abbreviations as in Table 6.2.

derived parameters for the rectum as a function of PTV margins. There is a slight tendency for V50Gy to increase and for V70Gy to decrease (although not all statistically significant). However, the maximum mean deviation in V50Gy and V70Gy remained small: -1.5% (SD, 2.7%) and 1.5% (SD, 2.5%) for all the margins. Table 6.4 also shows that the changes of the V83% planning objective and the rectal EUD compared with plan were all small and mostly not statistically significant for all the margins.

Table 6.4: Group statistics for the change (plan - simulation) in rectal parameters V50Gy, V70Gy, V83%, and EUD

Parameter	PTV1	PTV2	PTV3	PTV4
V50Gy (% volume)				
Plan	22.2	24.6	27.1	36.6
M	-0.2	-0.1	-0.1	-1.5[*]
Ω	2.7	2.8	2.7	2.7
ω	4.8	5	5.2	5.4
V70Gy (% volume)				
Plan	10.2	12.2	14.2	17.6
M	1.2	1.4[*]	1.5[*]	0.9
Ω	2.2	2.5	2.4	2.4
ω	3.2	3.5	3.8	4.3
V83% (% volume)				
Plan	14	16.2	18.4	22.7
M	1.0	1.1	1.1	0.2
Ω	2.5	2.7	2.6	2.5
ω	3.8	4.1	4.3	4.8
EUD (Gy)				
Plan	57.3	58.5	59.7	62
M	1.1[*]	1.1[*]	1.1[*]	0.5
Ω	1.8	1.6	1.5	1.2
ω	2.7	2.5	2.4	2.2

Abbreviation: EUD = equivalent uniform dose. Other abbreviations as in Table 6.2
[*] Statistically significant ($p < 0.05$)

6.3.3 Rotation corrections

To assess the impact of additional online rotation corrections, we looked at the differences in the dose-derived parameters obtained with TplusR compared with those obtained with Tonly (Tables 6.5 and 6.6). Both tables show that the impact of rotation becomes smaller with increasing margins, as expected. In Table 6.5, the population mean values for differences in D_{min} and V95% for CTVp+sv were mostly negative, implying that rotation corrections seem to improve on average CTV coverage but only modestly so; the maximum increase in population D_{min} and V95%with additional rotation corrections for any margin were 1.2 Gy (SD, 4.6 Gy) and 1.1% (SD, 2.8%), respectively. For CTVp, differences between Tonly and TplusR were hardly noticeable. In Table 6.6, positive values of the differences in rectal parameters between Tonly and TplusR indicate that the rectal dose was reduced with rotation corrections, but this effect was also very small.

Table 6.5: Group statistics for the difference Tonly - TplusR of D_{min} and V95% for CTV including seminal vesicles and for prostate-only CTV

	D_{min} **(Gy)**				V95% **(% volume)**			
Parameter	**PTV1**	**PTV2**	**PTV3**	**PTV4**	**PTV1**	**PTV2**	**PTV3**	**PTV4**
CTVp+sv								
M	-1.1	-1.2	-1.2	0.0	-1.0	-0.8	-0.7	-0.2
Ω	5.1	4.9	4.6	3.1	2.8	2.3	1.9	0.8
ω	11.4	10.7	9.9	7.7	4.8	4.1	3.5	2.1
CTVp								
M	0.3	0.3	0.2	0.0	0.1	0.1	0.0	0.0
Ω	0.8	0.7	0.6	0.3	0.3	0.2	0.1	0.0
ω	4.3	3.5	2.8	1.9	1.7	1.1	0.6	0.2

None of the differences were statistically significant (p > 0.05).
Abbreviations: Tonly = translation only; Tplus 4 = translation plus rotation. Other abbreviations as in Table 6.2.

6.4 Discussion

We have developed a method to optimize and validate planning margins without using a margin recipe. Such an approach is necessary because margin recipes no longer hold in the presence of deformations, relative organ motion, and rotations. Importantly, our simulations show that there is considerable interpatient spread in probability that part of the CTV is underdosed. Such a spread is not predictable in the framework of margin recipes. For our clinical intensity modulated radiotherapy technique, combined with online SGT, a 5 mm margin seems appropriate for the prostate on average. We found that the clinically applied 8 mm margin for the SV

Table 6.6: Group statistics for the difference Tonly - TplusR for rectal parameters V50Gy, V70Gy V83%, and EUD

Parameter	PTV1	PTV2	PTV3	PTV4
V50Gy (% volume)				
M	1.1*	1.1*	1.1*	0.7
Ω	2.2	2.3	2.4	2.5
ω	6.7	7.1	7.4	7.9
V70Gy (% volume)				
M	0.6	0.6	0.8*	0.8
Ω	1.3	1.5	1.6	2.1
ω	4.5	4.9	5.3	6.1
V83% (% volume)				
M	0.8*	0.8*	1.0*	1.0
Ω	1.6	1.8	1.9	2.4
ω	5.3	5.7	6.1	6.8
EUD (Gy)				
M	0.5	0.4	0.4	0.3
Ω	1.3	1.2	1.1	0.9
ω	3.7	3.5	3.3	3

Abbreviations as in Table 6.2 and Table 6.4.
* Statistically significant ($p < 0.05$).

was not really safe when testing with synthetic dose distributions. It was, however-er, also observed that for clinical dose distributions with a wider penumbra, using 8 mm was clinically acceptable regarding vesicle coverage. The clinical decision was therefore made to continue with the use of 8 mm margins. The commonly applied margin recipe for translational uncertainties (van Herk) has been derived with synthetic dose distributions. Although we did not test this in this study, it may well be that these margins are too generous, depending on the treatment site/individual patient anatomy and quality of the clinical dose distributions. Although we report on population margins in this study, we are currently investigating application of the methodology to customize margins for the individual patient in the framework of adaptive radiotherapy. Modelling the impact of set-up error and organ motion on delivered dose distributions by the Monte-Carlo simulations presented here is not new and has been reported elsewhere [116–120]. However, most of these studies evaluated dosimetric effects of rigid motion set-up error and organ motion during prostate radiotherapy, but few included dosimetric effects due to organ deformation. Yan et.al.[117] used finite element modelling and biomechanical properties of tissues elements to obtain vector displacements used for simulating organ deformations. Söhn et al. [121] have used principal component analysis on multiple CT scans to calculate surface displacements of organ boundary points due to deformation. The novelty in our methods is that the method simulates deformations that maintain observed patient-specific systematic and random deformations and correlations within the deformation vector fields even for a limited number of input volumetric datasets

per patient. Witte et al. [122] reported on a method to produce dose distributions that are robust to patient/organ displacements during treatment delivery without relying on margins. They incorporated displacements directly into the optimization process during treatment planning for the case of rigid body motion. However, they ignored rotation and deformations. Inclusion of deformations will be computationally infeasible because this will involve repeated sampling of the deformation space of each individual voxel before the optimization step, which is already computationally expensive. Our approach is different in that we first create dose distributions for selected margins and then evaluate the robustness of each dose distribution by simulating the actual dose delivered. Meijer et al. [105] presented margins for the prostate and for the first 2 cm of the SV, taking deformation into account. However, they neither evaluated dose to the rectum nor dose to the entire vesicles. Nevertheless, to the extent of the first 2 cm of the SV, the 7 mm margin derived in Meijer et al. is consistent with our results. Although we investigated margins for full dosimetric coverage of the SV, it is still unclear whether this is imperative, even if the risk of invasion is high. There are very limited data as to what length of the vesicles contains demonstrable tumour cells, what their density is, and therefore what proportion of the vesicles should be treated to what dose level [20]. Still, our model can be applied to optimize margins and ultimately dose distributions if assumptions on the clonogenic density are made [88]. The benefit of rotation corrections in addition to translation corrections was insignificant for the CTVp and modest at best for CTVp+sv, with high patient and treatment variation. The simulated rotation corrections were fully determined by the markers implanted in the prostate. The prostate is almost spherical, which explains the insignificance of the rotation corrections. The SV are flexible and can move to a large extent independently of the prostate and markers. Therefore, the marker-based rotation corrections only have a minor impact on SV treatment accuracy. Two studies [123, 124] reported significant gains in rotation corrections with SV included in the CTV, but both studies treated the CTV (prostate plus SV) as a rigid body. Concerning the rectum, all final accumulated doses were on average still in compliance with the original planning objective (i.e., V83% =35%). The changes in rectal dose-derived parameters with respect to treatment planning were small in general (Table 6.4). It seems that prostate marker-based corrections bring the average treatment rectal DVH in close proximity to the planned DVH. Again, there are notable patient-specific variations in organ shape and deformation, and therefore the rectal dose in one individual treatment can still significantly differ from the intended dose distribution. We have focussed on how organ motion and deformation cause deviations in delivered dose distributions. To translate these deviations into expected treatment outcomes a radiobiological analysis, using validated models for tumor

density and spread, normal tissue complications, and interpatient heterogeneity is required. For instance, it is obvious that the CTV underdosage probability P_u used to derive margin recipes, although indicative for how well the ICRU-50 criteria are met, has little predictive value for tumor control probability for the SV. Indeed, the interpretation of P_u in general is cumbersome because it provides no information on the size or location of the underdosage. Although beyond the scope of the present study, we will investigate the expected outcome of such radiobiological endpoints.

6.5 Conclusion

We described a framework for margin evaluation and validation taking into account organ deformation. We applied the framework to the case of prostate and entire vesicle irradiation. With marker-based corrections, a prostate margin of 5 mm was adequate, whereas an 8-mm margin still did not guarantee coverage for the entire SV to the prescribed level. Our results show that the additional benefit from full rotational corrections is small for the finally delivered CTV dose, even if the vesicles are part of the CTV.

6.6 Acknowledgments

The authors thank Marjolein van Os and Mascha van de Laar for their input in creating and validating the clinical treatment plans; and Wilco Schillemans and Davy Wentzler for developing the marker registration tool.

6.7 Appendix

6.7.1 Simulation of shape deformations from a limited set of repeat CT scans

In each patient i ($1 \leqslant i \leqslant N_P$), organs are delineated in each CT scan j ($1 \leqslant j \leqslant N_S$; j = 1 is arbitrarily chosen as reference scan). The so obtained organ surface meshes $S_{i,j}$ can be represented as a collection of $N_{i,j}$ 3D vectors $\vec{r}_{i,j}(k)$, each vector representing a surface point:

$$S_{i,j} = \{\vec{r}_{i,j}(1), ..., \vec{r}_{i,j}(N_{i,j})\}; \vec{r}_{i,j}(k) \in \Re^3 \tag{6.2}$$

Each repeat CT scan ($j > 1$) is rigidly registered with CT1 using the implanted markers.

Two cases were studied:

1. apply only the translation

$$S_{i,j}^{t} = S_{i,j} + T$$

2. apply both translation and rotation

$$S_{i,j}^{t} = RS_{i,j} + T$$

We continue with transformed surfaces, $S_{i,j}^{t}$, which are now in the marker-based coordinate frame of CT1, dropping the superscript t and i. for readability.

6.7.2 Calculating patient average displacement vectors and random deformations

For a patient, we obtain non-rigid transformations $f_j (j > 1)$ mapping the points of reference surface S_1 to points on repeat scan surface S_j using the thin plate spline robust point matching (TPS-RPM) algorithm [114]. With these transformations, we obtain the displacement vector fields:

$$v_j = f_j(S_1) - S_1 = \{\vec{v}_j(1), \vec{v}_j(2), \cdots, \vec{v}_j(N_1)\} \tag{6.3}$$

where the notation for v_j is the same as for S_j in Eqn.6.2. Note that, because $f_1(S_1) \equiv S_1$, we have $v_1 \equiv 0$. Also, each matrix v_j has the same number of columns (i.e., displacement vectors) N_1. The mean position of a point k then becomes:

$$\vec{m}(k) = \vec{r}_1(k) + \vec{v}_{avg}(k)) \tag{6.4}$$

with

$$\vec{v}_{avg}(k) = \frac{1}{N_S} \sum_{j=1}^{N_S} \vec{v}_j(k)$$

Let x^d be the vector component in direction d of vector $\vec{x}$. $\delta_j^d(k) \equiv v_j^d(k) - v_{avg}^d(k)$. At each point k ($1 \leqslant k \leqslant N_1$) the SDs of random displacements in direction d was calculated from:

$$\sigma^d(k) = \sqrt{\frac{1}{N_S - 1} \sum_{j=1}^{N_S} (\delta_j^d)^2} \tag{6.5}$$

6.7.3 Simulating displacements of volume elements

Without *a priori* information, one may assume that displacements caused by deformations are (nearly) normally distributed, with SD at point k given by Eqn. 6.5 i.e. according to distribution $N(m^d(k), \sigma^d(k))$ for direction d. However, because the displacements of many points are highly correlated (e.g., if the tip of the vesicle goes up, so does almost the entire vesicle) we cannot simulate them by drawing numbers from normal distributions for each point k independently. Principal component analysis (PCA) ([121]) can provide displacement vector fields that represent modes of correlated movement, but requires a large number of datasets per patient to yield a reliable analysis. Here, we take a different approach. We simulate deformations that contain the observed shapes and correlations and simultaneously are consistent with the mean positions in Eqn. 6.4 and SDs of Eqn. 6.5.

We first linearize the problem (as PCA does), by writing possible positions of all points k as

$$r^d(k) = m^d(k) + C \sum_{j=1}^{N_S} a_j \delta_j^d(k) \tag{6.6}$$

where C is a normalization constant for later convenience. In this equation, the a_j are stochastic variables and thus the only simulated variables. Hence, Eqn. 6.6 supposes that linear combinations of the observed deformation vector fields are possible within limits derived below. The correlations within any observed deformation field are maintained because a_j is independent of k and d. As a corollary, there can never be overlap between two organs for any point satisfying Eqn. 6.6.

To derive distributions for a_j, we pose that they are normally distributed (see above) with variance equal for each j, i.e. as $N(0, \sigma_a)$. The identity of the variances reflects that each input CT scan can be treated as equal (no bias). We now demand that the local SDs of Eqn. 6.5 are conserved in the simulations. Specifically, for simulated fraction f we get

$$r^d(k, f) = m^d(k) + C \sum_{j=1}^{N_S} a_j(f) \delta_j^d(k) \tag{6.7}$$

with notation:

$$< a >_i = \lim_{N_x \to \infty} \frac{1}{N_x} \sum_{i=1}^{N_x} a(i) \text{ and } SD_i^2(a) = \lim_{N_x \to \infty} \frac{1}{N_x - 1} \sum_{i=1}^{N_x} [a(i) - < a >_i]^2$$

we obtain:

$$\text{SD}_f^2(r^d(k,f)) = C^2 \sum_{j=1}^{N_S} \sigma_a^2 [\delta_j^d(k)]^2 = C^2 \sigma_a^2 (N_S - 1)(\sigma^d(k))^2 \equiv (\sigma^d(k))^2 \qquad (6.8)$$

where the last equality is the posed demand. In deriving Eqn. 6.8 we use:

$< a_l(f)a_m(f) >_f = \delta_{l.m}$ (Kronecker delta).

Hence, if we put the normalization constant $C = \frac{1}{\sqrt{N_S - 1}}$, we obtain $\sigma_a = 1$. Note that we can satisfy Eqn. 6.8 for each d and k with the same C and σ_a value, which is a necessity for the model of Eqn. 6.6.

In conclusion, we can simulate a deformed state in fraction f by drawing N_S numbers $a_j(f), j = 1, \ldots, N_S$ from a normal distribution $N(0,1)$ and then calculate the coordinates of each point k from:

$$\vec{r}(k,f) = \vec{m}(k) + \frac{1}{\sqrt{N_S - 1}} \sum_{j=1}^{N_S} a_j(f)\vec{\delta}_j(k) \qquad (6.9)$$

where we have switched to vector notation again as the Eqn. 6.6 is identical for every direction. Eqn. 6.9 applies to points at the surface, but it can also be applied to any point p within that surface as long as $\vec{m}(p)$ and $\vec{\delta}_j(p)$ are known (which we obtain from interpolation)

6.7.4 Systematic and random displacements

If treatments are denoted by t, then the positions of a point k in a treatment can be described as an extension of Eqn. 6.9:

$$\vec{r}(k,f,t) = \vec{m}(k) + \vec{\varepsilon}(k,t) + \frac{1}{\sqrt{N_S - 1}} \sum_{j=1}^{N_S} a_j(f,t)\vec{\delta}_j(k) \qquad (6.10)$$

where the systematic displacement $\vec{\varepsilon}(k,t)$ is introduced. For reasons of symmetry (systematic and random deformations have the same distributions if all used scans are comparable), we immediately obtain that both systematic and random deviations can be simulated from

$$\vec{r}(k,f,t) = \vec{m}(k) + \frac{1}{\sqrt{N_S - 1}} \sum_{j=1}^{N_S} b_j(t)\vec{\delta}_j(k) + \frac{1}{\sqrt{N_S - 1}} \sum_{j=1}^{N_S} a_j(f,t)\vec{\delta}_j(k) \qquad (6.11)$$

with each $b_j(t)$ drawn from normal distribution $N(0,1)$. Finally, to include full geometrical errors, including systematic and random rigid motion contributions, Eqn. 6.11 is updated with the corresponding offsets to obtain Eqn. (6.1) in the manuscript.

CHAPTER 7

Discussion

7.1   Introduction

In prostate radiotherapy, geometric errors due to target localization uncertainty at the time of treatment have always been a major drawback to the achievable accuracy with which treatments can be delivered. image guided radiation therapy (IGRT) and adaptive radiation therapy (ART) have been introduced in order to encourage methods that can be used to efficiently minimize these geometric uncertainty and consequently improve the final outcome of radiotherapy treatments. Clinical solutions for reducing target localization uncertainties on a daily basis and also within the treatment have not been widespread, in a large part due to the potential increases in clinical workload.

The use of implanted markers in combination with electronic portal imaging device (EPID) imaging in a highly automated workflow allow for improved prostate positioning with sub-mm accuracy on a daily basis. With our StereoGraphic Targeting (SGT) and intrafraction StereoGraphic Targeting (iSGT) procedures, this has been achieved with little imaging specific dose prior to and during the treatment fraction within a few seconds in a single software environment(Chapter 2 and Chapter 4). The ensuing corrections executed by remote controlled couch shifts (technician does not enter treatment room) are performed with an accuracy better than 0.3 mm. Hence for translation errors, the systematic errors (SD) of the center of mass (COM) of the markers can be reduced to $\Sigma \leqslant 0.7$ mm and random errors to $\sigma \leqslant 0.9$ mm, allowing for smaller clinical target volume (CTV)-planning target volume (PTV) margin.

In this chapter, other solutions for prostate IGRT will be discussed paying attention to some key differences compared to the marker-based approach described in this thesis. With translation corrections in iSGT and SGT, organ deformation and rotation errors still remain(Chapter 5). The issue of whether or not to perform rotation corrections in addition to online translation corrections with marker-based positioning will be discussed. It was shown in Chapter 5 that margin reduction for the prostate is possible but if seminal vesicles are included in the CTV, locally enlarged margins are required mainly due to deformation and rotation errors of the seminal vesicles. Here, the margin choices obtained with our evaluations will also be discussed in connection with the issue of whether or not to include the seminal vesicles in the target.

For the residual errors that cannot be corrected by simple marker-based couch translations, ART offers possible options to compensate for accounting for these types of errors. Some future ideas relating to accounting for these residual errors and the extent to which possible ART schemes can be realized in the context of the IGRT

scheme in this thesis will also be presented.

7.2 Other IGRT approaches to patient positioning

Various solutions for tackling the problem of patient (re)positioning in prostate radiotherapy fall under three main categories: (i) bony anatomy based registration, (ii) alignment based on registration of implanted fiducial markers (this thesis) or (iii) alignment based on soft-tissue image registration . Although these techniques could be useful in their own right, implanted markers offer some unique properties which allow them to be used in combination with other techniques (for instance volumetric cone beam CT) to achieve a higher positioning accuracy.

For bony anatomy based positioning, generally portal images are obtained prior to treatment and compared with simulator radiographs or digitally reconstructed radiographs (DRRs). However, it has been shown that bony anatomy based set-up solutions for prostate positioning are unreliable due to relative motion between the bony anatomy and the prostate resulting from organ motion and deformation [125]. In addition, not only is the registration accuracy of bony anatomy low [126] compared to registration on makers, for bony anatomy based positioning solutions, interpretation and analysis of image registration is user subjective and usually not performed fast enough in order to be applicable in an online correction setting [127].

Computed tomography (CT) [128, 129], cone beam computed tomography (CB CT) [32, 33, 130, 131] and 3D ultrasound imaging [132–134] have been introduced in the treatment room to provide volumetric anatomical information of the patient in the treatment position directly before or during [69, 135] the treatment delivery. This has the powerful advantage that the patient can be positioned based on the actual 3D anatomy on the treatment day. Furthermore, if correct relative electron densities (in Hounsfield units (HU)) can be obtained, the 3D dataset can be used for re-planning, for instance, if drastic systematic anatomic deformations are observed. A common requirement of all these volumetric imaging based solutions is the registration of the treatment image to the planning CT image. A grey-value based soft-tissue registration method is often applied for these systems but this is highly sensitive to motion-induced artifacts. A serious problem for prostate soft-tissue based cone beam computed tomography (CBCT) registration is caused by moving gas in the rectum during acquisition, which degrades the registration accuracy. Attempts to limit rectal gas and improve image quality by using a diet regiment for volumetric CBCT scanning had limited success [136]. For higher accuracy, the soft-tissue registration was abandoned [137] in favour of registration based on implanted markers which provide a

fixed frame of reference and guaranteed high registration accuracy. In the SGT and iSGT systems, the presence of the linear accelerator (linac) mounted kV imager with volumetric CBCT capability is an added advantage which can be exploited for ART.

Several studies have demonstrated the superiority of marker-based prostate positioning compared to ultrasound based positioning in terms of accuracy [132–134] and margin reduction [134]. One problem with ultrasound is the systematic error caused by probe pressure. Although this systematic error could be corrected for, there will still be large differences between ultrasound shifts and shifts obtained by marker matching. The large variability in ultrasound match results could be attributed to inter user variability and experience. While ultrasound uses non-ionizing radiation for patient positioning, there are still no solutions based on ultrasound capable of automated intrafraction prostate positioning [138].

An emerging promising approach for IGRT involves hybrid magnetic resonance imaging (MRI)-linac systems where a diagnostic quality MRI scanner is built into a linac. The MRI imaging capability allows for excellent soft-tissue contrast to enable real-time image guidance during treatment [139]. Clinical usage of such systems are not yet available, but prototypes are being tested.

7.3   Rotation corrections

The potential of performing rotation corrections in addition to the translation corrections was investigated in Chapter 5 and Chapter 6. Both from geometry and dosimetry based analyses(Chapter 5 and Chapter 6), it was found that marker-based rotation corrections could improve and deteriorate dose coverage of the seminal vesicles, depending on the patient and fraction. For the prostate gland itself the rotation corrections were of minor influence. A possible explanation for the former is that the marker rotations are not representative of the seminal vesicle motion since the later move and deform largely independently of the prostate in which markers are placed. The latter observation can be explained by fact that the prostate shape is approximately spherical, hence it not too surprising that the COM-derived rotation corrections have negligible influence. For the patient population described in the studies in Chapter 6, the gain from rotation corrections is insignificant, and margins close to 1 cm are still required for full vesicle coverage. This larger margin is required largely to cover for mainly deformation errors at the seminal vesicles. Recently, Smitsmans et al. [137] published a study on 13 patients to quantify residual interfraction displacement of seminal vesicles (SV) and investigate the efficacy of rotation correction on SV displacement in a marker-based IGRT system using CBCT volumetric images.

They also conclude that rotation correction did not reduce residual seminal vesicle displacements due to the fact that a large part of the motion of the seminal vesicles relative to the prostate gland is not captured by the marker position.

In contrast to our results and those of Smitsmans et al. [137], other authors have shown improvement of the delivered dose when correcting for rotations in addition to translation positioning error [124, 140]. However, these rotations were derived by registering the prostate and seminal vesicles together as a single structure. By doing so, motion of the vesicles relative to the prostate was (partly) included in the registration. Further, this type of rotation correction requires online volumetric imaging and (soft-tissue based) registration.

7.4   Margins and inclusion of seminal vesicles in the CTV

The reduction of positioning errors using both interfraction and intrafraction translation corrections allows for the use of margins of about 5 mm for the prostate alone and at least 8 mm for the seminal vesicles. These values were estimated based on the geometric analyses of Chapter 5 and further evaluated in the dosimetric analyses of Chapter 6 , using both synthetic and clinically delivered dose distributions. In these investigations, an estimate of the inter-observer delineation uncertainty was included in the calculations. In Chapter 5 little deformation of the prostate corpus was observed. The smaller prostate margin adequately accounts for mainly target delineation uncertainties, residual set-up errors and the small prostate deformations(Chapter 6).

The inclusion (and extent of) the seminal vesicles in the CTV is one of the controversies in prostate radiotherapy today. This is particularly important because inclusion of (part of) the seminal vesicle in the target inherently places a larger area of high dose close to or overlapping with the rectum. This therefore has the potential for increased toxicities for patients treated with full (or partial) seminal vesicles included in the CTV. Kestin et al. [20] carried out a study on biopsy samples to investigate the presence and extent of visible tumour in the seminal vesicles of radical prostatectomy specimens. In that study, approximately 1% of the 344 specimens had any risk of seminal vesicle involvement at a distance larger than 2.0 cm from the base of the prostate. Based on this study and a few others [20, 141, 142] with similar results, a number of centres have adopted a protocol including only the first 2 cm of the seminal vesicles in the target volume. However, because these studies included only patients with T1 or T2 tumour stage, there is no clear evidence that only part of the seminal vesicles should be treated for higher risk patients (>= T3 tumour stage). Us-

ing our data, we can estimate that margins of the seminal vesicles could be reduced to about 7 mm for the lower risk patients if only the first 2 cm of the seminal vesicle is included in the target. For full vesicle coverage however, margins >8 mm will be required. These margins were estimated based on how organ motion and deformation cause deviations in delivered dose distributions (see Chapter 6).

A preliminary radio-biological study was carried out to evaluate the equivalent uniform dose (EUD), tumour control probability (TCP) and normal tissue complication probability (NTCP) for the proposed margins assuming constant tumour density and using estimated parameters from literature [88]. The results from this evaluation were in support of the conclusions arrived at in the dosimetric analysis in Chapter 6. For the prostate, a margin of 4-5 mm with marker-based online corrections was adequate to prevent any loss in TCP for all patients. For the seminal vesicles, an 8 mm margin could not prevent TCP loss for some patients due to deformation errors. The rectal EUD and NTCP were in general close the the planned values, probably due to online translation corrections. To estimate the true expected treatment outcomes, a full radio-biological analysis using validated models for tumour density and spread, normal tissue complications, and inter-patient heterogeneity is required.

7.5   Future directions

7.5.1   Introduction

In the general framework of adaptive radiation therapy (ART), volumetric images (CBCT [130], MRI [139, 143]) taken just before treatment delivery give a 3D picture of the actual anatomy on the treatment day. These images can then be used in an offline or online setting to adapt the treatment to changes observed in the images.

Evidently, translation corrections based on implanted markers are not optimal, especially if full seminal vesicle coverage is required. In this case, adaptive radiotherapy might yield some benefits. Furthermore, although with marker-based set-up correction, observed dosimetric variations in the rectum were on average small compared to planning, adaptive radiotherapy might be used to reduce the large inter-patient variations. ART strategies are increasingly more popular in prostate radiotherapy [91, 130, 144, 145].

7.5.2   Online adaptive radiotherapy for prostate cancer

One possible approach for online ART could involve first creating a set of treatment plans with various degrees of anatomic variations and set-up errors for an individual patient. On the treatment day, a "plan of the day" can be selected from the set of pre-created plans and delivered. This selection can be based on observations of the anatomy in the in-room imaging (for example CBCT already present on the linac) image and the isocenter shift is determined from markers registrations. During dose delivery, between beams, if necessary, intrafraction corrections could then be corrected with iSGT. The implementation of such of an approach will require the following tools: 1) auto-segmentation tools for automatic delineation of anatomic structures from the CBCT image 2) rigid and non-rigid registration as well as modelling tools to create simulated anatomies (see Chapter 6 and [146]) and 3) fast (template-based) planning to create a range of acceptable treatment plans for each anatomic variation.

In another approach [147], which simplifies evaluation of the treatment, only a limited number of treatment plans could be created before hand; for example, a plan for a full rectum and/or bladder, empty rectum and/or bladder, and something in between. On a treatment day only one of these plans is selected based on the state of the anatomy as observed on the in-room CBCT, using marker registrations to provide the isocentre shift.

A full online ART approach can also be implemented to make use of online planning or re-optimization of the planed dose using deformation fields obtained from registering the in-room CBCT and the original planning CT [145, 148, 149]. Fast online planning algorithms are not yet available but it is now possible to quickly re-optimize the initial planned dose on the new anatomy in <2 minutes [149]. After such a plan re-optimization the dose is delivered and iSGT is still used to correct for intrafraction errors within the fraction. This approach will require reliable and fast tools to perform auto-contouring (auto-segmentation) of the anatomic structures on the in-room image.

7.5.3   Probabilistic planning

Another offline ART strategy that does not require the use of margins is to incorporate the residual errors (especially organ deformation error) into the treatment planning optimization proces [122, 150, 151]. The planning can be performed on a probability distribution of possible patient geometries instead of a single snapshot from the planning CT. The method presented in Budiarto et al. [146] can be used for

the creation of possible geometries using first the patient anatomy from the planning CT scan together with anatomies of similar patients. The probabilistic plan created as such can then be updated after obtaining more patient-specific data for example from repeat CBCTs. The benefit of this approach is that the geometric variations of the target and organs at risk (OAR) are taken into account directly in the dose optimization process, resulting in a robust dose distribution with an improved balance between target coverage and OAR sparing compared to conventional planning [122].

The required tools mentioned above are already available from research and development at our institute. Fast and robust non-rigid registration algorithms based on robust point matching has been available [114] and was used extensively in the work in this thesis. A new tool, Atlas-Based Auto Segmentation (ABAS)[152], is currently under evaluation for the automatic contouring of anatomic organs from CBCT for use in prostate radiotherapy. Fast plan re-optimization based on *Lagrange multipliers* is now possible [149] using tools developed at our institute.

The main issue that remains to be solved before implementing an adaptive strategy clinically is a work-flow manager to handle all the aspects of integration and communications between imagers, registration software, planning systems and the treatment machine. Prior to clinical implementation, these strategies will have to be evaluated for example using software simulations and anatomic modelling algorithms presented in Chapter 6 and Budiarto et al. [146] in order to determine the most effective strategy.

Summary

Prostate cancer is the most prevalent form of cancer and the second leading cause of cancer-related deaths in males after lung cancer [1, 2]. external beam radiation therapy (EBRT) is one of the main treatment options and involves application of doses of radiation to the target volume while avoiding the normal tissues (organs at risk (OAR)) as much as possible. The treatments are usually delivered in small fractions over several weeks (5-6 weeks) thus requiring accurate and reproducible patient positioning during delivery. The last few decades have seen substantial improvements in more conformal techniques for EBRT delivery with increasing ability to shape the radiation dose to conform [4–8] to the target shape while avoiding the OAR. Based on the premise that these conformal treatment delivery techniques will yield a better therapeutic ratio, even higher fraction (or total) doses are being used for potentially better tumour eradication [153–156]. This combination of more conformal EBRT dose distributions with steep dose gradients towards the OAR will increase the risk of missing the target and potentially increasing toxicities to OAR. Coupled with the highly conformal dose distributions, higher fraction and/or prescription doses imply that the negative impact of a geographic miss could be more damaging. Therefore, the implementation of appropriate measures to guarantee high precision in treatment delivery is of the utmost importance for contemporary prostate radiotherapy.

This need for very high precision in target localization has in turn encouraged research in in-room imaging technologies such as electronic portal imaging devices (EPIDs) and cone beam computed tomography (CBCT), enabling the development of image guided radiation therapy (IGRT) treatment techniques. In designing these IGRT techniques, it is desirable if analyses can be automated to reduce workload while making use of standard evaluation tools already present on the linac.

The research in this thesis was focused on systems and methods for time- and workload efficient correction strategies for prostate positioning during EBRT using the general framework of IGRT. To this end, a system designated StereoGraphic Targeting (SGT) was designed for daily interfraction positioning and later extended for intrafraction prostate repositioning using imaging of implanted markers and subsequent software-controlled position adjustments. The main advantages of these systems are: (1) minimal increase in fraction duration (2) high possible accuracy (3) minimal workload from imaging, image evaluation and position adjustments (couch shifts) (4) minimal additional imaging dose. Another important objective of the research in this thesis was the assessment of residual errors including especially organ

deformation and rotation errors remaining after translation corrections and the assessment of appropriate planning margins to account for them.

Chapter 1 is a general introduction of the thesis, describing some of the concepts related to prostate cancer treatment by EBRT. The main objectives and the scope of the thesis are also defined in **Chapter 1**.

In **Chapter 2**, a fully automated, fast, online prostate repositioning scheme was developed and clinically applied. Prostate positioning was achieved using orthogonal kilovoltage/megavoltage imaging of implanted markers and remote couch movements . The initial clinical results of this StereoGraphic Targeting (SGT) method, as well as phantom evaluations, are presented. With SGT, the SDs of the systematic center of mass (COM) positioning errors (Σ) were reduced from 4.0 mm to < 0.5 mm for all axes. The corresponding SD of the random (σ) errors were reduced from 3.0 to < 0.8 mm. These small residual errors were achieved with a treatment time extension of <1 minute. Furthermore, the imaging-specific dose was minimal because the MV imaging was obtained with the therapeutic dose and the low dose planar kV images were acquired for only one direction.

In **Chapter 3**, prostate intrafraction motion was assessed by multiple kV and MV imaging of implanted markers during treatment for a large group of prostate patients. Prostate displacements in the sagittal plane increased during the fraction (on average 0.2 ± 0.2 mm/minute). The Observed population systematic intrafraction motion ($\mu_{eff} \pm \Sigma_{eff}$) was 0.9 ± 1.1 mm and 0.6 ± 1.0 mm for the anterior-posterior and inferior-superior directions, respectively. Corresponding random motion (σ_{eff}) was 1.2 mm and 1.1 mm. Mean effective prostate motion in the first 5 fractions predicted for the mean effective displacement in remaining fractions (p<0.001). The systematic (reproducing from fraction to fraction) intrafraction motion can severely impact treatment and therefore requires correction.

A new system for software-controlled highly automated correction of infraction prostate motion, "intrafraction StereoGraphic Targeting" (iSGT) was described and evaluated in **Chapter 4**. intrafraction StereoGraphic Targeting (iSGT) entails MV image acquisitions with the first segment of selected subsequent IMRT beams, followed by remote couch repositioning to correct for intrafraction motion above a pre-defined threshold, prior to delivery of the remainder of the segments. iSGT was implemented by extension of the SGT software to facilitate fast and accurate intrafraction set-up corrections with minimal user interaction. Using iSGT with an action level of 2 mm for intrafraction corrections, effective systematic and random prostate displacements in the sagittal plane could be kept < 0.6 mm and < 0.7 mm, respectively, with addition of < 30 seconds per fraction, if a correction is required.

Chapter 5 presents a study to quantify residual geometric errors and estimate planning margins after marker-based prostate positioning. The deformation errors of the prostate and, in particular, the seminal vesicles relative to intra-prostatic fiducial markers were quantified using non-rigid registration and organ segmentations from repeat computed tomographys (CTs) of 21 prostate patients. The repeat CTs were first rigidly registered on markers to simulate online translation corrections and additionally, rotation corrections. It was found that the largest deformations occurred at the anterior and posterior side of the seminal vesicles with population average standard deviations of 3 mm. Prostate deformation was small with standard deviation of 1 mm. The significantly larger deformation errors for the seminal vesicles present a limitation to achievable margin reduction for prostate radiotherapy including vesicles in the clinical target volume (CTV). Adding marker-based rotational corrections to online translation corrections provided a limited reduction in the estimated planning margins.

In **Chapter 6**, a system for margin evaluation in the presence of all measured errors in particular deformation errors was developed and applied to the case of prostate and entire seminal vesicle irradiation. In the population of patients, a 5-mm margin provided sufficient dosimetric coverage for the prostate. In contrast, an 8-mm SV margin was still insufficient owing to deformations. In agreement with the geometric analysis in **Chapter 5**, addition of three-dimensional rotation corrections was of minor influence for the finally delivered CTV dose, even if the vesicles are part of the CTV.

Chapter 7 provides a discussion of the main findings of this thesis. Other solutions for prostate IGRT are also discussed, paying attention to some key differences compared to the marker-based approached described in this thesis. For the residual errors that cannot be corrected by simple marker-based couch translations, adaptive radiotherapy (ART) offers possible options for accounting for these types of errors. Some future ideas relating to accounting for these residual errors and the extent to which possible adaptive radiation therapy (ART) schemes can be realized in the context of the IGRT scheme in this thesis are also presented.

Samenvatting

Prostaatkanker is de meest voorkomende vorm van kanker en de tweede belangrijkste oorzaak van kanker-gerelateerde sterfgevallen bij mannen op longkanker na [1, 2]. Een van de meest gebruikte behandelingen is EBRT (*External Beam Radiotherapy*, EBRT). Hierbij wordt het doelvolume (target) bestraald terwijl het gezonde weefsel (OAR, organs at risk) zoveel mogelijk ontzien wordt. De behandeling vindt meestal plaats in fracties, waarbij in een periode van 5-6 weken de patiënt dagelijks een deel van de dosis krijgt. Voor een goede behandeling is het belangrijk dat de patiënt (en doelvolume) bij elke fractie zo identiek mogelijk ligt.

In de afgelopen decennia is er een grote vooruitgang geboekt in het EBRT techniek, waardoor het mogelijk is tumoren nauwkeurig te bestralen zonder de gevoelige organen aan een te hoge dosis bloot te stellen. Deze ontwikkelingen hebben ertoe geleid dat er tegenwoordig met een hogere dosis bestraald kan worden dan voorheen, zonder een onacceptabele kans op bijwerkingen. De combinatie van hoge dosissen en de steile dosisgradiënten in de richting de gevoelige organen brengt het risico met zich mee dat de tumor gemist kan worden en dat de gevoelige organen een te hoge dosis kunnen krijgen. Daarom is het van groot belang dat de benodigde voorzorgsmaatregelen genomen worden om hoge precisie van de behandeling te garanderen.

Dit heeft onderzoek gestimuleerd naar beeldvormingstechnieken die in de behandelkamer gebruikt kunnen worden, zoals electronische beeldvormingapparaten (*Electronic Portal Imaging Devices*, EPIDs) en *cone beam computed tomography* (CBCT). Hieruit is beeldgeleide radiotherapie (*Image Guided Radiotherapy*, IGRT) ontstaan.

Voor de klinische implementatie van IGRT technieken is het wenselijk om de werkdruk te verkleinen door verschillende analyses automatisch uit te voeren met behulp van de standaard evaluatieopties van de lineaire versneller.

Het onderzoek beschreven in dit proefschrift is gericht op het ontwikkelen van tijds- en werkdrukefficiënte systemen en methodes voor de positionering van prostaatkankerpatiënten tijdens EBRT gebruik makend van het algemene IGRT raamwerk. Een systeem is ontwikkeld voor dagelijkse interfractie positionering van de patiënt. Later is het uitgebreid naar intrafractie positionering met behulp van beeldvorming van markers geïmplanteerd in de prostaat en software om de positie van behandeltafel, met daarop de patiënt, automatisch aan te passen. De grote voordelen die dit biedt zijn: (1) minimale toename van de duur van de bestralingsfractie; (2) een hoge nauwkeurigheid van de behandeling; (3) minimale toename van de werkdruk door beeldvorming en analyse van de beelden en positionering; (4) de extra

dosis aan de patiënt van de beeldvormingstechnieken is beperkt.

Het tweede doel van dit onderzoek was om de residuele positioneringsfouten te kwantificeren die niet gecorrigeerd kunnen worden door translaties van de behandeltafel, en hiervoor de planningsmarges te bepalen die nodig zijn om voor deze effecten te corrigeren. Het gaat dan met name om rotaties en deformaties van de organen.

Hoofdstuk 1 is een algemene introductie van dit proefschrift, waarin een aantal concepten beschreven worden die specifiek zijn bij de behandeling van porstaatkanker door middel van EBRT. Hierin staan ook de doelstellingen beschreven.

Hoofdstuk 2 beschrijft de ontwikkeling van een volledig automatische en snelle *online* prostaat positionering methode. Deze methode is vervolgens klinisch in gebruik genomen. De patiënt word gepositioneerd door middel van automatische translaties van de behandeltafel op basis van orthogonale kilovolt (kV) of megavolt (MV) beeldvorming van de geïmplanteerde markers. De initiële klinische resultaten van deze methode (*stereoGraphic Targeting*, SGT) worden gepresenteerd samen met fantoom metingen. Met behulp van SGT zijn de standaard deviaties (SD) van de systematische positioneringsfouten (Σ) verkleind van 4 mm naar minder dan 0.5 mm in alle richtingen. De SD van de willekeurige (random) fouten (σ) is afgenomen van 3.0 tot minder dan 0.8 mm. De procedure die benodigd is om deze resultaten te behalen neemt minder dan 1 minuut per fractie in beslag. De extra stralingdosis aan de patiënt als gevolg van de beeldvorming is minimaal omdat bij de MV velden de beeldvorming gedaan word met een deel van de therapeutisch bundels. De planaire kV beelden werden slechts in een richting gemaakt met lage dosissen.

Hoofdstuk 3 beschrijft een studie waarin voor een grote groep prostaatkankerpatiënten de intrafractie beweging van de prostaat is bepaald. Dit word gedaan met behulp van kV en MV beeldvorming van geïmplanteerde markers tijdens de behandeling. De verplaatsing van de prostaat in het sagittale vlak neemt tijdens de behandelfractie toe (gemiddeld 0.2 ± 0.2 mm / minuut). De geobserveerde systematische intrafractiebeweging ($\mu_{eff} \pm \Sigma_{eff}$) was 0.9 ± 1.1 mm en 0.6 ± 1.0 mm voor de anterior-posteriore en de inferior-superiore richting respectievelijk. De corresponderende willekeurige bewegingen (σ_{eff}) waren 1.2 mm en 1.1 mm respectievelijk. De gemiddelde effectieve prostaat beweging tijdens de eerste vijf fracties is voorspellend voor de gemiddelde verplaatsing tijdens de rest van de fracties (p<0.001). De systematische intrafractiebeweging kan een grote impact hebben op de behandeling waarvoor gecorrigeerd moet worden.

Een nieuw systeem voor software-gecontroleerde automatische correctie van intrafractie prostaat beweging (*intrafraction StereoGraphic Targeting*, iSGT), wordt be-

schreven en geëvalueerd in **Hoofdstuk 4**. Bij iSGT wordt een MV beeld gemaakt van de eerste segmenten van geselecteerde Intensiteits Gemoduleerde Radiotherapy (IMRT) velden. Op basis van deze beelden wordt de positie van de behandeltafel aangepast als er een vooraf gedefinieerde drempel overschreden wordt. Daarna pas worden de overgebleven IMRT segmenten afgestraald. iSGT was geïmplementeerd door uitbreiding van de SGT software om snel en nauwkeurige intrafractie set-up correcties uit te voeren met minimale gebruikersinteractie. iSGT met een drempelwaarde van 2 mm voor intrafractie correcties leidt tot systematische en willekeurige prostaat verplaatsingen in het sagittale vlak van minder dan 0.6 mm en minder dan 0.7 mm respectievelijk, ten koste van een verlengde fractieduur van slecht 30 seconden of minder.

Hoofdstuk 5 beschrijft een studie om residuele geometrische fouten te kwantificeren en een schatting te maken van de benodigde marges nadat de positie van de patient op basis van de markers aangepast is. De deformatiefouten van de prostaat, en meer specifiek de zaadblaasjes, ten opzichte van de positie van de markers in de prostaat zijn gekwantificeerd met niet-rigide registratie en orgaan segmentaties van herhaalde CT scans (dat wil zeggen gemaakt tijden de behandeling) van 21 prostaatpatiënten. De CT scans werden eerst rigide geregistreerd met de markers om online translatie- en rotatiecorrecties te simuleren. De grootste deformaties vonden plaats in de anteriore en posteriore richting van de zaadblaasjes. De gemiddelde SD van de populatie was 3 mm. Deformaties van de prostaat waren klein met een SD van 1 mm. De significant grotere deformatiefouten van de zaadblaasjes ten opzichte van de prostaat vormen de beperking voor marge reductie bij de behandeling van prostaatkanker met radiotherapie voor de patiënten bij wie de zaadblaasjes in het te bestralen volume (*Clinical Target Volume*, CTV) opgenomen zijn. Het toevoegen van rotatiecorrecties gebaseerd op markers resulteerde in slechts een beperkte afname van de benodigde planning marges.

Hoofdstuk 6 beschrijft een methode voor margeevaluatie van alle gemeten fouten (specifiek deformatiefouten). De methode was toegepast voor gecombineerde bestralingen van de prostaat en beide zaadblaasjes. Voor de populatie gaf een marge van 5 mm voldoende dosimetrische dekking voor de prostaat. Echter zelfs een marge van 8 mm was niet voldoende voor de zaadblaasjes, ten gevolge van de grote deformaties ten opzichte van de markers in de prostaat. In overeenstemming met Hoofdstuk 5 had een rotatiecorrectie weinig toegevoegde waarde voor de dosis aan het CTV. Ook als de zaadblaasjes onderdeel uitmaakten van het CTV.

In **Hoofdstuk 7** worden de belangrijkste bevinden van dit proefschrift bediscussieerd. Andere methoden voor prostaat IGRT worden besproken met speciale

aandacht voor methoden die geen gebruik maken van markers. Voor de residuele fouten die niet gecorrigeerd kunnen worden met tafelverschuivingen, kan adaptieve radiotherapie (*Adaptive Radiotherapy*, ART) voor een deel uitkomst bieden. Dit wordt beschreven aan de hand van een aantal toekomstperspectieven.

References

[1] Ferlay, J; Shin, HR; Bray, F; Forman, D; Mathers, C; Parkin, DM. "Estimates of worldwide burden of cancer in 2008: GLOBOCAN 2008." eng. *Int J Cancer* (2010).

[2] Hsing, AW; Tsao, L; Devesa, SS. "International trends and patterns of prostate cancer incidence and mortality." eng. *Int J Cancer* 85.1 (2000), pp. 60–67.

[3] Jemal, A; Siegel, R; Xu, J; Ward, E. "Cancer statistics, 2010." eng. *CA Cancer J Clin* 60.5 (2010), pp. 277–300.

[4] Biagioli, MC; Hoffe, SE. "Emerging technologies in prostate cancer radiation therapy: improving the therapeutic window." eng. *Cancer Control* 17.4 (2010), pp. 223–232.

[5] Mackie, TR; Holmes, T; Swerdloff, S; Reckwerdt, P; Deasy, JO; Yang, J; Paliwal, B; Kinsella, T. "Tomotherapy: a new concept for the delivery of dynamic conformal radiotherapy." eng. *Med Phys* 20.6 (1993), pp. 1709–1719.

[6] Sterzing, F; Schubert, K; Sroka-Perez, G; Kalz, J; Debus, J; Herfarth, K. "Helical tomotherapy. Experiences of the first 150 patients in Heidelberg." eng. *Strahlenther Onkol* 184.1 (2008), pp. 8–14.

[7] Yu, CX. "Intensity-modulated arc therapy with dynamic multileaf collimation: an alternative to tomotherapy." eng. *Phys Med Biol* 40.9 (1995), pp. 1435–1449.

[8] Mangar, SA; Huddart, RA; Parker, CC; Dearnaley, DP; Khoo, VS; Horwich, A. "Technological advances in radiotherapy for the treatment of localised prostate cancer." eng. *Eur J Cancer* 41.6 (2005), pp. 908–921.

[9] Khoo, VS. "Radiotherapeutic techniques for prostate cancer, dose escalation and brachytherapy." eng. *Clin Oncol (R Coll Radiol)* 17.7 (2005), pp. 560–571.

[10] Ahmed, HU; Pendse, D; Illing, R; Allen, C; Meulen, JH van der; Emberton, M. "Will focal therapy become a standard of care for men with localized prostate cancer?" *Nat Clin Prac Oncol* 4.11 (Nov. 2007), pp. 632–642.

[11] Peeters, STH; Heemsbergen, WD; Koper, PCM; Putten, WLJ van; Slot, A; Dielwart, MFH; Bonfrer, JMG; Incrocci, L; Lebesque, JV. "Dose-response in radiotherapy for localized prostate cancer: results of the Dutch multicenter randomized phase III trial comparing 68 Gy of radiotherapy with 78 Gy." eng. *J Clin Oncol* 24.13 (2006), pp. 1990–1996.

[12] Pollack, A; Zagars, GK; Starkschall, G; Antolak, JA; Lee, JJ; Huang, E; Eschenbach, AC von; Kuban, DA; Rosen, I. "Prostate cancer radiation dose response: results of the M. D. Anderson phase III randomized trial." eng. *Int J Radiat Oncol Biol Phys* 53.5 (2002), pp. 1097–1105.

[13] Zelefsky, MJ; Fuks, Z; Happersett, L; Lee, HJ; Ling, CC; Burman, CM; Hunt, M; Wolfe, T; Venkatraman, ES; Jackson, A; Skwarchuk, M; Leibel, SA. "Clinical experience with intensity modulated radiation therapy (IMRT) in prostate cancer." eng. *Radiother Oncol* 55.3 (2000), pp. 241–249.

[14] Zelefsky, MJ; Leibel, SA; Gaudin, PB; Kutcher, GJ; Fleshner, NE; Venkatramen, ES; Reuter, VE; Fair, WR; Ling, CC; Fuks, Z. "Dose escalation with three-dimensional conformal radiation therapy affects the outcome in prostate cancer." eng. *Int J Radiat Oncol Biol Phys* 41.3 (1998), pp. 491–500.

[15] Al-Mamgani, A; Putten, WLJ van; Heemsbergen, WD; Leenders, GJLH van; Slot, A; Dielwart, MFH; Incrocci, L; Lebesque, JV. "Update of Dutch multicenter dose-escalation trial of radiotherapy for localized prostate cancer." eng. *Int J Radiat Oncol Biol Phys* 72.4 (2008), pp. 980–988.

[16] Wielen, GJ van der; Mulhall, JP; Incrocci, L. "Erectile dysfunction after radiotherapy for prostate cancer and radiation dose to the penile structures: a critical review." eng. *Radiother Oncol* 84.2 (2007), pp. 107–113.

[17] Wielen, GJ van der; Putten, WLJ van; Incrocci, L. "Sexual function after three-dimensional conformal radiotherapy for prostate cancer: results from a dose-escalation trial." eng. *Int J Radiat Oncol Biol Phys* 68.2 (2007), pp. 479–484.

[18] Wielen, GJ van der. "Erectile dysfunction after external beam radiotherapy for prostate cancer: Can it be prevented?: Gerard Johan van der Wielen". English. http://opc-prd.ubib.eur.nl:8080/DB=2/PPN?PPN=323551459/. PhD thesis. Rotterdam: Erasmus University, 2010.

[19] Bayman, NA; Wylie, JP. "When should the seminal vesicles be included in the target volume in prostate radiotherapy?" eng. *Clin Oncol (R Coll Radiol)* 19.5 (2007), pp. 302–307.

[20] Kestin, LL; Goldstein, NS; Vicini, FA; Yan, D; Korman, HJ; Martinez, AA. "Treatment of prostate cancer with radiotherapy: should the entire seminal vesicles be included in the clinical target volume?" *International journal of radiation oncology, biology, physics* 54.3 (Nov. 2002), pp. 686–697.

[21] Brenner, DJ; Hall, EJ. "Fractionation and protraction for radiotherapy of prostate carcinoma." eng. *Int J Radiat Oncol Biol Phys* 43.5 (1999), pp. 1095–1101.

[22] "Prescribing, Recording, and Reporting Photon-Beam Intensity-Modulated Radiation Therapy (IMRT)". *Journal of the ICRU* 10.1 (2010), NP.

[23] "ICRU Report 62. Prescribing, recording and reporting photon beam therapy (supplement to ICRU Report 50)" (1999). Bethseda, MD.

[24] "ICRU Report 50. Prescribing, Recording, and Reporting Photon Beam Therapy" (1993). Bethseda, MD.

[25] Herk, M van; Remeijer, P; Rasch, C; Lebesque, JV. "The probability of correct target dosage: dose-population histograms for deriving treatment margins in radiotherapy." eng. *Int J Radiat Oncol Biol Phys* 47.4 (2000), pp. 1121–1135.

[26] Stroom, JC; Boer, HC de; Huizenga, H; Visser, AG. "Inclusion of geometrical uncertainties in radiotherapy treatment planning by means of coverage probability." eng. *Int J Radiat Oncol Biol Phys* 43.4 (1999), pp. 905–919.

[27] Welsh, JS; Berta, C; Borzillary, S; Sam, C; Shickell, D; Nobile, L; Greenberg, M; Weiss, S; Detorie, N. "Fiducial markers implanted during prostate brachytherapy for guiding conformal external beam radiation therapy." eng. *Technol Cancer Res Treat* 3.4 (2004), pp. 359–364.

[28] Schiffner, DC; Gottschalk, AR; Lometti, M; Aubin, M; Pouliot, J; Speight, J; Hsu, IC; Shinohara, K; Roach, M. "Daily electronic portal imaging of implanted gold seed fiducials in patients undergoing radiotherapy after radical prostatectomy." eng. *Int J Radiat Oncol Biol Phys* 67.2 (2007), pp. 610–619.

[29] Poggi, MM; Gant, DA; Sewchand, W; Warlick, WB. "Marker seed migration in prostate localization." eng. *Int J Radiat Oncol Biol Phys* 56.5 (2003), pp. 1248–1251.

[30] Beaulieu, L; Girouard, LM; Aubin, S; Aubry, JF; Brouard, L; Roy-Lacroix, L; Dumont, J; Tremblay, D; Laverdière, J; Vigneault, E. "Performing daily prostate targeting with a standard V-EPID and an automated radio-opaque marker detection algorithm." eng. *Radiother Oncol* 73.1 (2004), pp. 61–64.

[31] Aubry, JF; Beaulieu, L; Girouard, LM; Aubin, S; Tremblay, D; Laverdière, J; Vigneault, E. "Measurements of intrafraction motion and interfraction and intrafraction rotation of prostate by three-dimensional analysis of daily portal imaging with radiopaque markers." eng. *Int J Radiat Oncol Biol Phys* 60.1 (2004), pp. 30–39.

[32] Sorcini, B; Tilikidis, A. "Clinical application of image-guided radiotherapy, IGRT (on the Varian OBI platform)." eng. *Cancer Radiother* 10.5 (2006), pp. 252–257.

[33] Jaffray, D; Siewerdsen, J; Wong, J; Martinez, A. "Flat-panel cone-beam computed tomography for image-guided radiation therapy". *International Journal of Radiation Oncology Biology Physics* 53.5 (2002). cited By (since 1996) 430, pp. 1337–1349.

[34] Shalev, S. "Treatment verification using digital imaging". *Radiation Therapy Physics* (1995). Cited By (since 1996): 15 Export Date: 8 March 2011 Source: Scopus, pp. 155–173.

[35] Heemsbergen, WD; Hoogeman, MS; Witte, MG; Peeters, STH; Incrocci, L; Lebesque, JV. "Increased Risk of Biochemical and Clinical Failure for Prostate Patients with a Large Rectum at Radiotherapy Planning: Results from the Dutch Trial of 68 GY Versus 78 Gy". *International Journal of Radiation Oncology Biology Physics* 67.5 (2007). Cited By (since 1996): 38 Export Date: 8 March 2011 Source: Scopus, pp. 1418–1424.

[36] De Crevoisier, R; Tucker, SL; Dong, L; Mohan, R; Cheung, R; Cox, JD; Kuban, DA. "Increased risk of biochemical and local failure in patients with distended rectum on the planning CT for prostate cancer radiotherapy". *International Journal of Radiation Oncology Biology Physics* 62.4 (2005). Cited By (since 1996): 132 Export Date: 8 March 2011 Source: Scopus, pp. 965–973.

[37] Létourneau, D; Martinez, AA; Lockman, D; Yan, D; Vargas, C; Ivaldi, G; Wong, J. "Assessment of residual error for online cone-beam CT-guided treatment of prostate cancer patients." eng. *Int J Radiat Oncol Biol Phys* 62.4 (2005), pp. 1239–1246.

[38] Litzenberg, D; Dawson, LA; Sandler, H; Sanda, MG; McShan, DL; Ten Haken, RK; Lam, KL; Brock, KK; Balter, JM. "Daily prostate targeting using implanted radiopaque markers". *International Journal of Radiation Oncology Biology Physics* 52.3 (2002). Cited By (since 1996): 110 Export Date: 8 March 2011 Source: Scopus, pp. 699–703.

[39] De Boer, HCJ; Van Os, MJH; Jansen, PP; Heijmen, BJM. "Application of the No Action Level (NAL) protocol to correct for prostate motion based on electronic portal imaging of implanted markers". *International Journal of Radiation Oncology Biology Physics* 61.4 (2005). Cited By (since 1996): 49 Export Date: 8 March 2011 Source: Scopus, pp. 969–983.

[40] Chung, PWM; Haycocks, T; Brown, T; Cambridge, Z; Kelly, V; Alasti, H; Jaffray, DA; Catton, CN. "On-line aSi portal imaging of implanted fiducial markers for the reduction of interfraction error during conformal radiotherapy of prostate carcinoma". *International Journal of Radiation Oncology Biology Physics*

60.1 (2004). Cited By (since 1996): 71 Export Date: 8 March 2011 Source: Scopus, pp. 329–334.

[41] Reed, DR; Wallner, K; Ford, E; Mueller, A; Merrick, G; Maki, J; Sutlief, S; Butler, W. "Effect of post-implant edema on prostate brachytherapy treatment margins". *International Journal of Radiation Oncology Biology Physics* 63.5 (2005). Cited By (since 1996): 17 Export Date: 8 March 2011 Source: Scopus, pp. 1469–1473.

[42] Vieira, SC; Dirkx, MLP; Heijmen, BJM; De Boer, HCJ. "SIFT: A method to verify the IMRT fluence delivered during patient treatment using an electronic portal imaging device". *International Journal of Radiation Oncology Biology Physics* 60.3 (2004). Cited By (since 1996): 17 Export Date: 8 March 2011 Source: Scopus, pp. 981–993.

[43] Sharpe, MB; Moseley, DJ; Purdie, TG; Islam, M; Siewerdsen, JH; Jaffray, DA. "The stability of mechanical calibration for a kV cone beam computed tomography system integrated with linear accelerator." eng. *Med Phys* 33.1 (2006), pp. 136–144.

[44] Bijhold, J; Gilhuijs, KGA; Van Herk, M; Meertens, H. "Radiation field edge detection in portal images". *Physics in Medicine and Biology* 36.12 (1991). Cited By (since 1996): 38 Export Date: 8 March 2011 Source: Scopus, pp. 1705–1710.

[45] Nederveen, A; Lagendijk, J; Hofman, P. "Detection of fiducial gold markers for automatic on-line megavoltage position verification using a marker extraction kernel (MEK)". *International Journal of Radiation Oncology Biology Physics* 47.5 (2000). Cited By (since 1996): 55 Export Date: 8 March 2011 Source: Scopus, pp. 1435–1442.

[46] Gilhuijs, KGA; Van Herk, M. "Automatic on-line inspection of patient setup in radiation therapy using digital portal images". *Medical Physics* 20.3 (1993). Cited By (since 1996): 71 Export Date: 8 March 2011 Source: Scopus, pp. 667–677.

[47] Murphy, MJ. "Fiducial-based targeting accuracy for external-beam radiotherapy". *Medical Physics* 29.3 (2002). Cited By (since 1996): 46 Export Date: 8 March 2011 Source: Scopus, pp. 334–344.

[48] Verellen, D; Soete, G; Linthout, N; Tournel, K; Storme, G. "Optimal control of set-up margins and internal margins for intra- and extracranial radiotherapy using stereoscopic kilovoltage imaging". *Cancer/Radiotherapie* 10.5 (2006). Cited By (since 1996): 21 Export Date: 8 March 2011 Source: Scopus, pp. 235–244.

[49] Soete, G; Cock, MD; Verellen, D; Michielsen, D; Keuppens, F; Storme, G. "X-ray-assisted positioning of patients treated by conformal arc radiotherapy for prostate cancer: Comparison of setup accuracy using implanted markers versus bony structures". *International Journal of Radiation Oncology*Biology*Physics* 67.3 (Mar. 2007), pp. 823–827.

[50] Fuller, CD; Thomas, CR; Schwartz, S; Golden, N; Ting, J; Wong, A; Erdogmus, D; Scarbrough, TJ. "Method comparison of ultrasound and kilovoltage x-ray fiducial marker imaging for prostate radiotherapy targeting". *Physics in Medicine and Biology* 51.19 (2006). Cited By (since 1996): 13 Export Date: 8 March 2011 Source: Scopus Art. No.: 016, pp. 4981–4993.

[51] Yan, D; Lockman, D; Brabbins, D; Tyburski, L; Martinez, A. "An off-line strategy for constructing a patient-specific planning target volume in adaptive treatment process for prostate cancer". *International Journal of Radiation Oncology Biology Physics* 48.1 (2000). Cited By (since 1996): 167 Export Date: 8 March 2011 Source: Scopus, pp. 289–302.

[52] Nuver, TT; Hoogeman, MS; Remeijer, P; Herk, M van; Lebesque, JV. "An Adaptive Off-Line Procedure for Radiotherapy of Prostate Cancer". *International Journal of Radiation Oncology Biology Physics* 67.5 (2007). Cited By (since 1996): 27 Export Date: 8 March 2011 Source: Scopus, pp. 1559–1567.

[53] Zijtveld, M van; Dirkx, MLP; Boer, HCJ de; Heijmen, BJM. "Dosimetric pre-treatment verification of IMRT using an EPID; clinical experience". *Radiotherapy and Oncology* 81.2 (2006). Cited By (since 1996): 30 Export Date: 8 March 2011 Source: Scopus, pp. 168–175.

[54] Smitsmans, MHP; De Bois, J; Sonke, JJ; Betgen, A; Zijp, LJ; Jaffray, DA; Lebesque, JV; Van Herk, M. "Automatic prostate localization on cone-beam CT scans for high precision image-guided radiotherapy". *International Journal of Radiation Oncology Biology Physics* 63.4 (2005). Cited By (since 1996): 94 Export Date: 8 March 2011 Source: Scopus, pp. 975–984.

[55] Fowler, J; Chappell, R; Ritter, M. "Is α/β for prostate tumors really low?" eng. *Int J Radiat Oncol Biol Phys* 50.4 (2001), pp. 1021–1031.

[56] Brenner, DJ; Martinez, AA; Edmundson, GK; Mitchell, C; Thames, HD; Armour, EP. "Direct evidence that prostate tumors show high sensitivity to fractionation (low α/β ratio), similar to late-responding normal tissue". *International Journal of Radiation Oncology Biology Physics* 52.1 (2002). Cited By (since 1996): 240 Export Date: 8 March 2011 Source: Scopus, pp. 6–13.

[57] Heide, UA van der; Kotte, ANTJ; Dehnad, H; Hofman, P; Lagenijk, JJW; Vulpen, M van. "Analysis of fiducial marker-based position verification in the external beam radiotherapy of patients with prostate cancer". *Radiotherapy and Oncology* 82.1 (2007). Cited By (since 1996): 47 Export Date: 8 March 2011 Source: Scopus, pp. 38–45.

[58] Boer, HCJ de; Heijmen, BJM. "eNAL: An Extension of the NAL Setup Correction Protocol for Effective Use of Weekly Follow-up Measurements". *International Journal of Radiation Oncology Biology Physics* 67.5 (2007). Cited By (since 1996): 10 Export Date: 8 March 2011 Source: Scopus, pp. 1586–1595.

[59] Hoogeman, MS; Van Herk, M; De Bois, J; Lebesque, JV. "Strategies to reduce the systematic error due to tumor and rectum motion in radiotherapy of prostate cancer". *Radiotherapy and Oncology* 74.2 (2005). Cited By (since 1996): 54 Export Date: 8 March 2011 Source: Scopus, pp. 177–185.

[60] Dehnad, H; Nederveen, AJ; Van Der Heide, UA; Van Moorselaar, RJA; Hofman, P; Lagendijk, JJW. "Clinical feasibility study for the use of implanted gold seeds in the prostate as reliable positioning markers during megavoltage irradiation". *Radiotherapy and Oncology* 67.3 (2003). Cited By (since 1996): 89 Export Date: 8 March 2011 Source: Scopus, pp. 295–302.

[61] Steenbakkers, RJHM; Duppen, JC; Betgen, A; Lotz, HT; Remeijer, P; Fitton, I; Nowak, PJCM; Van Herk, M; Rasch, CRN. "Impact of knee support and shape of tabletop on rectum and prostate position". *International Journal of Radiation Oncology Biology Physics* 60.5 (2004). Cited By (since 1996): 9 Export Date: 8 March 2011 Source: Scopus, pp. 1364–1372.

[62] Kupelian, PA; Willoughby, TR; Meeks, SL; Forbes, A; Wagner, T; Maach, M; Langen, KM. "Intraprostatic fiducials for localization of the prostate gland: Monitoring intermarker distances during radiation therapy to test for marker stability". *International Journal of Radiation Oncology Biology Physics* 62.5 (2005). Cited By (since 1996): 53 Export Date: 8 March 2011 Source: Scopus, pp. 1291–1296.

[63] Litzenberg, DW; Balter, JM; Hadley, SW; Sandler, HM; Willoughby, TR; Kupelian, PA; Levine, L. "Influence of intrafraction motion on margins for prostate radiotherapy". *International Journal of Radiation Oncology*Biology*Physics* 65.2 (June 2006), pp. 548–553.

[64] Ghilezan, MJ; Jaffray, DA; Siewerdsen, JH; Van Herk, M; Shetty, A; Sharpe, MB; Jafri, SZ; Vicini, FA; Matter, RC; Brabbins, DS; Martinez, AA. "Prostate gland motion assessed with cine-magnetic resonance imaging (cine-MRI)".

International Journal of Radiation Oncology Biology Physics 62.2 (2005). Cited By (since 1996): 114 Export Date: 8 March 2011 Source: Scopus, pp. 406–417.

[65] Van Herk, M. "Errors and Margins in Radiotherapy". *Seminars in Radiation Oncology* 14.1 (2004). Cited By (since 1996): 248 Export Date: 8 March 2011 Source: Scopus, pp. 52–64.

[66] Smitsmans, MHP; Wolthaus, JWH; Artignan, X; De Bois, J; Jaffray, DA; Lebesque, JV; Van Herk, M. "Automatic localization of the prostate for on-line or off-line image-guided radiotherapy". *International Journal of Radiation Oncology Biology Physics* 60.2 (2004). Cited By (since 1996): 44 Export Date: 8 March 2011 Source: Scopus, pp. 623–635.

[67] Smith, WL; Lewis, C; Bauman, G; Rodrigues, G; D'Souza, D; Ash, R; Ho, D; Venkatesan, V; Downey, D; Fenster, A. "Prostate volume contouring: A 3D analysis of segmentation using 3DTRUS, CT, and MR". *International Journal of Radiation Oncology Biology Physics* 67.4 (2007). Cited By (since 1996): 20 Export Date: 8 March 2011 Source: Scopus, pp. 1238–1247.

[68] Hoffelt, SC; Marshall, LM; Garzotto, M; Hung, A; Holland, J; Beer, TM. "A comparison of CT scan to transrectal ultrasound-measured prostate volume in untreated prostate cancer". *International Journal of Radiation Oncology Biology Physics* 57.1 (2003). Cited By (since 1996): 31 Export Date: 8 March 2011 Source: Scopus, pp. 29–32.

[69] Mutanga, TF; Boer, HCJ de; Wielen, GJ van der; Wentzler, D; Barnhoorn, J; Incrocci, L; Heijmen, BJM. "Stereographic targeting in prostate radiotherapy: speed and precision by daily automatic positioning corrections using kilovoltage/megavoltage image pairs." eng. *Int J Radiat Oncol Biol Phys* 71.4 (2008), pp. 1074–1083.

[70] Nederveen, AJ; Heide, UA van der; Dehnad, H; Moorselaar, RJA van; Hofman, P; Lagendijk, JJW. "Measurements and clinical consequences of prostate motion during a radiotherapy fraction." eng. *Int J Radiat Oncol Biol Phys* 53.1 (2002), pp. 206–214.

[71] Huang, E; Dong, L; Chandra, A; Kuban, DA; Rosen, II; Evans, A; Pollack, A. "Intrafraction prostate motion during IMRT for prostate cancer." eng. *Int J Radiat Oncol Biol Phys* 53.2 (2002), pp. 261–268.

[72] Willoughby, TR; Kupelian, PA; Pouliot, J; Shinohara, K; Aubin, M; Roach, M; Skrumeda, LL; Balter, JM; Litzenberg, DW; Hadley, SW; Wei, JT; Sandler, HM. "Target localization and real-time tracking using the Calypso 4D localization system in patients with localized prostate cancer." eng. *Int J Radiat Oncol Biol Phys* 65.2 (2006), pp. 528–534.

[73] Adamson, J; Wu, Q. "Prostate intrafraction motion assessed by simultaneous kilovoltage fluoroscopy at megavoltage delivery I: clinical observations and pattern analysis." eng. *Int J Radiat Oncol Biol Phys* 78.5 (2010), pp. 1563–1570.

[74] Boda-Heggemann, J; Köhler, FM; Wertz, H; Ehmann, M; Hermann, B; Riesenacker, N; Küpper, B; Lohr, F; Wenz, F. "Intrafraction motion of the prostate during an IMRT session: a fiducial-based 3D measurement with Cone-beam CT." eng. *Radiat Oncol* 3 (2008), p. 37.

[75] Langen, KM; Willoughby, TR; Meeks, SL; Santhanam, A; Cunningham, A; Levine, L; Kupelian, PA. "Observations on real-time prostate gland motion using electromagnetic tracking." eng. *Int J Radiat Oncol Biol Phys* 71.4 (2008), pp. 1084–1090.

[76] Malinowski, KT; Noel, C; Roy, M; Willoughby, T; Djemi, T; Jani, S; Solberg, T; Liu, D; Levine, L; Parikh, PJ. "Efficient use of continuous, real-time prostate localization." eng. *Phys Med Biol* 53.18 (2008), pp. 4959–4970.

[77] Kotte, AN; Hofman, P; Lagendijk, JJ; Vulpen, M van; Heide, UA van der. "Intrafraction Motion of the Prostate During External-Beam Radiation Therapy: Analysis of 427 Patients with Implanted Fiducial Markers". *International Journal of Radiation Oncology*Biology*Physics* 69.2 (Oct. 2007), pp. 419–425.

[78] Enmark, M; Korreman, S; Nyström, H. "IGRT of prostate cancer; is the margin reduction gained from daily IG time-dependent?" eng. *Acta Oncol* 45.7 (2006), pp. 907–914.

[79] Noel, C; Parikh, PJ; Roy, M; Kupelian, P; Mahadevan, A; Weinstein, G; Enke, C; Flores, N; Beyer, D; Levine, L. "Prediction of intrafraction prostate motion: accuracy of pre- and post-treatment imaging and intermittent imaging." eng. *Int J Radiat Oncol Biol Phys* 73.3 (2009), pp. 692–698.

[80] Li, JS; Jin, L; Pollack, A; Horwitz, EM; Buyyounouski, MK; Price, RA; Ma, CM. "Gains from real-time tracking of prostate motion during external beam radiation therapy." eng. *Int J Radiat Oncol Biol Phys* 75.5 (2009), pp. 1613–1620.

[81] Mah, D; Freedman, G; Milestone, B; Hanlon, A; Palacio, E; Richardson, T; Movsas, B; Mitra, R; Horwitz, E; Hanks, GE. "Measurement of intrafractional prostate motion using magnetic resonance imaging." eng. *Int J Radiat Oncol Biol Phys* 54.2 (2002), pp. 568–575.

[82] Padhani, AR; Khoo, VS; Suckling, J; Husband, JE; Leach, MO; Dearnaley, DP. "Evaluating the effect of rectal distension and rectal movement on prostate gland position using cine MRI." eng. *Int J Radiat Oncol Biol Phys* 44.3 (1999), pp. 525–533.

[83] Rosenthal, SA; Roach, M; Goldsmith, BJ; Doggett, EC; Pickett, B; Yuo, HS; Soffen, EM; Stern, RL; Ryu, JK. "Immobilization improves the reproducibility of patient positioning during six-field conformal radiation therapy for prostate carcinoma." eng. *Int J Radiat Oncol Biol Phys* 27.4 (1993), pp. 921–926.

[84] Soffen, EM; Hanks, GE; Hwang, CC; Chu, JC. "Conformal static field therapy for low volume low grade prostate cancer with rigid immobilization." eng. *Int J Radiat Oncol Biol Phys* 20.1 (1991), pp. 141–146.

[85] Nichol, AM; Warde, PR; Lockwood, GA; Kirilova, AK; Bayley, A; Bristow, R; Crook, J; Gospodarowicz, M; McLean, M; Milosevic, M; Rosewall, T; Jaffray, DA; Catton, CN. "A cinematic magnetic resonance imaging study of milk of magnesia laxative and an antiflatulent diet to reduce intrafraction prostate motion." eng. *Int J Radiat Oncol Biol Phys* 77.4 (2010), pp. 1072–1078.

[86] Wielen, GJ van der; Mutanga, TF; Incrocci, L; Kirkels, WJ; Osorio, EMV; Hoogeman, MS; Heijmen, BJM; Boer, HCJ de. "Deformation of prostate and seminal vesicles relative to intraprostatic fiducial markers." eng. *Int J Radiat Oncol Biol Phys* 72.5 (2008), 1604–1611.e3.

[87] Mutanga, TF; Boer, HCJ de; Wielen, GJ van der; Hoogeman, MS; Incrocci, L; Heijmen, BJM. "Margin Evaluation in the Presence of Deformation, Rotation, and Translation in Prostate and Entire Seminal Vesicle Irradiation with Daily Marker-Based Setup Corrections." eng. *Int J Radiat Oncol Biol Phys* (2010).

[88] Mutanga, TF; Boer., HD; Hoogeman, M; Wielen, GJ van der; Incrocci, L; Heijmen, B. "Radiobiological Evaluation Of The Impact Of Organ Deformation, Rotation And Residue Positioning Errors In Prostate And Seminal Vesicle Irradiation". *Radiotherapy and Oncology* 92.Supplement 1 (2009). Abstract book: 10th BIENNIAL ESTRO CONFERENCE ON PHYSICS AND RADIATION TECHNOLOGY FOR CLINICAL RADIOTHERAPY, 30 Aug - 3 Sep 2009, Maastricht, Netherlands, S118.

[89] Kupelian, PA; Langen, KM; Zeidan, OA; Meeks, SL; Willoughby, TR; Wagner, TH; Jeswani, S; Ruchala, KJ; Haimerl, J; Olivera, GH. "Daily variations in delivered doses in patients treated with radiotherapy for localized prostate cancer." eng. *Int J Radiat Oncol Biol Phys* 66.3 (2006), pp. 876–882.

[90] Mutanga, TF; Boer, HCJ de; Rajan, V; Dirkx, MLP; Incrocci, L; Heijmen, BJM. "Day-to-day reproducibility of prostate intrafraction motion assessed by multiple kV and MV imaging of implanted markers during treatment". eng. *Int J Radiat Oncol Biol Phys* (2011). Submitted, ROB-S-10-02414 (1).

[91] Adamson, J; Wu, Q. "Prostate intrafraction motion assessed by simultaneous kV fluoroscopy at MV delivery II: adaptive strategies." eng. *Int J Radiat Oncol Biol Phys* 78.5 (2010), pp. 1323–1330.

[92] Su, Z; Zhang, L; Murphy, M; Williamson, J. "Analysis of Prostate Patient Setup and Tracking Data: Potential Intervention Strategies." eng. *Int J Radiat Oncol Biol Phys* (2010).

[93] Dong, L; Boyer, AL. "An objective method for evaluating electronic portal imaging devices." eng. *Med Phys* 21.6 (1994), pp. 755–760.

[94] Rose, A. *Vision: Human and Electronic*. New York: Plenum, 1974.

[95] Boer, J de; Barnhoorn, J; Heijmen, B. "Ranking EPID image quality: standard methods and their clinical relevance". *Radiotherapy and Oncology* 73.Supplement 1 (2004), S139–S139.

[96] Kron, T; Thomas, J; Fox, C; Thompson, A; Owen, R; Herschtal, A; Haworth, A; Tai, KH; Foroudi, F. "Intra-fraction prostate displacement in radiotherapy estimated from pre- and post-treatment imaging of patients with implanted fiducial markers." eng. *Radiother Oncol* 95.2 (2010), pp. 191–197.

[97] Jemal, A; Siegel, R; Ward, E; Murray, T; Xu, J; Thun, MJ. "Cancer statistics, 2007." eng. *CA Cancer J Clin* 57.1 (2007), pp. 43–66.

[98] Zelefsky, MJ; Chan, H; Hunt, M; Yamada, Y; Shippy, AM; Amols, H. "Long-term outcome of high dose intensity modulated radiation therapy for patients with clinically localized prostate cancer." eng. *J Urol* 176.4 Pt 1 (2006), pp. 1415–1419.

[99] Dearnaley, DP; Hall, E; Lawrence, D; Huddart, RA; Eeles, R; Nutting, CM; Gadd, J; Warrington, A; Bidmead, M; Horwich, A. "Phase III pilot study of dose escalation using conformal radiotherapy in prostate cancer: PSA control and side effects." eng. *Br J Cancer* 92.3 (2005), pp. 488–498.

[100] Deurloo, KEI; Steenbakkers, RJHM; Zijp, LJ; Bois, JA de; Nowak, PJCM; Rasch, CRN; Herk, M van. "Quantification of shape variation of prostate and seminal vesicles during external beam radiotherapy." eng. *Int J Radiat Oncol Biol Phys* 61.1 (2005), pp. 228–238.

[101] Chui, H; Rangarajan, A. "A new point matching algorithm for non-rigid registration". *Comput. Vis. Image Underst.* 89 (2-3 2003), pp. 114–141.

[102] Osorio, EMV; Hoogeman, MS; Al-Mamgani, A; Teguh, DN; Levendag, PC; Heijmen, BJM. "Local anatomic changes in parotid and submandibular glands during radiotherapy for oropharynx cancer and correlation with dose, studied in detail with nonrigid registration." eng. *Int J Radiat Oncol Biol Phys* 70.3 (2008), pp. 875–882.

[103] Vásquez Osorio, E; Hoogeman, M; Al-Mamgani, A; Teguh, D; Levendag, P; Heijmen, B. "Non-rigid point matching and its application in Radiotherapy". *ICCR: Proceedings of the XVth International Conference on the Use of Computers in Radiation Therapy.* Vol. 2. 2007, pp. 413–417.

[104] Bijhold, J; Lebesque, JV; Hart, AA; Vijlbrief, RE. "Maximizing setup accuracy using portal images as applied to a conformal boost technique for prostatic cancer." eng. *Radiother Oncol* 24.4 (1992), pp. 261–271.

[105] Meijer, GJ; Klerk, J de; Bzdusek, K; Berg, HA van den; Janssen, R; Kaus, MR; Rodrigus, P; Toorn, PP van der. "What CTV-to-PTV margins should be applied for prostate irradiation? Four-dimensional quantitative assessment using model-based deformable image registration techniques." eng. *Int J Radiat Oncol Biol Phys* 72.5 (2008), pp. 1416–1425.

[106] Stroom, JC; Heijmen, BJM. "Geometrical uncertainties, radiotherapy planning margins, and the ICRU-62 report." eng. *Radiother Oncol* 64.1 (2002), pp. 75–83.

[107] Song, W; Schaly, B; Bauman, G; Battista, J; Dyk, JV. "Image-guided adaptive radiation therapy (IGART): Radiobiological and dose escalation considerations for localized carcinoma of the prostate." eng. *Med Phys* 32.7 (2005), pp. 2193–2203.

[108] Boer, HC de; Heijmen, BJ. "A protocol for the reduction of systematic patient setup errors with minimal portal imaging workload." eng. *Int J Radiat Oncol Biol Phys* 50.5 (2001), pp. 1350–1365.

[109] Stroom, JC; Koper, PC; Korevaar, GA; Os, M van; Janssen, M; Boer, HC de; Levendag, PC; Heijmen, BJ. "Internal organ motion in prostate cancer patients treated in prone and supine treatment position." eng. *Radiother Oncol* 51.3 (1999), pp. 237–248.

[110] Rasch, C; Remeijer, P; Koper, PC; Meijer, GJ; Stroom, JC; Herk, M van; Lebesque, JV. "Comparison of prostate cancer treatment in two institutions: a quality control study." eng. *Int J Radiat Oncol Biol Phys* 45.4 (1999), pp. 1055–1062.

[111] Peeters, STH; Heemsbergen, WD; Putten, WLJ van; Slot, A; Tabak, H; Mens, JW; Lebesque, JV; Koper, PCM. "Acute and late complications after radiotherapy for prostate cancer: results of a multicenter randomized trial comparing 68 Gy to 78 Gy." eng. *Int J Radiat Oncol Biol Phys* 61.4 (2005), pp. 1019–1034.

[112] Deasy, JO; Blanco, AI; Clark, VH. "CERR: a computational environment for radiotherapy research." eng. *Med Phys* 30.5 (2003), pp. 979–985.

[113] Os, M van; Dirkx, M; Rajan, V; Barnhoorn, J; Heijmen, B; Boer, HD. "Online Correction for Intrafraction Motion in Prostate Patients with Fiducial Markers". *Radiotherapy and Oncology* 92.Supplement 1 (2009). Poster discussion: 10th BIENNIAL ESTRO CONFERENCE ON PHYSICS AND RADIATION TECHNOLOGY FOR CLINICAL RADIOTHERAPY, 30 Aug–3 Sep 2009, Maastricht, Netherlands, S177.

[114] Osorio, EMV; Hoogeman, MS; Bondar, L; Levendag, PC; Heijmen, BJM. "A novel flexible framework with automatic feature correspondence optimization for nonrigid registration in radiotherapy." eng. *Med Phys* 36.7 (2009), pp. 2848–2859.

[115] Boersma, LJ; Brink, M van den; Bruce, AM; Shouman, T; Gras, L; Velde, A te; Lebesque, JV. "Estimation of the incidence of late bladder and rectum complications after high-dose (70-78 GY) conformal radiotherapy for prostate cancer, using dose-volume histograms." eng. *Int J Radiat Oncol Biol Phys* 41.1 (1998), pp. 83–92.

[116] Mageras, GS; Kutcher, GJ; Leibel, SA; Zelefsky, MJ; Melian, E; Mohan, R; Fuks, Z. "A method of incorporating organ motion uncertainties into three-dimensional conformal treatment plans." eng. *Int J Radiat Oncol Biol Phys* 35.2 (1996), pp. 333–342.

[117] Yan, D; Jaffray, DA; Wong, JW. "A model to accumulate fractionated dose in a deforming organ." eng. *Int J Radiat Oncol Biol Phys* 44.3 (1999), pp. 665–675.

[118] Killoran, JH; Kooy, HM; Gladstone, DJ; Welte, FJ; Beard, CJ. "A numerical simulation of organ motion and daily setup uncertainties: implications for radiation therapy." eng. *Int J Radiat Oncol Biol Phys* 37.1 (1997), pp. 213–221.

[119] Miralbell, R; Ozsoy, O; Pugliesi, A; Carballo, N; Arnalte, R; Escudé, L; Jargy, C; Nouet, P; Rouzaud, M. "Dosimetric implications of changes in patient repositioning and organ motion in conformal radiotherapy for prostate cancer." eng. *Radiother Oncol* 66.2 (2003), pp. 197–202.

[120] Herk, M van; Remeijer, P; Lebesque, JV. "Inclusion of geometric uncertainties in treatment plan evaluation." eng. *Int J Radiat Oncol Biol Phys* 52.5 (2002), pp. 1407–1422.

[121] Söhn, M; Birkner, M; Yan, D; Alber, M. "Modelling individual geometric variation based on dominant eigenmodes of organ deformation: implementation and evaluation." eng. *Phys Med Biol* 50.24 (2005), pp. 5893–5908.

[122] Witte, MG; Geer, J van der; Schneider, C; Lebesque, JV; Alber, M; Herk, M van. "IMRT optimization including random and systematic geometric errors based on the expectation of TCP and NTCP." eng. *Med Phys* 34.9 (2007), pp. 3544–3555.

[123] Lips, IM; Heide, UA van der; Kotte, ANTJ; Vulpen, M van; Bel, A. "Effect of translational and rotational errors on complex dose distributions with off-line and on-line position verification." eng. *Int J Radiat Oncol Biol Phys* 74.5 (2009), pp. 1600–1608.

[124] Rijkhorst, EJ; Herk, M van; Lebesque, JV; Sonke, JJ. "Strategy for online correction of rotational organ motion for intensity-modulated radiotherapy of prostate cancer." eng. *Int J Radiat Oncol Biol Phys* 69.5 (2007), pp. 1608–1617.

[125] Schallenkamp, J; Herman, M; Kruse, J; Pisansky, T. "Prostate position relative to pelvic bony anatomy based on intraprostatic gold markers and electronic portal imaging". *International Journal of Radiation Oncology* Biology* Physics* 63.3 (2005), pp. 800–811.

[126] Nederveen, A; Dehnad, H; Heide, U van der; Moorselaar, R van; Hofman, P; Lagendijk, J. "Comparison of megavoltage position verification for prostate irradiation based on bony anatomy and implanted fiducials". *Radiotherapy and Oncology* 68.1 (2003), pp. 81–88.

[127] McNair, H; Hansen, V; Parker, C; Evans, P; Norman, A; Miles, E; Harris, E; Del-Acroix, L; Smith, E; Keane, R, et al. "A comparison of the use of bony anatomy and internal markers for offline verification and an evaluation of the potential benefit of online and offline verification protocols for prostate radiotherapy". *International Journal of Radiation Oncology, Biology and Physics* 71.1 (2008).

[128] Owen, R; Kron, T; Foroudi, F; Milner, A; Cox, J; Duchesne, G; Cleeve, L; Zhu, L; Cramb, J; Sparks, L; Laferlita, M. "Comparison of CT on rails with electronic portal imaging for positioning of prostate cancer patients with implanted fiducial markers." eng. *Int J Radiat Oncol Biol Phys* 74.3 (2009), pp. 906–912.

[129] Aoki, Y; Akanuma, A; Karasawa, K; Sakata, K; Nakagawa, K; Muta, N; Onogi, Y; Iio, M. "An integrated radiotherapy treatment system and its clinical application." *Radiation Medicine - Medical Imaging and Radiation Oncology* 5.4 (1987). cited By (since 1996) 12, pp. 131–141.

[130] Nijkamp, J; Pos, F; Nuver, T; Jong, R de; Remeijer, P; Sonke, JJ; Lebesque, J. "Adaptive Radiotherapy for Prostate Cancer Using Kilovoltage Cone-Beam Computed Tomography: First Clinical Results". *International Journal of Radiation Oncology Biology Physics* 70.1 (2008). cited By (since 1996) 39, pp. 75–82.

[131] Pouliot, J; Bani-Hashemi, A; Chen, J; Svatos, M; Ghelmansarai, F; Mitschke, M; Aubin, M; Xia, P; Morin, O; Bucci, K; Roach III, M; Hernandez, P; Zheng, Z; Hristov, D; Verhey, L. "Low-dose megavoltage cone-beam CT for radiation therapy". *International Journal of Radiation Oncology Biology Physics* 61.2 (2005). cited By (since 1996) 177, pp. 552–560.

[132] McNair, HA; Mangar, SA; Coffey, J; Shoulders, B; Hansen, VN; Norman, A; Staffurth, J; Sohaib, SA; Warrington, AP; Dearnaley, DP. "A comparison of CT- and ultrasound-based imaging to localize the prostate for external beam radiotherapy". *International Journal of Radiation Oncology*Biology*Physics* 65.3 (July 2006), pp. 678–687.

[133] Serago, CF; Buskirk, SJ; Igel, TC; Gale, AA; Serago, NE; Earle, JD. "Comparison of daily megavoltage electronic portal imaging or kilovoltage imaging with marker seeds to ultrasound imaging or skin marks for prostate localization and treatment positioning in patients with prostate cancer". *International Journal of Radiation Oncology*Biology*Physics* 65.5 (Aug. 2006), pp. 1585–1592.

[134] Langen, KM; Pouliot, J; Anezinos, C; Aubin, M; Gottschalk, AR; Hsu, I; Lowther, D; Liu, Y; Shinohara, K; Verhey, LJ; Weinberg, V; Roach, M. "Evaluation of ultrasound-based prostate localization for image-guided radiotherapy". *International Journal of Radiation Oncology*Biology*Physics* 57.3 (Nov. 2003), pp. 635–644.

[135] Mutanga, TF; Boer, HCJ de; Rajan, V; Dirkx, MLP; Os, MJH van; Incrocci, L; Heijmen, BJM. "Software-controlled, highly automated intrafraction prostate motion correction with intrafraction StereoGraphic Targeting (iSGT): system description and clinical results". eng. *Int J Radiat Oncol Biol Phys* (2011). Submitted, ROB-D-11-00397.

[136] Smitsmans, M; Pos, F; Bois, J de; Heemsbergen, W; Sonke, JJ; Lebesque, J; Herk, M van. "The Influence of a Dietary Protocol on Cone Beam CT-Guided Radiotherapy for Prostate Cancer Patients". *International Journal of Radiation Oncology Biology Physics* 71.4 (2008). cited By (since 1996) 12, pp. 1279–1286.

[137] Smitsmans, MHP; Bois, J de; Sonke, JJ; Catton, CN; Jaffray, DA; Lebesque, JV; Herk, M van. "Residual Seminal Vesicle Displacement in Marker-Based Image-Guided Radiotherapy for Prostate Cancer and the Impact on Margin Design." eng. *Int J Radiat Oncol Biol Phys* (2010).

[138] Korreman, S; Rasch, C; McNair, H; Verellen, D; Oelfke, U; Maingon, P; Mijnheer, B; Khoo, V. "The European Society of Therapeutic Radiology and Oncology-European Institute of Radiotherapy (ESTRO-EIR) report on 3D CT-based in-room image guidance systems: a practical and technical review and guide." eng. *Radiother Oncol* 94.2 (2010), pp. 129–144.

[139] Lagendijk, JJW; Raaymakers, BW; Raaijmakers, AJE; Overweg, J; Brown, KJ; Kerkhof, EM; Put, RW van der; Hårdemark, B; Vulpen, M van; Heide, UA van der. "MRI/linac integration." eng. *Radiother Oncol* 86.1 (2008), pp. 25–29.

[140] Herten, YRJ van; Kamer, JB van de; Wieringen, N van; Pieters, BR; Bel, A. "Dosimetric evaluation of prostate rotations and their correction by couch rotations." eng. *Radiother Oncol* 88.1 (2008), pp. 156–162.

[141] Davis, B; Cheville, J; Wilson, T; Slezak, J; Pisansky, T. "Histopathologic characterization of seminal vesicle invasion in prostate cancer: implications for radiotherapeutic management". *International journal of radiation oncology, biology, physics* 51.3 (Nov. 2001), pp. 140–141.

[142] Villers, AA; McNeal, JE; Redwine, EA; Freiha, FS; Stamey, TA. "Pathogenesis and biological significance of seminal vesicle invasion in prostatic adenocarcinoma." eng. *J Urol* 143.6 (1990), pp. 1183–1187.

[143] Fallone, BG; Murray, B; Rathee, S; Stanescu, T; Steciw, S; Vidakovic, S; Blosser, E; Tymofichuk, D. "First MR images obtained during megavoltage photon irradiation from a prototype integrated linac-MR system." eng. *Med Phys* 36.6 (2009), pp. 2084–2088.

[144] Lei, Y; Wu, Q. "A hybrid strategy of offline adaptive planning and online image guidance for prostate cancer radiotherapy." eng. *Phys Med Biol* 55.8 (2010), pp. 2221–2234.

[145] Li, T; Thongphiew, D; Zhu, X; Lee, WR; Vujaskovic, Z; Yin, FF; Wu, QJ. "Adaptive prostate IGRT combining online re-optimization and re-positioning: a feasibility study." eng. *Phys Med Biol* 56.5 (2011), pp. 1243–1258.

[146] Budiarto, E; Keijzer, M; Storchi, PR; Hoogeman, MS; Bondar, L; Mutanga, TF; Boer, HCJ de; Heemink, AW. "A population-based model to describe geometrical uncertainties in radiotherapy: applied to prostate cases". *Physics in Medicine and Biology* 56.4 (2011), p. 1045.

[147] Foroudi, F; Wong, J; Haworth, A; Baille, A; McAlpine, J; Rolfo, A; Kron, T; Roxby, P; Paneghel, A; Williams, S; Duchesne, G; Tai, KH. "Offline adaptive radiotherapy for bladder cancer using cone beam computed tomography." eng. *J Med Imaging Radiat Oncol* 53.2 (2009), pp. 226–233.

[148] Ahunbay, EE; Peng, C; Chen, GP; Narayanan, S; Yu, C; Lawton, C; Li, XA. "An on-line replanning scheme for interfractional variations." eng. *Med Phys* 35.8 (2008), pp. 3607–3615.

[149] Breedveld, S; Storchi, P; Bondar, M; Osorio, EV; Hoogeman, M; Heijmen, B. "Fast On-line Plan Adjustment for Adaptive Radiotherapy Evaluated for Prostate and Cervical Cancer". *International journal of radiation oncology, biology, physics* 78.3 (Nov. 2010), S744–S745.

[150] Unkelbach, J; Oelfke, U. "Incorporating organ movements in inverse planning: assessing dose uncertainties by Bayesian inference." eng. *Phys Med Biol* 50.1 (2005), pp. 121–139.

[151] Birkner, M; Yan, D; Alber, M; Liang, J; Nüsslin, F. "Adapting inverse planning to patient and organ geometrical variation: algorithm and implementation." eng. *Med Phys* 30.10 (2003), pp. 2822–2831.

[152] Teguh, DN; Levendag, PC; Voet, PW; Al-Mamgani, A; Han, X; Wolf, TK; Hibbard, LS; Nowak, P; Akhiat, H; Dirkx, ML; Heijmen, BJ; Hoogeman, MS. "Clinical Validation of Atlas-Based Auto-Segmentation of Multiple Target Volumes and Normal Tissue (Swallowing/Mastication) Structures in the Head and Neck". *International Journal of Radiation Oncology*Biology*Physics* In Press, Corrected Proof ().

[153] Al-Mamgani, A. "The dynamics of dose escalation of radiotherapy for localized prostate cancer: Abrahim Al-Mamgani". English. http://opc-prd.ubib.eur.nl:8080/DB=2/PPN?PPN=328865583/. PhD thesis. Rotterdam: Erasmus University, 2010.

[154] Brenner, DJ. "Toward optimal external-beam fractionation for prostate cancer." eng. *Int J Radiat Oncol Biol Phys* 48.2 (2000), pp. 315–316.

[155] Dașu, A. "Is the alpha/beta value for prostate tumours low enough to be safely used in clinical trials?" eng. *Clin Oncol (R Coll Radiol)* 19.5 (2007), pp. 289–301.

[156] Fowler, JF. "The radiobiology of prostate cancer including new aspects of fractionated radiotherapy." eng. *Acta Oncol* 44.3 (2005), pp. 265–276.

[157]   Boer, H de; Mutanga, TF; Wielen, G van der; Barnhoorn, J; Wentzler, D; In-crocci, L; Heijmen, B. "Daily Prostate Targeting With Stereographic Kvlmv Imaging And Fiducial Markers". *Radiotherapy and Oncology* 84.Supplement 1 (2007). Symposium - IGRT and correction Strategies: 9th Biennial ESTRO Meeting on physics and radiation technology for clinical radiotherapy, S56 – S60.

[158]   Boer, H de; Rajan, V; Barnhoorn, J; Mutanga, TF; Wentzler, D; Heijmen, B. "Fully automated on-line correction for intrafraction prostate motion by continuous imaging of fiducial marker". *Radiotherapy and Oncology* 88.Supplement 2 (2008). Poster discussion: European Society For Therapeutic Radiology And Oncology Annual Congress, ESTRO 27,14-18 September 2008, Goteborg, Sweden, S31 –S32.

[159]   Boer, JCJ de; Mutanga, TF; Wielen, GJ van der; Incrocci, L; Heijmen, BJM. "Efficacy Of On-line Translation And Rotation Corrections For Seminal Vesicle Coverage In Prostate Radiotherapy". *International Journal of Radiation Oncology*Biology*Physics* 72.1, Supplement 1 (2008). Proceedings of the American Society for Therapeutic Radiology and Oncology 50th Annual Meeting, American Society for Therapeutic Radiology and Oncology 50th Annual Meeting, S574 –S574.

[160]   Mutanga, TF; Boer, C de; Wielen, G van der; Incrocci, L; Heijmen, B. "Full Dosimetric Evaluation Of The Impact Of Organ Deformation, Rotation And Residue Positioning Errors In Prostate And Seminal Vesicle Irradiation". *Radiotherapy and Oncology* 88.Supplement 2 (2008). Proffered paper: European Society For Therapeutic Radiology And Oncology Annual Congress, ESTRO 27,14-18 September 2008, Goteborg, Sweden, S158 –S159.

[161]   Mutanga, TF; Boer, H de; Wielen, G van der; Heijmen, B. "Fast On-line Prostate Positioning With Stereographic Targeting On Kv/mv Image Pairs". *Medical Physics* 34.6 (2007). Abstract TH-C-M100J-04: 49th Annual Meeting of the American Association of Physicists in Medicine (AAPM), July 22-26, 2007, Minneapolis, MN, pp. 2624–2624.

[162]   Wielen, G van der; Boer, H de; Mutanga, TF; Schillemans, W; Osorio, EV; Kuipers, R; Incrocci, L; Heijmen, B. "Seminal vesicle motion and deformation relative to prostate implanted fiducial markers". *Radiotherapy and Oncology* 84.Supplement 1 (2007). Abstract Book: 9th BIENNIAL ESTRO MEETING ON PHYSICS AND RADIATION TECHNOLOGY FOR CLINICAL RADIOTHERAPY September 8-13, 2007 Barcelona, Spain, S43.

List of Abbreviations

Σ	systematic error
σ	random error
3D	three-dimensional
ABAS	Atlas-Based Auto Segmentation
ART	adaptive radiation therapy
CBCT	cone beam computed tomography
COM	center of mass
CT	computed tomography
CTV	clinical target volume
DRR	digitally reconstructed radiograph
EBRT	external beam radiation therapy
EPID	electronic portal imaging device
EUD	equivalent uniform dose
GTV	gross tumour volume
HU	Hounsfield units
ICRU	International Commission on Radiation Units and Measurements
IGRT	image guided radiation therapy
IMRT	intensity modulated radiation therapy
iSGT	intrafraction StereoGraphic Targeting
linac	linear accelerator
MRI	magnetic resonance imaging
MU	monitor units
NTCP	normal tissue complication probability

OAR   organs at risk

PTV   planning target volume

SGT   StereoGraphic Targeting

TCP   tumour control probability

Theodore Mutanga was born on the 4th of November 1978 in Bamenda, Cameroon. After completing high school, he entered the University of Buea as a science undergraduate with emphasis on Physics and a minor in Computer Science. He graduated with a Bachelor of Science (Honours) degree and worked for a few months as a wireless internet support technician in Douala before moving to Sweden for graduate studies in 2002. At Umeå University he enrolled in the International Master's in Physics program and later on, the Medical Physics (*Sjukhusfysiker*) program after he became interested in the applications of physics principles for cancer treatment. He graduated with double Master's degrees and later carried out an internship at the Norrlands University Hospital at the end of which he became certified as a licensed medical physicist by the Swedish National Board of Health and Welfare. He moved to Rotterdam in 2006 where he was employed by the Erasmus MC as a medical physics researcher at the Daniel den Hoed Cancer Center. His doctoral research has involved development and evaluation of systems and methods to ensure precision in prostate radiation therapy delivery using image-guidance.

Acknowledgements

There are many people with whom I would like to share the joy of the completion of this thesis. Without their support in all forms, shapes and sizes, this thesis would not have been possible. I would fill these pages with a lot of names if I was allowed to do so.

I thank Ben Heijmen for his thoughtful insights and for guiding me to the end of this thesis. Ben, you have been like a father to me, having fun when it is fun time but also getting your hands dirty when it is time for work. You have made yourself available on top of your very busy schedule and pulled all strings for me when things appeared to be moving slow. I appreciate your comments and meaningful suggestions that have improved the quality of my papers.

I appreciate everything Hans de Boer has contributed to this work, to my own development and for the many great discussions. Hans de Boer, you have taught me everything I know about EPIDs, correction protocols, statistical analyses, geometric errors and lots more. You have taught me how to carry out careful and meticulous simulations in scientific research. I appreciate the amount of time and energy you put into reading my papers.

I also express my sincere gratitude to all other staff, fellow PhDs and post Docs at the Daniel den Hoed for offering their expertise and time for the various projects that I have been involved with. In particular, I acknowledge all support from Jacco Barnhoorn, Davy Wentzler, Andras Zolnay , Wilco Schillemans, Eliana Vásquez Osorio, Sebastiaan Breedveld and Hafid Akhiat. I have learnt a lot in the area of computer programming from you guys. Thanks to your tireless support in getting my numerous requests honoured.

The following have also offered substantial contributions, their time and fruitful ideas which have gone a long way in helping me finish my projects and this thesis: Gerard van der Wielen, Wouter Wunderink, Pascal Storchi, Mischa Hoogeman, Maarten Dirkx, Sarah Osman, Marjolein van Os, Mascha van de Laar, Steven Petit, Erik Loeff and Dennis Grofsmid. My interaction with you all has made substantial contributions to my personal development. For all these, I say thank you to you all and I wish you the best in your future careers.

I will also like to acknowledge the help of Jacqueline van der Valk and Jolanda Jacobs in *'t kippenhok* for taking care of all practical matters which have contributed to a comfortable stay here in Rotterdam and in the Daniel den Hoed in particular.

My sincere appreciation also goes to Gordon Acha; without your support during my graduate studies in Sweden, I will not be where I am today.

Most especially, I thank my entire family for all invaluable support and for having such strong confidence in me.

Finally, I reserve my most special gratitude to my wife and best friend, Gisele. Thank you for being with me every step of the journey and for giving me two lovely kids.

List of Publications

Full Length Papers

Mutanga, TF; Boer, HCJ de; Wielen, GJ van der; Wentzler, D; Barnhoorn, J; Incrocci, L; Heijmen, BJM. "Stereographic targeting in prostate radiotherapy: speed and precision by daily automatic positioning corrections using kilovoltage/megavoltage image pairs." eng. *Int J Radiat Oncol Biol Phys* 71.4 (2008), pp. 1074–1083.

Wielen, GJ van der; Mutanga, TF; Incrocci, L; Kirkels, WJ; Osorio, EMV; Hoogeman, MS; Heijmen, BJM; Boer, HCJ de. "Deformation of prostate and seminal vesicles relative to intraprostatic fiducial markers." eng. *Int J Radiat Oncol Biol Phys* 72.5 (2008), 1604–1611.e3.

Mutanga, TF; Boer, HCJ de; Wielen, GJ van der; Hoogeman, MS; Incrocci, L; Heijmen, BJM. "Margin Evaluation in the Presence of Deformation, Rotation, and Translation in Prostate and Entire Seminal Vesicle Irradiation with Daily Marker-Based Setup Corrections." eng. *Int J Radiat Oncol Biol Phys* (2010).

Mutanga, TF; Boer, HCJ de; Rajan, V; Dirkx, MLP; Incrocci, L; Heijmen, BJM. "Day-to-day reproducibility of prostate intrafraction motion assessed by multiple kV and MV imaging of implanted markers during treatment". eng. *Int J Radiat Oncol Biol Phys* (2011). Submitted, ROB-S-10-02414 (1).

Mutanga, TF; Boer, HCJ de; Rajan, V; Dirkx, MLP; Os, MJH van; Incrocci, L; Heijmen, BJM. "Software-controlled, highly automated intrafraction prostate motion correction with intrafraction StereoGraphic Targeting (iSGT): system description and clinical results". eng. *Int J Radiat Oncol Biol Phys* (2011). Submitted, ROB-D-11-00397.

Budiarto, E; Keijzer, M; Storchi, PR; Hoogeman, MS; Bondar, L; Mutanga, TF; Boer, HCJ de; Heemink, AW. "A population-based model to describe geometrical uncertainties in radiotherapy: applied to prostate cases". *Physics in Medicine and Biology* 56.4 (2011), p. 1045.

Abtracts in Conference Proceeedings

Mutanga, TF; Boer., HD; Hoogeman, M; Wielen, GJ van der; Incrocci, L; Heijmen, B. "Radiobiological Evaluation Of The Impact Of Organ Deformation, Rotation And Residue Positioning Errors In Prostate And Seminal Vesicle Irradiation".

Radiotherapy and Oncology 92.Supplement 1 (2009). Abstract book: 10th BIENNI-AL ESTRO CONFERENCE ON PHYSICS AND RADIATION TECHNOLOGY FOR CLINICAL RADIOTHERAPY, 30 Aug - 3 Sep 2009, Maastricht, Netherlands, S118.

Boer, H de; Mutanga, TF; Wielen, G van der; Barnhoorn, J; Wentzler, D; Incrocci, L; Heijmen, B. "Daily Prostate Targeting With Stereographic Kvlmv Imaging And Fiducial Markers". *Radiotherapy and Oncology* 84.Supplement 1 (2007). Symposium - IGRT and correction Strategies: 9th Biennial ESTRO Meeting on physics and radiation technology for clinical radiotherapy, S56 –S60.

Boer, H de; Rajan, V; Barnhoorn, J; Mutanga, TF; Wentzler, D; Heijmen, B. "Fully automated on-line correction for intrafraction prostate motion by continuous imaging of fiducial marker". *Radiotherapy and Oncology* 88.Supplement 2 (2008). Poster discussion: European Society For Therapeutic Radiology And Oncology Annual Congress, ESTRO 27,14-18 September 2008, Goteborg, Sweden, S31 –S32.

Boer, JCJ de; Mutanga, TF; Wielen, GJ van der; Incrocci, L; Heijmen, BJM. "Efficacy Of On-line Translation And Rotation Corrections For Seminal Vesicle Coverage In Prostate Radiotherapy". *International Journal of Radiation Oncology*Biology*Physics* 72.1, Supplement 1 (2008). Proceedings of the American Society for Therapeutic Radiology and Oncology 50th Annual Meeting, American Society for Therapeutic Radiology and Oncology 50th Annual Meeting, S574 –S574.

Mutanga, TF; Boer, C de; Wielen, G van der; Incrocci, L; Heijmen, B. "Full Dosimetric Evaluation Of The Impact Of Organ Deformation, Rotation And Residue Positioning Errors In Prostate And Seminal Vesicle Irradiation". *Radiotherapy and Oncology* 88.Supplement 2 (2008). Proffered paper: European Society For Therapeutic Radiology And Oncology Annual Congress, ESTRO 27,14-18 September 2008, Goteborg, Sweden, S158 –S159.

Mutanga, TF; Boer, H de; Wielen, G van der; Heijmen, B. "Fast On-line Prostate Positioning With Stereographic Targeting On Kv/mv Image Pairs". *Medical Physics* 34.6 (2007). Abstract TH-C-M100J-04: 49th Annual Meeting of the American Association of Physicists in Medicine (AAPM), July 22-26, 2007, Minneapolis, MN, pp. 2624–2624.

Wielen, G van der; Boer, H de; Mutanga, TF; Schillemans, W; Osorio, EV; Kuipers, R; Incrocci, L; Heijmen, B. "Seminal vesicle motion and deformation relative to prostate implanted fiducial markers". *Radiotherapy and Oncology* 84.Supplement 1 (2007). Abstract Book: 9th BIENNIAL ESTRO MEETING ON PHYSICS AND RADIATION TECHNOLOGY FOR CLINICAL RADIOTHERAPY September 8-13, 2007 Barcelona, Spain, S43.

Erasmus MC
University Medical Center Rotterdam

Summary of PhD training and teaching

PhD Student: Theodore Funwi Mutanga   **PhD Period:** 2006 — 2011
ErasmusMC Department: Radiotherapy   **Promotor:** Prof.dr. B. Heijmen
Research School: Molecular Medicine   **Supervisor:** Prof.dr. B. Heijmen

---

1. PhD Training

Seminars and workshops

- ErasmusMC PhD Day   Rotterdam, Netherlands
  Attended 2 courses   24th May, 2007

Specific courses

- ESTRO Teaching Course on IGRT   Brussels, Belgium
  Certificate of Attendance   3 – 7 December, 2006

Presentations

- Impact of organ deformation, rotation and residue positioning errors in prostate and seminal vesicle irradiation, Maastricht.   2009

- Stereographic Targeting (SGT) for rapid daily prostate localization: Implementation and impact of residual positioning errors, Stresa.   2009

- Full dosimetric evaluation of the impact of organ deformation, rotation and residue positioning errors in prostate and seminal vesicle irradiation, Goteborg.   2008

- Stereographic Targeting of the Prostate Using Implanted Gold Markers, Eindhoven.   2007

- Fast Online Prostate Positioning with Stereographic Targeting on kV/MV Image Pairs, Minneapolis.   2007

Conferences

- 10th Biennial ESTRO Conference   Maastricht, Netherlands
  Invited speaker   30 Aug - 3 Sep, 2009

- 4th European Elekta Users Conference   Stresa, Italy
  Invited speaker   June 4 - 7, 2009

- ESTRO 27 Congress   Goteborg, Sweden
  Invited speaker   September 14-18, 2008

- 49th Annual AAPM Meeting   Minneapolis, MN, USA
  Invited speaker   July 22-26, 2007

- Project Day RKF   Eindhoven, Netherlands
  Invited speaker   February 2nd, 2007

2. Teaching

Department journal club lectures

- Strategies for coping with intrafraction prostate motion   2010

- Adaptive strategies for prostate radiotherapy   2010

- (QA of) image quality of in-room CT (kV, MV, Tomotherapy)   2008

- Precise prostate localization for external beam radiotherapy   2007

- Prostate rotations: Impact and correction   2006

Supervising Master's theses

- Paul A. van Duijvenvoorde
  (partial supervision)   2007

The research described in this thesis is focused on development and clinical evaluation of image-guidance solutions for correction of both inter- and intrafraction prostate motion in external beam radiotherapy. Corrections are based on planar imaging of implanted gold markers with MV and kV beams. The main advantages of the developed system include (1) high positioning accuracy, (2) minimal increase in fraction duration, (3) high degree of automation, i.e. minimal operator interference, (4) remote controlled couch re-positioning, (5) minimal additional imaging dose. Another important objective of the research was the assessment of residual errors, including organ deformation and rotation, to establish appropriate planning margins.